Novel Epoxide-Based Glutamate Agonist Class of Pesticide: Synthesis, Binding Mechanism, and Potency.

Honors Thesis
Presented to the College of Arts and Sciences,
Cornell University
in Partial Fulfillment of the Requirements for the Biological Sciences Honors Program

by
Ryan Erik Landvater
May 2014

Supervisor Chad Arthur Lewis

ABSTRACT

Global food production poses one of the greatest challenges for the planet in coming decades, and synthesis of next generation safer pesticides ranks among the important methods in combating this challenge. The vast majority of pesticides are halogenated lipophilic neurotoxins: highly potent in low concentrations and posing certain risks, such as implication in many neurodegenerative diseases. This study utilized the epoxide ring-opening neurotoxin motif found in the lophotoxin natural product family for the conceptualization of 2-epoxygluteric acid as a model class of next generation neurotoxins. Here, we report the stereo-enhanced synthesis of 2-epoxygluteric acid, the crystal structure of the binding domain of GluR2 bound to 2-epoxygluteric acid at 1.86Å, and electrophysiological potency assays showing the dynamic concentration range of both enantiomers. According to the crystal structure, 2-epoxygluteric acid failed to bind covalently to the receptor; however, it was found to bind non-covalently and cause nerve cord death in the crayfish arthropod model at 20mM.

I. INTRODUCTION

1.1 Agricultural Need

The human population has more than doubled from 3 billion in 1960 to the present 7 billion and is projected to grow by 70 million per annum to reach 9.1 billion by 2050. Unfortunately, due to a change in global diet, the demand for food production is projected to increase by 70% in this time frame (FAO, 2009). The agricultural expansion necessary to accommodate this change in production implies the destruction of forests, wildlife habitats and, ironically, the natural enemies of crop pests. Due to this agricultural pressure, coupled with a 35% pre-harvest crop loss due to

pests, there has never been a more dire need for effective pesticides (Oerke, 2006; Popp et al., 2013).

Natural products derived from botanical extracts such as nicotine, rotenone, and ryanodine were rapidly superseded from 1939 to 1990's by neuroactive synthetic pesticides such as DDT, endosulfan, chloropuriphos, and deltamethrin (Figure 1) (Casida and Quistad, 1998). These neurotoxic compounds are now the primary means of protecting crops, livestock and pets from arthropod pests in the United States. The compounds rapidly stop crop damage due to permeation through a lipoidal perineural sheath surrounding the insect nerve cord. However, these highly halogenated lipophilic compounds are fat-soluble – resulting in storage and chronic release in mammals– with proposed secondary effects contributing to neurologic degenerative disorders such as Parkinson's and Alzheimer's diseases (WHO, 1979; Casida and Durkin, 2013). Furthermore, water insoluble pesticides – both applied as powder and emulsions – have higher losses due to runoff than their water-soluble counterparts. Not only does this result in less effective pesticides, but also high environmental exposure to neurotoxic compounds with field half lives of 10-20 days for most (occasionally extending to 80 days), in addition to residual near-constant soil concentrations for several months (Wauchope, 1978).

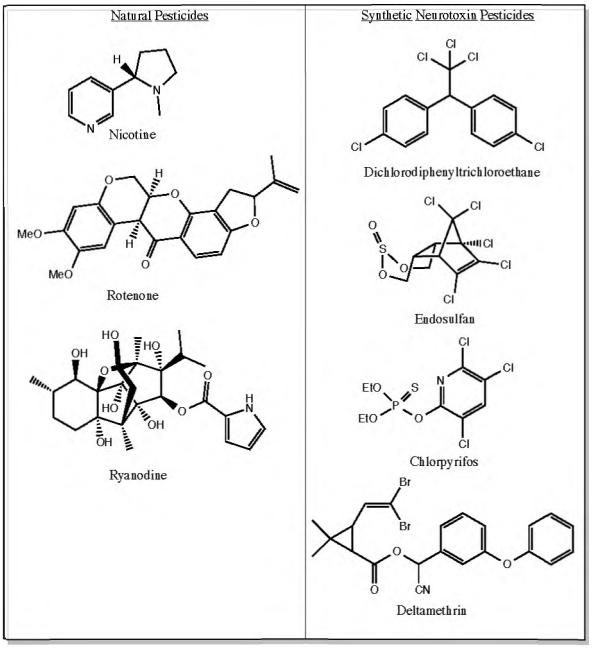

Figure 1: Natural extracts that were used as pesticides (left) were rapidly superseded throughout the 20th century by synthetic neurotoxic pesticides (right) which are highly lipophilic and implicated in the development of neurodegenerative disorders.

While the lipoidal sheath protects the arthropods' central nervous system (CNS) from ionized compounds, and is only susceptible to organic soluble pesticides, the peripheral nervous system (PNS) lacks this sheath and is a potential target for next generation smart pesticides. Anthropods utilize glutamate as the main excitatory neurotransmitter at the neuromuscular junction (NMJ). Interestingly, the perineural sheath has been shown to have permeability to L-glutamate (Defeudis, 1970), making both the NMJ and nerve cord potential targets. Exposure of highly potent glutamate receptor agonists at the NMJ causes rapid depolarization of the muscle fibers, resulting in contractile paralysis (Atwood and Cooper, 1996). It was concluded that the creation of an unstable, water-soluble compound with high affinity for glutamate receptors has the potential as a new class of pesticide. This class of compound can reduce the amount of runoff and has a lower half-life, thereby mitigating the environmental impact.

1.2 Glutamate Receptor Context

In recent decades the research community has experienced an explosion of interest in the molecular structure and dynamics of glutamate receptors – specifically following the cloning of cDNAs encoding binding subunits from 1989 to 1992 (Hollmann and Heinemann, 1994) – for their role in mediating the majority of excitatory synaptic transmission of higher vertebrates (Dingledine et al., 1999). Furthermore, the important roles of ionotrophic glutamate receptors (iGluRs) play in the formation of synaptic plasticity, crucial for higher order processing such as learning and memory or neuronal development, has been the staple principle motivating pharmacological studies.

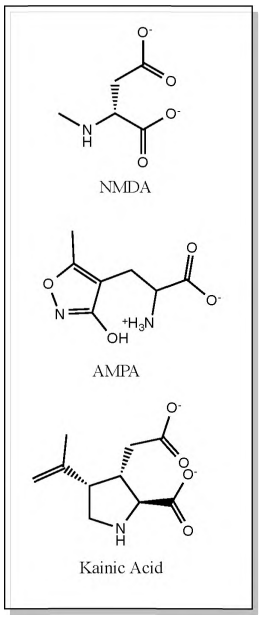

Figure 2: GluR agonists used to distinguish binding pocket sequence classes.

There are three pharmacologically defined classes of iGluRs distinguished by their respective selective agonists: N-methyl D-aspartate (NMDA), α-Amino-3-hydroxy-5-methyl-4-isoxazolepropionic acid (AMPA), and kainate (Figure 2). Receptor sequence homology between the six gene families comprising these receptors suggest a common evolutionary origin (Suchanek et al., 1995). This homology permits the utilization of multiple target organisms in binding studies as well as results that are beneficial in many facets of our modern society. For example, results from research conducted on pesticides in arthropods can be utilized for pharocological research in mammals. A high-resolution crystal structure shows the ligand-binding domain of iGluR2 (AMPA) receptor from *Rattus norvegicus*, which contains a conserved glutamic acid binding-pocket formed from two globular domains (S1 and S2). The ammonium-binding motif of the GluR2 S1S2 subunit viewed at ultra-high 1.45Å resolution shows the alpha ammonium donates three hydrogen bonds to E-193, T-91, and P-89 to hold the neurotransmitter in the cleft (Figure 3) (Krintel et al., 2012). The secondary hydrogen-bond donation from T-91 to E-193 for structural stability should theoretically enhance the nucleophilicity of threonine. This creates the potential for epoxide-based neurotoxins.

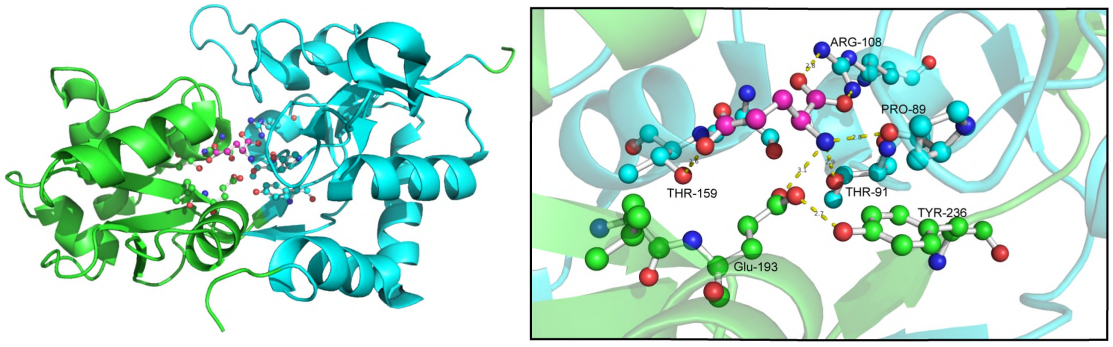

Figure 3: Residues N392-K506 and P632-S775 of the full rat GluR2 (AMPA biding) subunit domains S1 (green) and S2 (blue) connected by a "GT" linker bind glutamate by accepting hydrogen bonds at T-91, P-89, and E-193 (Krintel et al., 2012).

1.3 Pharmacological Rational

The marine natural products within the lophotoxin family are epoxide-based acetylcholine antagonists that bind slowly, but covalently, to the ligand pocket at Y-190 in the α-subunit of the nicotinic acetylcholine receptor (nAchR). Lophotoxin utilizes molecular mimicry with a lactone and extracyclic quartinary epoxide at the same approximate location as the ammonium in acetylcholine (Figure 4). The anionic tyrosine, which normally interacts with ammonium via electrostatic attraction, undergoes nuceophilic substitution (S_N2) at the epoxide – binding the receptor and ligand irreversibly (Groebe and Abramson, 1995). This same concept was utilized in the construction of 2-epoxygluteric acid [IUPAC 3-(2-Carboxy-2-oxiranyl)propionic acid](**1**) for use on glutamatergic neurons and muscles.

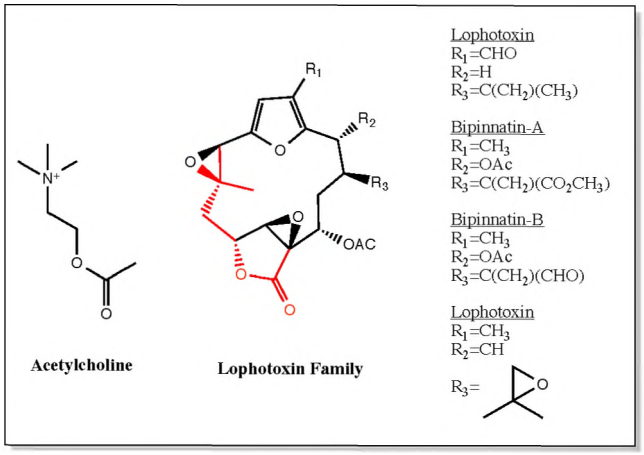

Figure 4: The lophotoxin family of epoxide-based marine neurotoxins bind covalently but slowly to the nAChRs at T-190 using molecular mimicry.

The purpose of this study was the synthesis and binding affinity assays of the epoxide-based covalently-binding neurotoxin skeleton (**1**) with hopes that such structural motifs could be used in the future to construct safer pesticides. A stereo-selective synthesis was performed, as vastly different effects are often observed between enantiomers of ligands in a biological context. Crystals of the GluR2 S1S2 binding domains, bound to L-Aspartate, were then augmented with the epoxide ligand (**1**) and the structure solved to show association to the ligand, but not via the

anticipated ring opening mechanism. Electrophysiological studies were chosen over ligand binding assays, as they were in better alignment with the goal of this study, which was to find the potency of the ligand to arthropod nervous system. Assays were performed to probe the effect of the compound on in vivo systems of crayfish and showed that the epoxide caused nerve death in 20mM to 40mM concentrations depending on the enantiomer.

II. Synthesis

The construction of an epoxide alpha to a ketone on a bis-acid poses a synthetic challenge due to the electron deficient ring's susceptibility to elimination. Furthermore, emphasis must be placed on the stereochemistry of products in the construction of biological ligands, since enantiomers often vary greatly in their effect (Grond and Sablotzki, 2004). In glutamate biosynthesis, alpha-ketoglutaric acid (α-KG; **2**), a readily available metabolite of the Kreb's cycle, undergoes a stereoselective reductive amination catalyzed by glutamate dehydrogenase (GDH) (Grabowska et al., 2011). Two retro-synthetic routes were devised following this biosynthesis (Scheme 1). α-KG is commercially available in bulk with a highly electrophilic carbonyl, which provides an excellent synthetic handle for condensation chemistry.

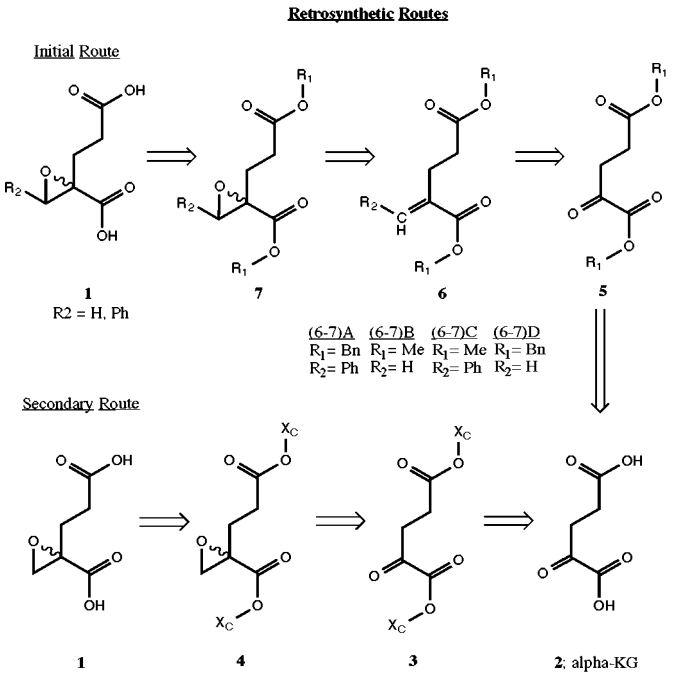

Scheme 1: Retrosynthetic routes of 1. The initial route was constructed based upon asymmetric epoxidation of a terminal olefin. The second route coupled alkylation and epoxidation into a single step and stereoisomers resolved on column.

Asymmetric epoxidation provides a versatile tool in synthesis. The vast majority of asymmetric epoxidation catalysts such as the Sharpless' utilize metal centers directed by heteroatoms to epoxidize olefins, though recent work by organocatalytic groups such as Scott Miller or Karl Anker Jørgensen have shown high enantioinduction with peptide derived catalysts using asymmetric or symmetric directing groups on the substrate (Denmark and Wu, 1999; Davis et al., 2014; Lichtor and Miller, 2014). The initial, but unsuccessful, synthetic route for (**1**) planned to utilize organo-catalytic asymmetric epoxidation following alkylation, while the secondary synthetic route utilized bis-chiral auxiliaries to separate diastereomers (**4**) with column chromatography followed by cleavage of the esters to produce enantiomerically enriched products.

2.1 Initial Route

Protection of the carboxylic acid was necessary early in the synthesis due to the use of basic alkylating conditions at the alpha-carbon in both routes. The eventual primary epoxide at the α-carbon created constraints on the possible deprotection reactions, which commonly include using acid and base to return the ester to the free-acid. For the first synthetic route, benzyl-protection of both free acids was deemed the most strategic option due to the functional group tolerant hydrogenolysis of benzyl esters when returning to the free acids.

Condensation of benzyl alcohol was attempted via a Fischer Esterification reaction using a Dean-Stark trap in toluene. Unfortunately, extended heating resulted in the decomposition of the starting material. Reduction of time from 26.5 hrs to 5 hrs resulted in significantly less

degradation of the starting material, but little product was observed by thin layer chromatography (TLC). It was concluded that reduced time and heat would likely curb the amount of starting material or product decomposition. An esterification method utilizing boron trifluoride etherate heated in a sealed tube at lower temperature for reduced times was used and, following workup and purification by column chromatography, compound (**5A**) was identified by NMR spectroscopy (Scheme 2). Unfortunately, the product could only be purified at a low scale by large volume water washings. Larger scale reactions were contaminated with benzyl alcohol following repeated purification via column chromatography and washings. A methyl-protected product (**5B**) was synthesized with the same procedure for its ease of production, purification, and to be used as a control in future reactions (Scheme 2). A screen of alkylating conditions with aryl and methyl constituents were tried on **5A** and **5B**, however NMR spectroscopy indicated 56% conversion to the E/Z stereoisomers of the methyl-protected alkene (**6B**) with no conversion of **5A**. It is likely that residual alcohol starting materials were poisoning these delicate basic alkylation conditions. This synthetic route was abandoned following these failures.

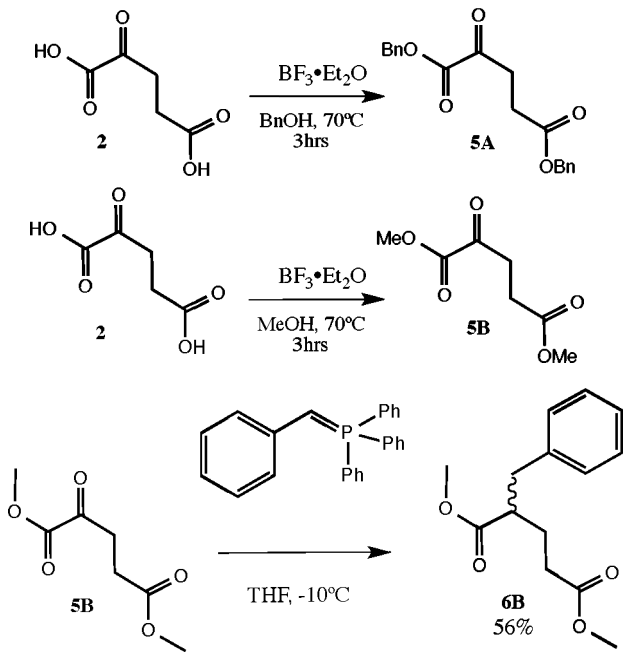

Scheme 2: Ester protection and alkylation conditions.

2.2 Second Route

The need for a removable chiral auxiliary for diesereometic resolution as well as ester protecting group led to the decision to use L-menthol over benzyl alcohol for protection of the bis-acid. Furthermore, the more facile separation of protected ester from starting material by column chromatography was considered and weighed against the potential difficulties in deprotection following epoxidation. Ultimately, the benefits were considered more advantageous to the synthetic goals of the project. A Fisher Esterification was performed using a Dean-Stark trap to condense L-menthol onto α-KG. Refluxing benzene was used instead of toluene due to the lower boiling point (80.1°C) relative to that of toluene (110.6°C) and α-KG's propensity to decompose in acid at elevated temperatures observed in the initial synthetic route (Matsumoto and Harada, 1966). The bis-menthol ester (**3**) was recovered in 55% yield following purification by column chromatography and characterized by ^{13}C and ^{1}H NMR spectroscopy (Scheme 3).

The two-step epoxidation scheme considered in the initial synthetic route was combined into a single step through the use of diazomethane as nucleophilic and electrophonic methylene source. The enhanced electrophilicity of the alpha-ketotone permits this unusual epoxidation reaction (dos Santos and de Magalhães, 1991). Following separation by column chromatography, 14.2% of highly

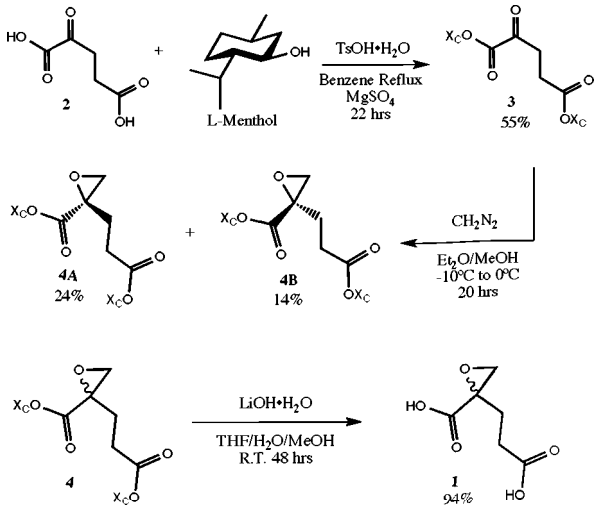

Scheme 3: Synthesis of 1 via Route 2

diestereomerically enriched epoxide (**4A**) and 24.0% of the other less diesteroenriched epoxide (**4B**) was recovered and characterized by ^{13}C and ^{1}H NMR spectroscopy (Scheme 4). Liquid chromatography mass spectroscopy (LCMS) showed a mass corresponding to the epoxide ring opened by water vapor on the source.

The use of sterically encumbered L-menthol as the protecting group for the carboxylic acids coupled with an electron deficient epoxide, reduces the number of possible deprotection conditions. Deprotection of secondary epoxides adjacent to carboxylic acids has been reported by Milewska et al., 2012 using potassium silox; however, initial attempts to deprotect the 2-epoxygluteric bis-menthol ester (**4**) with lithium silox showed no conversion after 24 hours by TLC and crude ^{1}H NMR. Nicolaou et al., 2005 reported the use of trimethyl tin hydroxide as a mild and neutral pH method for ester hydrolysis. However, after 40 hrs of reaction ^{1}H NMR showed retention of menthol ester protecting groups. It was considered that the large tin center was too encumbered by menthol to be nucleophilic at the carbonyl. Lithium hydroxide hydrate was used instead for the hydrolysis. Following 48 hrs of reaction, TLC and ^{1}H NMR showed full conversion of starting material, yielding 94% of bis-acid product (**1**) with LiCl salt (Scheme 4).

III. Crystallographic Studies

3.1 Crystal Preparation and Data Collection

Crystals of the S1S2 domains, consisting of residues N392-K506 and P632-S775 of the full rat GluR2 (AMPA biding) subunit connected by a "GT" linker, were grown by Ahmed Ahmed (Oswald Lab, Cornell University) from a construct provided by Eric Gouaux (Armstrong and Gouaux, 2000) in complex with L-aspartate. Crystals were transferred from the hanging drop to a

solution of 20% polyethylene glycol (PEG) 8K, 0.1 M sodium cacodylate (pH 6.5), 0.25 M ammonium sulfate, 0.1 M zinc acetate, and 2.5 mM **1B** and soaked for 15hrs. Crystals were cryoprotected using a 25% glycerol reservoir solution and quenched in liquid nitrogen before being transported to the synchrotron. Attempts to grow the crystals in complex with **1B** failed to yield crystals under an array of conditions. Significant cracking and fracturing of higher volume crystals was observed following extended soaking in 2.5 mM **1B** and immediately following exposure to 10 mM **1B**.

Data was collected at the Argon National Lab Advanced Photon Source through the North Eastern Collaborate Access Team (NE-CAT) facility at the 24 C undulator beam line using a Pilatus - 6MF pixel array detector (PAD). The RAPD pipeline, using Mosflm and BEST geometric and quantitative strategy programs, was utilized for data collection strategy. Two crystals (one from each ligand soak duration) were found to diffract significantly and data was collected using a 0.9789Å wavelength beam. iMosflm was used for autoindexing and integration (Battye et al., 2011). Pointless was used for laue group identification and Scala for reflection data scaling (Winn et al., 2011). Structures were solved by molecular replacement using Phenix 1.8.4 Phaser-MR (Armstrong and Gouaux, 2000; Adams et al., 2010). Refinement was performed using phenix.refine and the model constructed using Coot 0.7 (Emsley et al., 2010; Afonine et al., 2012).

3.2 Structure of GluR2 S1S2

The structure of the glutamate binding subunit domains S1S2 was solved by molecular replacement to phase correct according to a previous crystal structure taken at 1.9Å (RSCB

1FTJ) (Armstrong and Gouaux, 2000) with the glutamate ligands removed. The refinement statistics are provided in Table 1. The structure was solved at 1.86Å and three chains were found within the asymmetric unit. The ligand-binding pocket was well resolved and the resolution bin of 1.89-1.84Å showed an R-free of 28.3% (overall R-free of 21.76%). The binding pocket showed significant steric clashing with the slightly larger ligand (**1**) at E-193 and T-91, but the observed structure factors were consistent with the calculated at sigma 2.95 RMDS (Figure 5). Mol probability was used for structure validation, generating an overall score of 1.60 (Chen et al., 2010).

Table 1. Data collection and refinement statistics

Parameter	GluR2 S1S2 1B-Bound
Wavelength (Å)	0.9789
Resolution range (Å)	66.22 - 1.841 (1.907 - 1.841)
Space group	P 2 21 21
Unit cell	47.19 113.43 163.13 90 90 90
Total reflections	106005 (10852)
Unique reflections	59502 (6173)
Multiplicity	1.8 (1.8)
Completeness (%)	77.36 (81.39)
Mean I/sigma(I)	8.99 (2.20)
Wilson B-factor	21.66
R-merge	0.04309 (0.3324)
R-meas	0.06094
CC1/2	0.998 (0.728)
CC*	0.999 (0.918)
R-work	0.1889 (0.2394)
R-free	0.2176 (0.2788)
Number of non-hydrogen atoms	6790
macromolecules	6107
ligands	49
water	634
Protein residues	783
RMS(bonds)	0.009
RMS(angles)	1.28
Ramachandran favored (%)	98
Ramachandran outliers (%)	0
Clashscore	11.90
Average B-factor	30.20
macromolecules	29.40
ligands	26.80
solvent	37.40

*Statistics for the highest-resolution shell are shown in parentheses.

Structure solutions using L-aspartic acid as a ligand resulted in electron deficiency at the side-chain carboxylate that shares hydrogen bonds with T-143 and failed to refine sufficiently. This is indicative that the initial ligand was displaced. Examinations of the electron density relative to the epoxide model indicated there was a reduction in electron density at the primary epoxide carbon, while S-142 had excess electron density dispersed towards the epoxide sigma anti-bonding orbital when viewed with sigma level of 3 (Figure 6). The epoxide dipole, created by oxygen's electronegativity in a strained ring, appears to draw significant electron density from the adjacent T-91, S-142, E-193 oxygen lone pairs. Electrostatic attraction to the terminal carbon

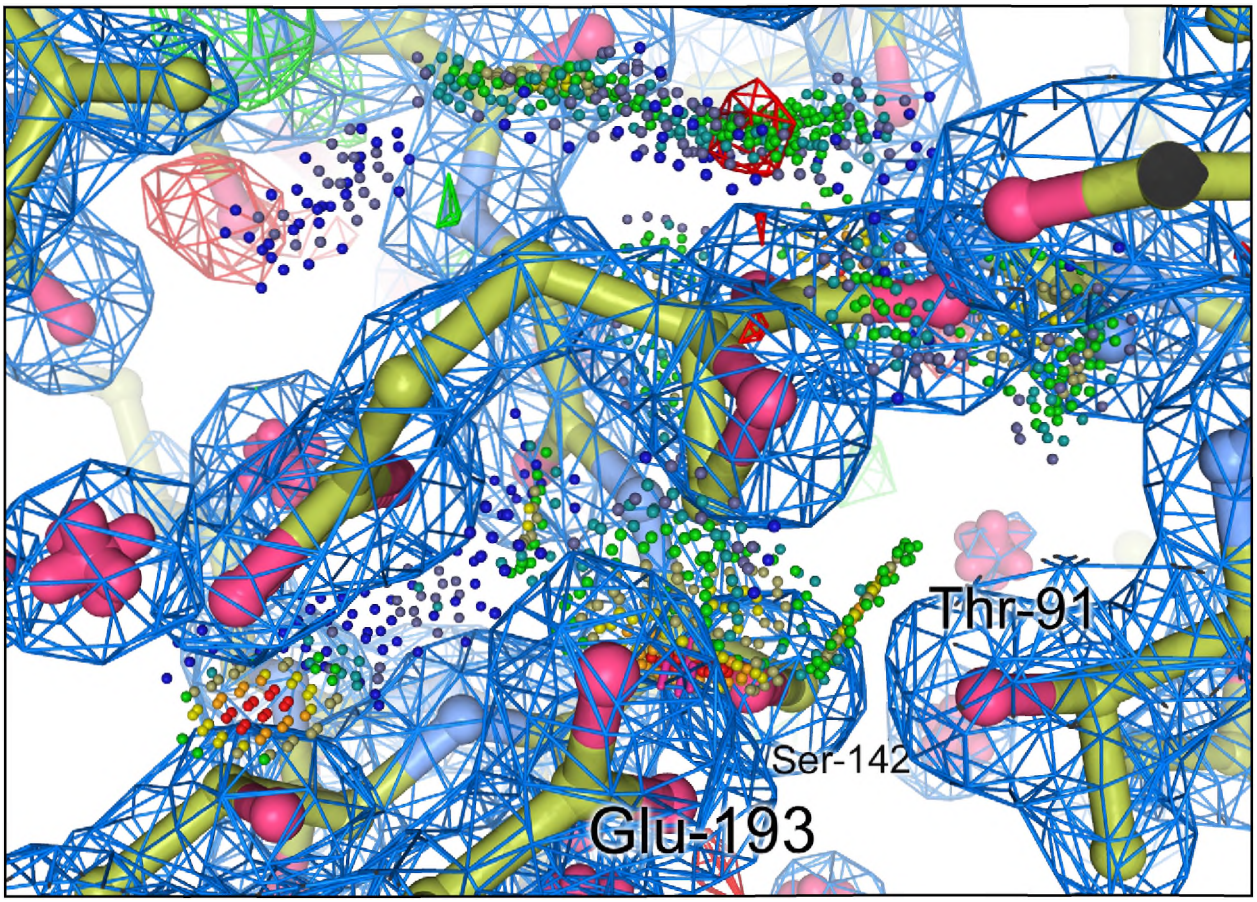

Figure 5: Electron density of 1B (center) within the binding pocket at a sigma level of 1.3. Structure factor difference map (green Fo-Fc>0; and red Fo-Fc <0) plotted at a sigma level of 3 shows model consistency with observed reflections. Steric contacts (pink) were observed between the ligand and T-91 and E-193.

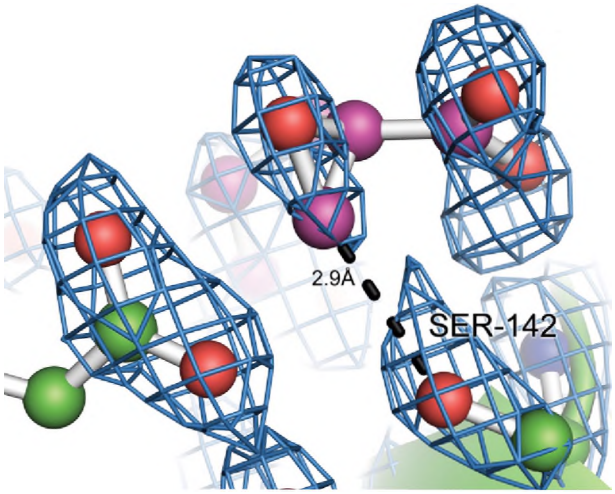

Figure 6: Electron density is deficient on the terminal carbon of the epoxide and directed towards the oxygen when observed at a sigma level of 3. Electron density from S-142 is drawn into the sigma antibonding orbital of the epoxide. These electrostatic interactions hold the ligand bound to the receptor at the epoxide.

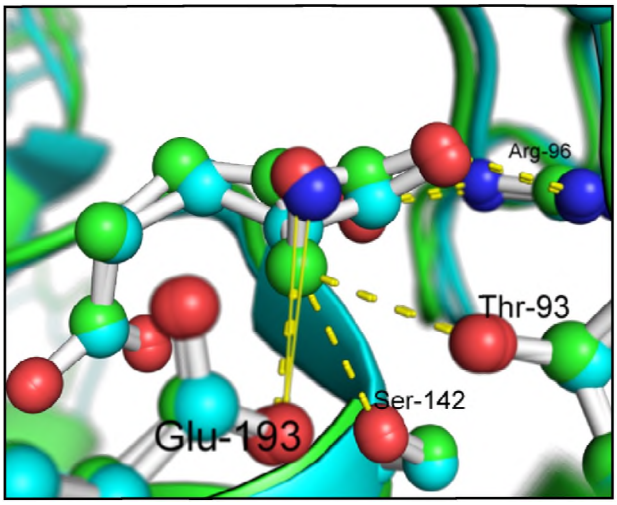

Figure 7: Binding site comparison between glutamate (teal) and 1B (green). Residues bound to glutamate were distanced farther from the ligand than residues bound to 1B. Additionally, the plane of the epoxide ring is held at angle of 3.2°, relative to the ammonium, with the sigma antibonding orbital oriented towards S-142 (solid yellow line).

of the epoxide shifted the residues T-91, S-142, E-193 by approximately 0.1Å towards the ligand binding site relative to their native position when bound to glutamte. Interestingly, the epoxide was angled 3.2° away from the native location the ammonium on glutamate in the direction away from T-91. It is likely that the donation of electron density into the epoxide anti-bonding orbital by S-142 is responsible for this slight rotation. The carboxylate adjacent to the epoxide was elevated towards Y-61, angling the carbonyl towards R-96 and shortening the hydrogen bonding distance by 0.2Å (Figure 7). These characteristics were calculated based upon chain B, which lacked the psudo-symmetry shared by chains A and C, yet resolved with higher clarity. The overall macromolecular structure of the domains did not shift dramatically due to the binding of the epoxide relative to the glutamate bound state when superimposed on a literature model (Figure 8)(Armstrong and Gouaux, 2000).

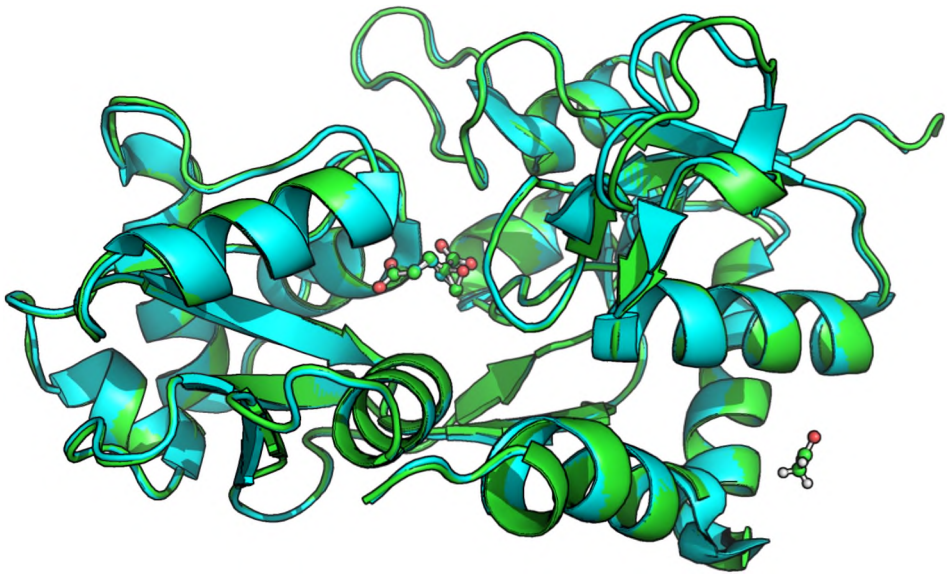

Figure 8: The overall macromolecular structure of the glutamate receptor changed only slightly between the glutamate bound form (teal) and the 1B bound form (green).

IV. CRAYFISH ELECTROPHYSIOLOGICAL STUDIES

4.1 Dissection and Recording

All animals were treated according the Cornell University policy 1.4 on Care and Use of Animals in Research and Teaching (Cornell Policy Library, 2012). Four living crayfish were placed under ice for ten minutes – until no movement was observed. Dissection procedure was done identically for each of the four preparations. The tail was extended and a cut was made at the base of the tail, where it joined with the cephalothorax. The cephalothorax was then placed in a -17.8°C freezer. The abdomen and tail were pinned in a dissecting dish with the ventral side facing upward and then submerged in 30 mL of cold crayfish saline ($[K^+]$ = 5.4 mM; $[Na^+]$ = 207.3 mM; $[Ca^{2+}]$ = 10mM; $[Mg^{2+}]$ = 2.6 mM; $[Cl^-]$ = 235.6 mM (Wyttenbach et al., 1999).

An incision was made at sternite four and extended anterior to sternite three (through segment S4). Superficial lateral cuts were made to the skin along the length of sternite three to the right and left of the ventral nerve cord (VNC). The skin and superficial flexor muscles were then pulled back to reveal nerve 3 (N3) extending laterally and into the superficial flexors. An extracellular glass electrode was submerged in the saline, which was drawn into the tip using a connected syringe, ensuring the silver wire was covered completely. Suction was applied to N3 and tension relieved from the skin and superficial flexor to allow the nerve to loop into the tip of the electrode. Signals from the extracellular electrode were passed through an alternating current amplifier and amplified by 10,000 fold with high and low pass frequency noise reduction. Output was relayed to a Tektronix TDS 1002 60mHz digital oscilloscope, speakers, and recorded using LabChart 8 through ADinstruments PowerLab 26T (model ML4856) electrode-computer interface.

Stock solutions of mono-sodium glutamate (MSG), **1A**, and **1B**, were prepared by dissolving each solid in 10 mL of crayfish saline and serial diluting to various concentrations. Baseline activity was recorded and then saline was removed from the preparation tray until level with segment S4. The dilutions were gently applied in single millilitre aliquots to the segment and recordings were taken for approximately 5 minutes or until activity stabilized. Two millilitre saline washes were performed between additions of the solutions. One preparation was used for each compound and recordings lasted for approximately one hour per preparation. The oscilloscope was turned off during most recordings to avoid electrical interference and reduce background noise by approximately half (0.1V). Addition of compounds 1A and 1B often resulted in the contraction of superficial flexors and deep phasic flexors and dislodged the electrode. Therefore, during later recordings, the nerve was often released and suctioned again to reestablish a strong seal and increase recording fidelity.

4.2 Dosage Response

Spontaneous firing was observed from N3 prior to addition of MSG, **1A**, or **1B**. Waveform analysis by spike amplitude and duration showed 3-4 distinct action potentials from 4 axon classes of differing diameter (Figure 9). Additional waveforms were observed in the voltage traces indicating a fifth, high amplitude, class of axon with insignificant baseline activity. The lowest amplitude axons (Unit 2; 0.03mV) fired at the highest frequency – 6 Hz in the MSG preparation and 15 Hz in the 1B preparation – in the MSG and **1B** preparations, though exhibited less activity in the 1A preparation (1 Hz). Alternatively, the **1A** preparation showed the highest basal high amplitude axon activity (Unit 3; 0.10mV) with an average firing rate of 13 Hz. It was

found that the firing rate of the small diameter axons (Unit 1 and 2) was inversely correlated to the firing rate of the high diameter axons (Unit 3 and 4) in the comparison of basal firing rates between preparations. These differences in preparations' native firing rates was considered in dose response analysis.

MSG was used as a positive binding control to measure the response of N3 to glutamate receptor activation under the dynamic concentration range for **1A** and **1B**. Addition of MSG up to 90 mM showed a gentle increase followed by decrease in firing frequency in most axons – specifically Axon 1 and 3 were nearly silenced at 90 mM. Axon 2 was seen to increase firing rate by as much as 300% within this range. Washing the recording site with saline following the addition of MSG often returned the firing rate and characteristics towards baseline, but could not return the firing to normal. Addition of higher concentration MSG (90-180mM) following 20 min of recording showed a shift in firing rates back towards baseline in all axons (Figure 9).

Perfusion of **1B** showed a slow increase in firing rate to 125% of basal at approximately 5mM with slow reduction back to 110% with 10mM in low diameter axons over the course of 12 minutes. The firing rate of large diameter axons increased with the addition of 5mM **1B** on average by only 0.54 Hz; however, this reflects a greater than 400% increase in activity. Firing rate of large diameter axons also decreased towards basal activity with addition of 10mM **1B**. Following the addition of 15mM **1B**, a significant change in firing characteristic was observed, in which the firing frequency of low diameter axons decreased to 70% of basal activity and large diameter axons increased activity by over 2800% of basal activity. Furthermore, action potentials generated by low diameter axon slowly dropped in amplitude from within the Unit 1 amplitude

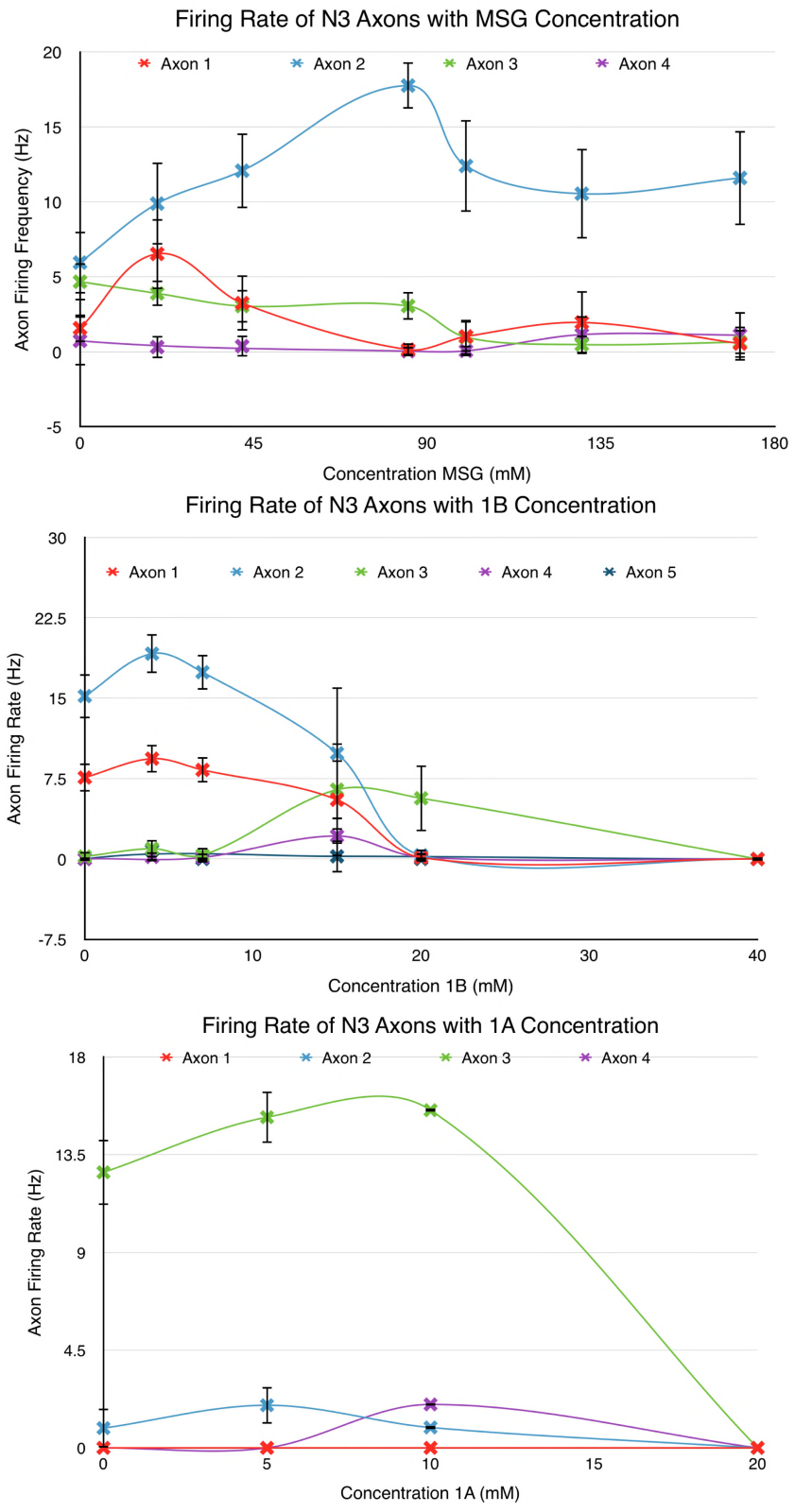

Figure 9: Dosage response curves for MSG (top), 1B (center), and 1A (bottom). MSG showed an increase in axon 2 firing rate up to 90mM with decrease in Axon 1 and 3, but ultimately returned to baseline following additional time and MSG. 1B showed a maximum response at approximately 20 mM and death at 40 mM. 1A had a sharper response with maximum effect seen at 10 mM and death following 20 mM.

range (0.8-0.5mV) to the Unit 2 range (0.3mV). These action potentials maintained consistent voltages until recording was ceased (410 sec) following this linear reduction in voltage over 260 seconds following addition of **1B**. Rhythmic firing emerged as well in Unit 3 axons and intensified following the addition of 20mM **1B** (Figure 10). A significant change in physiology – in the form of near silencing of small axons coupled with a large increase in wide diameter axon firing rate – was observed following 20mM **1B.** Complete nerve death was observed within 20 seconds after addition of 40mM **1B** (Figure 9).

Addition of the higher enantiomerically enriched epoxide **1A** showed a more dramatic dosage response curve. Following perfusion of 5mM, a slow increase in firing frequency was observed in axon 3 but axons 2 doubled the firing rate – similarly to **1B** at 5mM. The perfusion of 10mM **1A** reduced firing frequency in axon 2 back to baseline while axon 3 continued to gradually increase firing rate. Large amplitude axon 4 began firing at following this addition. Nerve death occurred after 24 seconds of exposure to 20mM **1A**. A rapid increase in firing of axon 3 to 35Hz occurred just before firing ceased. Washing out revived the nerve and large amplitude axons fired in bursts. A second addition of 20 mM **1A** again caused rapid nerve death (Figure 9).

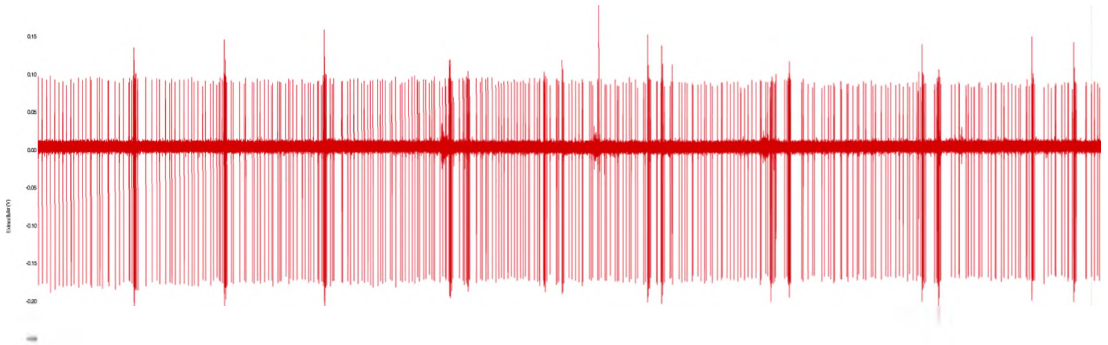

Figure 10: Rhythmic firing bursts from large axons within N3 were observed in the voltage trace following higher concentrations of the epoxide agonists 1A and 1B. (1B; 20mM)

V. DISCUSSION

The stability of epoxide rings is a difficult molecular characteristic to predict. While ring stability in **1A** and **1B** was a significant asset in the synthesis – specifically for ester deprotection under extreme pH ranges – it failed to allow for covalent binding to the receptor within the binding pocket. The initial model used in the conceptualization of the ligand placed the ligand within range of the secondary oxygen's non-bonding orbitals on T-91; however, steric restraints imposed by the hydrogens on the terminal carbon of the epoxide orient this antibonding towards S-142 (Figure 6). While distance between S-142 and the terminal carbon is comparable to T-91, the epoxide requires a very enhanced nucleophile to open through substitution, as indicated by high deprotection yields using lithium hydroxide. Furthermore, the phenol hydroxyl moiety on tyrosine has a pK_a of 10.07, resulting in a fully anionic residue for substitution in the binding of lophotoxin rather than the uncharged serine and threonine at physiological pH (Rupp, 2010 p.41). It should be noted, however, that the pH used for crystal augmentation was an order of magnitude more acidic than physiological pH. And while lophotoxin shows reversible binding constant (K_d) of 4.23μM, indicating that a strong non-covalent interaction does hold the toxin in the receptor, the slow zero-order covalent binding rate constant of 0.063 min^{-1} indicates that even the fully anionic residue opens the epoxide slowly (Groebe and Abramson, 1995). It was initially conceived that the construction of a less sterically encumbered skeleton would increase the covalent binding rate constant in this system; however, the kinetic implications of steric versus charge effects on this system of neurotoxic compounds was not a topic discussed in the literature. Ultimately, it appears the electrophilicity of epoxide sites mimicking cationic ligands may play the most significant role in binding affinity for this class of suicide inhibitors.

The structure factors predicted by the model corresponded best with the observed reflections when refined against the R-stereoisomer (**1A**). Crystal augmentation was specifically performed with the less enantiomerically pure epoxide stock (**1B**) with the assumption that the higher affinity enantiomer would bind almost exclusively and synthesis enantiomeric determination would be performed following electrophysiological studies. This was deemed the most strategic method for structural determination and the relative potency of enantiomers without the use of asymmetric epoxidation catalysis or advanced 2D NMR techniques.

While each preparation had unique firing characteristics that bias the interpretation of dosage response, certain trends were observed following the addition of ligands. Nerve toxicity followed a continuum wherein MSG failed to kill the nerve, while 1B at 40mM and 1A at 20mM were lethal. This approximate two-fold potency of 1A over 1B suggests strongly that 1A is the R-enantiomer of the epoxide. MSG was only applied around the dynamic concentration range found for the epoxide enatiomer solutions. Anecdotal evidence suggests, however, that the characteristic large amplitude 'burst' firing patterns, seen following the addition of ~20mM both epoxide enantiomers (1), are observed following glutamate concentrations at and exceeding 300mM (Landvater and Galanko, 2013). This suggests the use of MSG as a positive control was ineffective in modeling the activity of the compound due to insufficient concentration.

All compounds elicited an increase in unit 2 firing activity initially, with concentrations ranging from 5mM 1A to 90 mM MSG. The epoxide species were seen to cause a rapid decrease in small axon firing rates, while coincidentally increasing the firing rate of large diameter axons dramatically. This likely represents the activation of antagonistic pathways within the crayfish

nerve cord by the substrate due to the arthropod motor neuron configuration wherein both excitatory and inhibitory neurons innervate muscles. The large axon 3 is inhibitory at the crustacean NMJ and may be meant to counteract the excitatory effects of excess glutamate within the system (Evoy and Kennedy, 1967; Wyttenbach et al., 1999). Nerve cord death was likely the result of a combination of the neurons' inability to maintain high amplitude firing at a high frequency and excessive perturbation of the nerve cord network. The slow decrease in firing amplitude throughout progressive additions of **1** to the preparation support the former explanation. Alternatively, the MSG preparation showed a shift towards baseline activity following long exposure to the amino acid (approximately 40mins to 1hr), representing a homeostatic mechanism. Higher concentrations of MSG may have combated this mechanism to reveal pathologic firing.

The construction of epoxide-based neurotoxins for use against insects and other crop pests provides an advantage for sustainability for future agriculture. While this attempt proved ineffective in the construction of an suicide inhibitor molecule, strong affinity for the binding site was still observed through binding pocket residue perturbations (including residue electron density) and dosage response assays. Construction of more electrophilic epoxides or targeting receptors with greater anionic centers may prove more successful in the future. This class of molecules – both unstable long term and potent in extremely low concentrations – may prove to yield the pesticides that future generations will rely upon for the safe production of the global food supply.

VI. EXPERIMENTAL

Menthol Condensation of 2 to 3:

2.78g (19mmol) of alpha-ketoglutarate (2) was dissolved in 12 mL of HPLC grade benzene with 190mg (1 mmol) of p-toluenesulfonic acid monohydrate, 6.25g (40mmol) L-menthol, and magnesium sulfate. A Dean-Stark apparatus and reflux condenser was attached to the reaction vessel, which was heated to reflux for 22hrs. The reaction was monitored by thin-layer chromatography. Following consumption of starting material, the reaction mixture was diluted with 12 mL EtOAc, and washed 2X100mL of sat. $NaCO_3H$, 50mL brine, and dried over Na_2SO_4. Further purification was performed by column chromatography in 9:1 Hex/EtOAc, yielding 4.27g (55%) of a white solid. **m.p**.43-45°C; **rf** 0.53 in 9:1 Hex/EtOAc; **^{1}H NMR** (300 MHz, Chloroform-d) δ 4.72 (td, J = 10.9, 4.4 Hz, 1H), 4.57 (td, J = 10.9, 4.4 Hz, 1H), 3.02 (t, J = 6.5 Hz, 2H), 2.52 (t, J = 6.5 Hz, 2H), 1.98 – 1.81 (m, 2H), 1.76 (qd, J = 6.8, 2.6 Hz, 2H), 1.66 – 1.56 (m, 1H), 0.83 – 0.74 (m, 11H), 0.65 (dd, J = 7.0, 4.0 Hz, 5H); **^{13}C NMR** (101 MHz, $cdcl_3$) δ 193.06, 171.64, 160.42, 77.48, 77.22, 77.16, 76.84, 74.93, 47.10, 46.85, 40.93, 40.51, 34.53, 34.35, 34.15, 31.58, 31.50, 28.04, 26.40, 26.28, 23.57, 23.40, 22.13, 22.07, 20.86, 20.83, 16.46, 16.28.

Epoxidation of 3 to 4AB:

1.9g (4.5mmol) of 3 was dissolved in 1 mL dry methanol and 5mL dry ether, and cooled to -10°C using a cold-finger in acetone. Approximately 18mL (~4.5mmol) of a freshly prepared diazomethane ether solution at -78°C was added drop wise to the stirring solution of 3. The reaction was placed under a slightly pressurized inert atmosphere and stirred for 24 hrs. Slow addition glacial acetic acid until bubbling ceased quenched the reaction. Toluene was added and

the solvent removed under reduced pressure. Diastereomers were separated using column chromatography in 9:1 Hex/Et_2O to yield 278 mg of highly enriched 4A and 472 mg of partially enriched 4B as clear viscous liquids. **LCMS** – 455.1m/z (455.3 calc).

4A: **r.f**. 0.42 in 8:2 Hex/Et_2O; **^{1}H NMR** (400 MHz, Chloroform-d) δ 4.75 – 4.54 (m, 2H), 3.41 (q, J = 7.0 Hz, 0H), 2.98 (d, J = 5.8 Hz, 1H), 2.74 (dd, J = 5.9, 2.6 Hz, 1H), 2.51 – 2.22 (m, 3H), 2.10 – 1.86 (m, 3H), 1.84 – 1.68 (m, 2H), 1.62 (ddp, J = 13.4, 6.5, 3.3 Hz, 4H), 1.51 – 1.23 (m, 3H), 1.14 (t, J = 7.0 Hz, 1H), 1.07 – 0.85 (m, 6H), 0.84 – 0.75 (m, 2H), 0.70 (dd, J = 7.0, 2.3 Hz, 6H); **^{13}C NMR** (101 MHz, $cdcl_3$) 172.07, 172.05, 169.39, 169.38, 168.62, 77.30, 76.99, 76.67, 75.96, 75.83, 74.37, 65.81, 56.01, 56.00, 51.81, 51.76, 46.95, 46.94, 46.81, 46.74, 40.83, 40.80, 40.59, 40.54, 34.20, 34.08, 34.05, 31.35, 31.34, 29.83, 29.77, 26.44, 26.24, 26.22, 26.19, 23.38, 23.37, 23.07, 21.98, 21.94, 21.92, 20.77, 20.73, 20.67, 16.29, 16.26, 15.95, 15.25.

4B: **r.f**. 0.36 in Hex/Et_2O; **^{1}H NMR** (400 MHz, Chloroform-d) δ 4.63 (dtd, J = 25.7, 10.9, 4.2 Hz, 2H), 3.38 (q, J = 7.1 Hz, 1H), 2.95 (d, J = 5.9 Hz, 1H), 2.71 (dd, J = 5.9, 2.7 Hz, 1H), 2.42 – 2.32 (m, 2H), 2.30 – 2.17 (m, 1H), 2.05 – 1.83 (m, 3H), 1.74 (dddt, J = 13.8, 9.6, 7.0, 2.9 Hz, 2H), 1.59 (dtt, J = 13.2, 6.5, 3.3 Hz, 5H), 1.46 – 1.31 (m, 2H), 1.28 – 1.23 (m, 1H), 1.11 (t, J = 7.1 Hz, 1H), 1.01 – 0.85 (m, 4H), 0.85 – 0.75 (m, 14H), 0.67 (d, J = 7.0 Hz, 7H); **^{13}C NMR** (101 MHz, cdcl3) δ 172.39, 171.92, 169.55, 169.30, 77.48, 77.16, 76.84, 75.81, 75.68, 75.50, 74.25, 73.93, 65.75, 56.61, 55.92, 51.72, 51.66, 51.51, 51.43, 46.94, 46.92, 46.81, 46.75, 46.72, 40.90, 40.80, 40.58, 40.53, 40.50, 34.20, 34.07, 31.68, 31.33, 30.67, 29.79, 29.73, 26.78, 26.45, 26.42, 26.22, 26.18, 26.14, 23.55, 23.39, 23.36, 23.08, 22.60, 21.97, 21.92, 20.75, 20.71, 20.68, 20.64, 20.51, 16.28, 16.25, 15.94, 15.23.

Deprotection of 4 to 1:

440 mg (1mmol) of 4B was dissolved in 10mL THF, 2mL methanol, and 5mL distilled water. 300 mg (7mmol) of lithium hydroxide monohydrate was added and the solution stirred at room temperature for 48 hrs until the TLC in 1:9 MeOH/DCM showed full consumption of mono and bis-protected reactant. The solution was washed with 50mL ether, and brought to a pH of ~2 using 1M HCl. The solution became opaque and was washed again 2x50mL EtOAc. Toluene was added and the solvent removed under reduced pressure. 480 mg of 1B with LiCl (94%) was recovered as a white crystalline solid. **m.p.** 85-87°C; **^{1}H NMR** (300 MHz, Deuterium Oxide) δ 3.89 (d, J = 11.6 Hz, 1H), 3.68 (d, J = 11.7 Hz, 1H), 2.69 – 2.31 (m, 2H), 2.19 – 1.88 (m, 2H).

VII. References

Adams PD, Afonine PV, Bunkóczi G, Chen VB, Davis IW, Echols N, Headd JJ, Hung L-W, Kapral GJ, Grosse-Kunstleve RW, McCoy AJ, Moriarty NW, Oeffner R, Read RJ, Richardson DC, Richardson JS, Terwilliger TC, Zwart PH (2010) PHENIX: a comprehensive Python-based system for macromolecular structure solution. Acta Crystallogr D Biol Crystallogr 66:213–221.

Afonine PV, Grosse-Kunstleve RW, Echols N, Headd JJ, Moriarty NW, Mustyakimov M, Terwilliger TC, Urzhumtsev A, Zwart PH, Adams PD (2012) Towards automated crystallographic structure refinement with *phenix.refine*. Acta Crystallogr D Biol Crystallogr 68:352–367.

Armstrong N, Gouaux E (2000) Mechanisms for activation and antagonism of an AMPA-sensitive glutamate receptor: crystal structures of the GluR2 ligand binding core. Neuron 28:165–181.

Atwood HL, Cooper RL (1996) Assessing ultrastructure of crustacean and insect neuromuscular junctions. J Neurosci Methods 69:51–58.

Battye TGG, Kontogiannis L, Johnson O, Powell HR, Leslie AGW (2011) *iMOSFLM*: a new graphical interface for diffraction-image processing with *MOSFLM*. Acta Crystallogr D Biol Crystallogr 67:271–281.

Casida JE, Durkin KA (2013) Neuroactive insecticides: targets, selectivity, resistance, and secondary effects. Annu Rev Entomol 58:99–117.

Casida JE, Quistad GB (1998) Golden age of insecticide research: past, present, or future? Annu Rev Entomol 43:1–16.

Chen VB, Arendall WB, Headd JJ, Keedy DA, Immormino RM, Kapral GJ, Murray LW, Richardson JS, Richardson DC (2010) MolProbity: all-atom structure validation for macromolecular crystallography. Acta Crystallogr D Biol Crystallogr 66:12–21.

Cornell Policy Library (2012) Policy 1.4 Care and Use of Animals in Research and Teaching. Available at: http://www.dfa.cornell.edu/cms/treasurer/policyoffice/policies/volumes/academic/upload/vol1_4.pdf [Accessed April 5, 2014].

Davis RL, Jensen KL, Gschwend B, Jørgensen KA (2014) On the Mechanism of the Organocatalytic Asymmetric Epoxidation of α,β-Unsaturated Aldehydes. Chem – Eur J 20:64–67.

Defeudis FV (1970) Role of the Perineural Sheath of Peripheral Nerve on Fluxes of L-Glutamate in vitro. Nature 227:854–855.

Denmark SE, Wu ZC (1999) The development of chiral, nonracemic dioxiranes for the catalytic, enantioselective epoxidation of alkenes. Synlett:847–859.

Dingledine R, Borges K, Bowie D, Traynelis SF (1999) The Glutamate Receptor Ion Channels. Pharmacol Rev 51:7–62.

Dos Santos ML, de Magalhães GC (1991) Synthesis of 2-Hydroxy-3-methyl-2-cyclo-pentenone, Corylone, from 2-Ketoglutaric Acid. Synth Commun 21:1783–1788.

Emsley P, Lohkamp B, Scott WG, Cowtan K (2010) Features and development of *Coot*. Acta Crystallogr D Biol Crystallogr 66:486–501.

Evoy WH, Kennedy D (1967) The central nervous organization underlying control of antagonistic muscles in the crayfish. I. types of command fibers. J Exp Zool 165:223–238.

FAO (2009) FAO's Director-General on How to Feed the World in 2050. Popul Dev Rev 35:837–839.

Grabowska A, Nowicki M, Kwinta J (2011) Glutamate dehydrogenase of the germinating triticale seeds: gene expression, activity distribution and kinetic characteristics. Acta Physiol Plant 33:1981–1990.

Groebe DR, Abramson SN (1995) Lophotoxin Is a Slow Binding Irreversible Inhibitor of Nicotinic Acetylcholine Receptors. J Biol Chem 270:281–286.

Grond S, Sablotzki A (2004) Clinical pharmacology of tramadol. Clin Pharmacokinet 43:879–923.

Hollmann M, Heinemann S (1994) Cloned Glutamate Receptors. Annu Rev Neurosci 17:31–108.

Krintel C, Frydenvang K, Olsen L, Kristensen MT, de Barrios O, Naur P, Francotte P, Pirotte B, Gajhede M, Kastrup JS (2012) Thermodynamics and structural analysis of positive allosteric modulation of the ionotropic glutamate receptor GluA2. Biochem J 441:173–178.

Landvater R, Galanko MB (2013) Effect of 2-Isohexoxiranedioic Acid and D-Aspartate on the Crayfish Neuromuscular Junction and Nerve Cord. BioNB 4910.

Lichtor PA, Miller SJ (2014) Experimental Lineage and Functional Analysis of a Remotely Directed Peptide Epoxidation Catalyst. J Am Chem Soc Available at: http://dx.doi.org/10.1021/ja410567a [Accessed April 3, 2014].

Matsumoto K, Harada K (1966) Stereoselective Syntheses of Optically Active Amino Acids from Menthyl Esters of α-Keto Acids1. J Org Chem 31:1956–1958.

Milewska MJ, Prokop M, Gabriel I, Wojciechowski M, Milewski S (2012) Antifungal activity of homoaconitate and homoisocitrate analogs. Mol Basel Switz 17:14022–14036.

Nicolaou KC, Estrada AA, Zak M, Lee SH, Safina BS (2005) A Mild and Selective Method for the Hydrolysis of Esters with Trimethyltin Hydroxide. Angew Chem Int Ed 44:1378–1382.

Oerke E-C (2006) Crop losses to pests. J Agric Sci 144:31–43.

Popp J, Pető K, Nagy J (2013) Pesticide productivity and food security. A review. Agron Sustain Dev 33:243–255.

Rupp B (2010) Biomolecular crystallography: principles, practice, and application to structural biology. New York: Garland Science.

Schrodinger (2010) The PyMOL Molecular Graphics System, Version 1.3r1.

Suchanek B, Seeburg PH, Sprengel R (1995) Gene structure of the murine N-methyl D-aspartate receptor subunit NR2C. J Biol Chem 270:41–44.

Wauchope RD (1978) The Pesticide Content of Surface Water Draining from Agricultural Fields—A Review1. J Environ Qual 7:459.

WHO (1979) DDT and its derivatives. Geneva : [Albany, N.Y: World Health Organization ; obtainable from WHO Publications Centre USA].

Winn MD, Ballard CC, Cowtan KD, Dodson EJ, Emsley P, Evans PR, Keegan RM, Krissinel EB, Leslie AGW, McCoy A, McNicholas SJ, Murshudov GN, Pannu NS, Potterton EA,

Powell HR, Read RJ, Vagin A, Wilson KS (2011) Overview of the CCP4 suite and current developments. Acta Crystallogr Sect D 67:235–242.

Wyttenbach RA, Johnson BR, Hoy RR, Sinauer Associates (1999) Crawdad a CD-ROM lab manual for neurophysiology. Sunderland, MA: Sinauer Associates.

VIII. Acknowledgements

There are quite a few fantastic scientists to whom I owe a great deal of gratitude and without whom this project would not have been completed. First and foremost I would like to thank Professor Lewis. In order to accurately describe the assistance I have received both in synthetic chemistry and my education more generally, I would likely need to write another 28 pages. My appreciation can truly not be understated. I would like to thank the Lewis group – Megan Hinze, Tony Tierno, Matt Moschitto, Anirudra Paul, Dave Vaccarello, and Jessica Daughtry – for their assistance and advice in the synthesis. I would like to thank Professor Ahmed Ahmed for providing GluR2 S1S2 crystals. I would like to thank Dr. Michael Fenwick for numerous hours of assistance during diffraction data collection and structure elucidation. I would like to thank Professor Ealick and the staff at NE-CAT – specifically Dr. Frank Murphy – for generously donating synchrotron beam time for my project and for their assistance. I would to thank Dr. Bruce Johnson for generously allowing my use of electrophysiological equipment, crayfish, and for hours of invaluable training. I would like to thank my colleague Brian Morris, who I respect immensely, for his assistance in data collection on the crayfish model. I would like to thank Shane Peace for his assistance in interpreting neurophysiologic data. Finally, I would like to thank my friends and family for their support in ways too numerous to describe.

IX. Supplemental Information

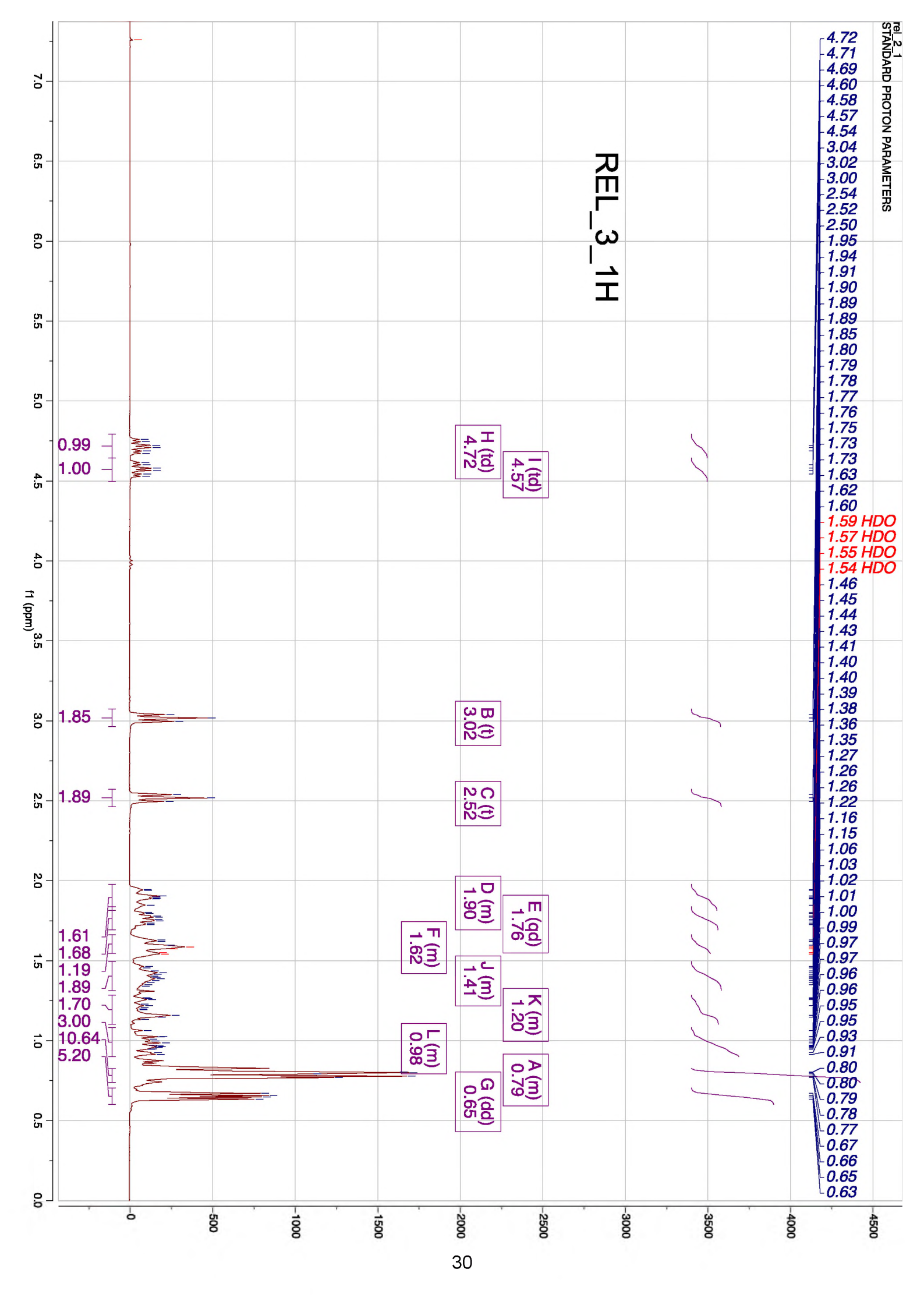
REL_3_1H
rel_2_1
STANDARD PROTON PARAMETERS
f1 (ppm)
H (td) 4.72
I (td) 4.57
B (t) 3.02
C (t) 2.52
D (m) 1.90
E (qd) 1.76
F (m) 1.62
J (m) 1.41
K (m) 1.20
L (m) 0.98
A (m) 0.79
G (dd) 0.65
0.99
1.00
1.85
1.89
1.61
1.68
1.19
1.89
1.70
3.00
10.64
5.20
1.59 HDO
1.57 HDO
1.55 HDO
1.54 HDO

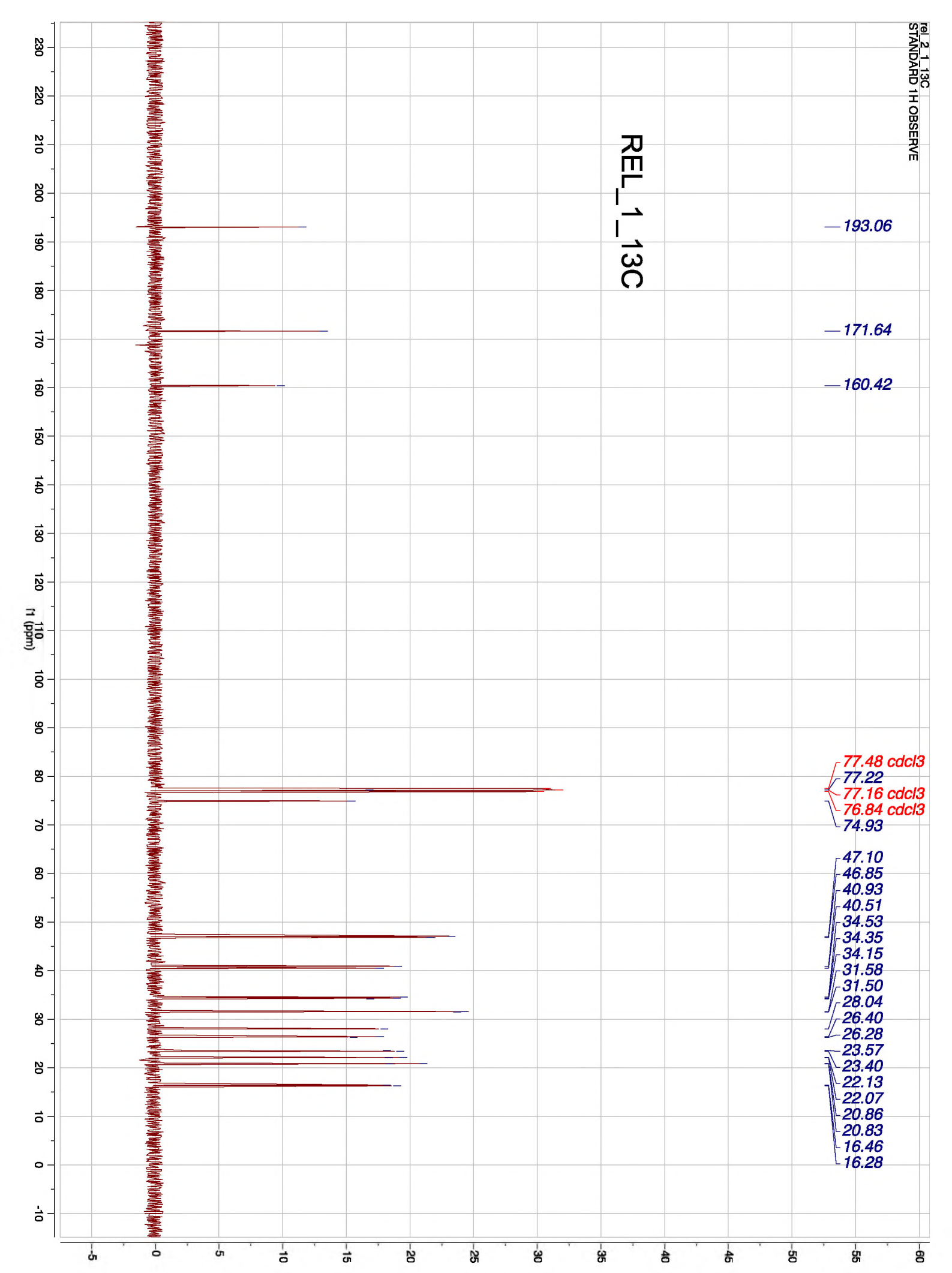
rel_2_1_13C
STANDARD 1H OBSERVE
REL_1_13C
193.06
171.64
160.42
77.48 cdcl3
77.22
77.16 cdcl3
76.84 cdcl3
74.93
47.10
46.85
40.93
40.51
34.53
34.35
34.15
31.58
31.50
28.04
26.40
26.28
23.57
23.40
22.13
22.07
20.86
20.83
16.46
16.28
f1 (ppm)

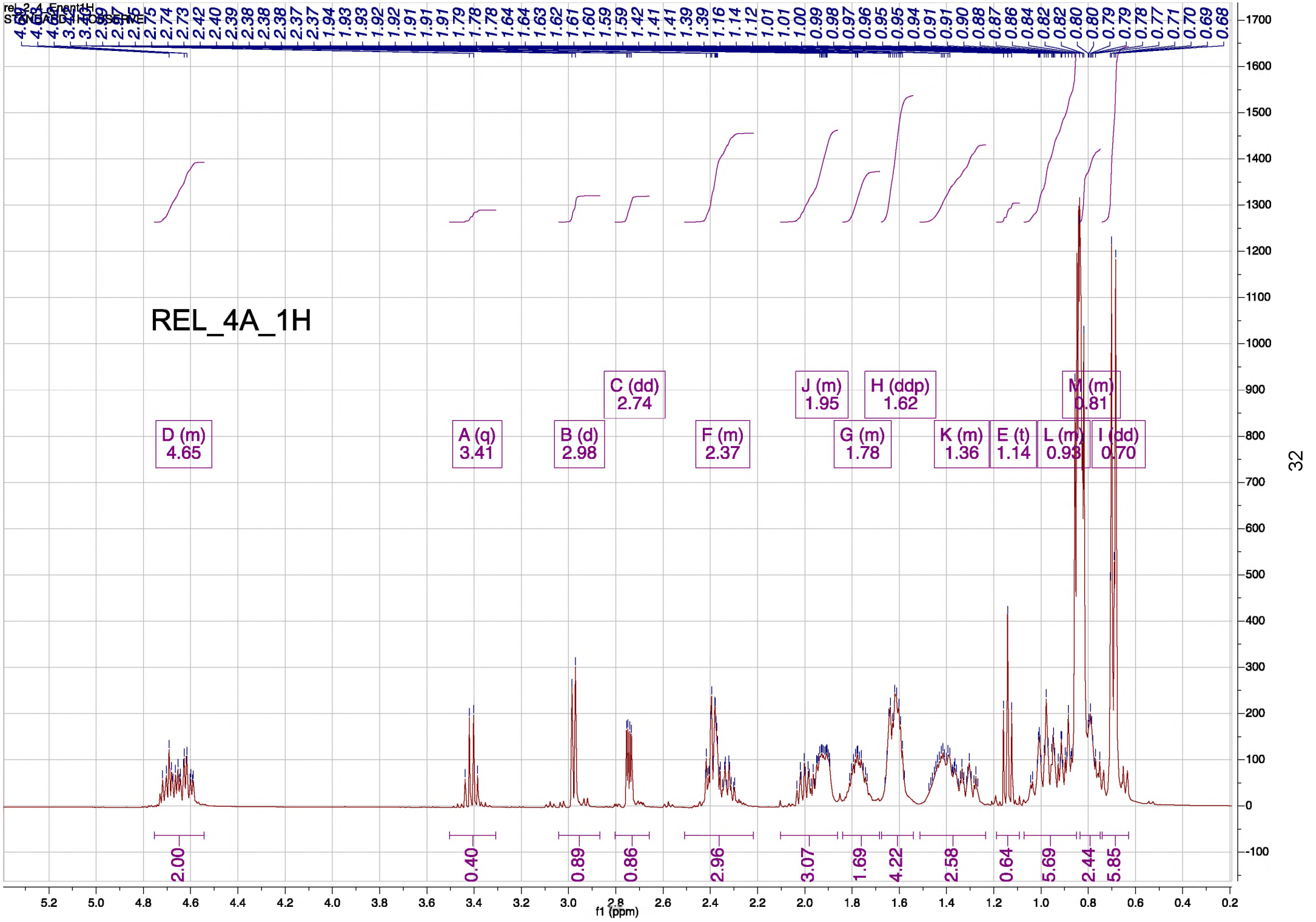
REL_4A_1H
D (m) 4.65
A (q) 3.41
B (d) 2.98
C (dd) 2.74
F (m) 2.37
J (m) 1.95
G (m) 1.78
H (ddp) 1.62
K (m) 1.36
E (t) 1.14
L (m) 0.93
I (dd) 0.70
M (m) 0.81
2.00
0.40
0.89
0.86
2.96
3.07
1.69
4.22
2.58
0.64
5.69
2.44
5.85
f1 (ppm)

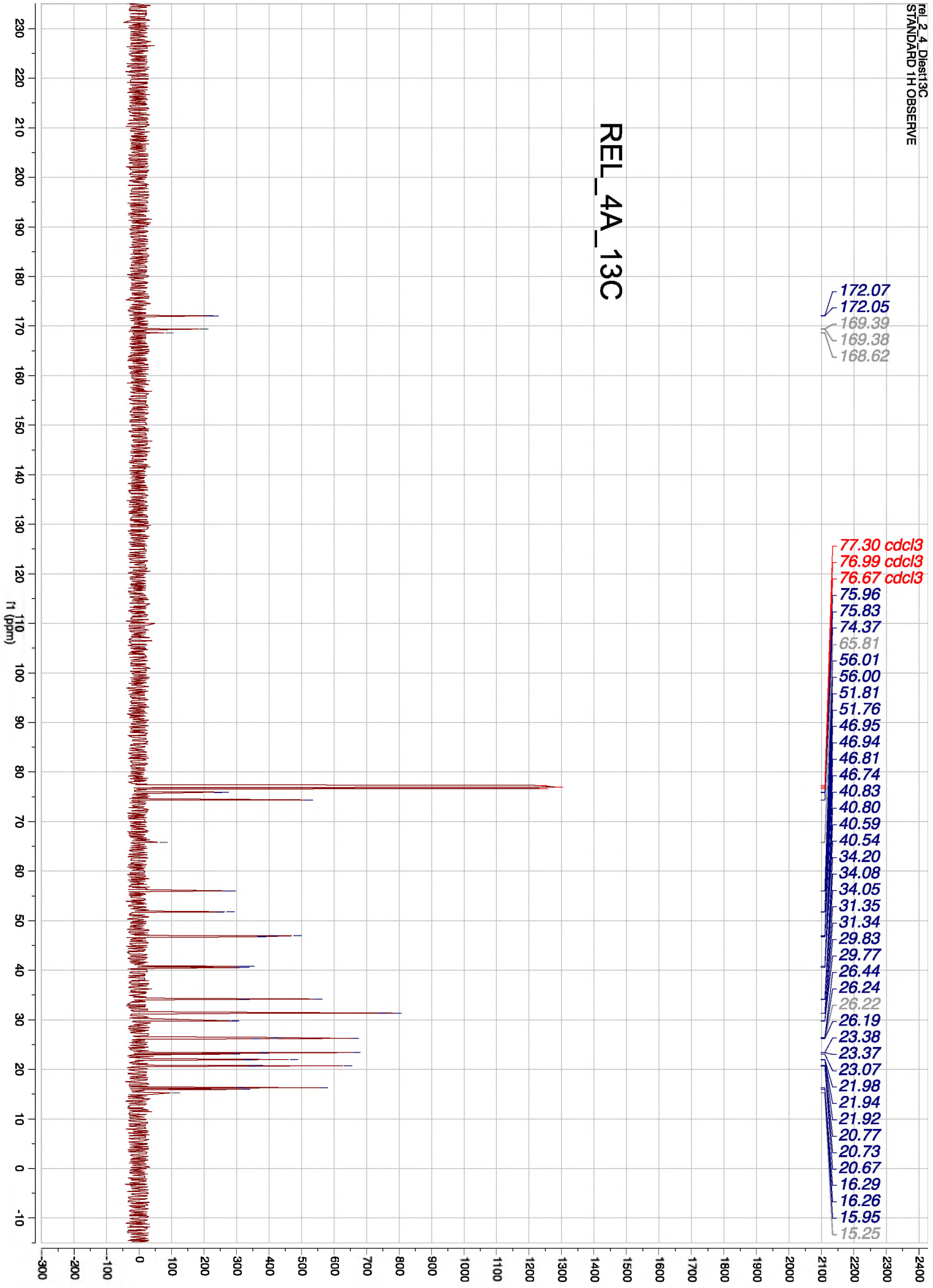
rel_2_4_Diesl13C
STANDARD 1H OBSERVE
REL_4A_13C
172.07
172.05
169.39
169.38
168.62
77.30 cdcl3
76.99 cdcl3
76.67 cdcl3
75.96
75.83
74.37
65.81
56.01
56.00
51.81
51.76
46.95
46.94
46.81
46.74
40.83
40.80
40.59
40.54
34.20
34.08
34.05
31.35
31.34
29.83
29.77
26.44
26.24
26.22
26.19
23.38
23.37
23.07
21.98
21.94
21.92
20.77
20.73
20.67
16.29
16.26
15.95
15.25
f1 (ppm)

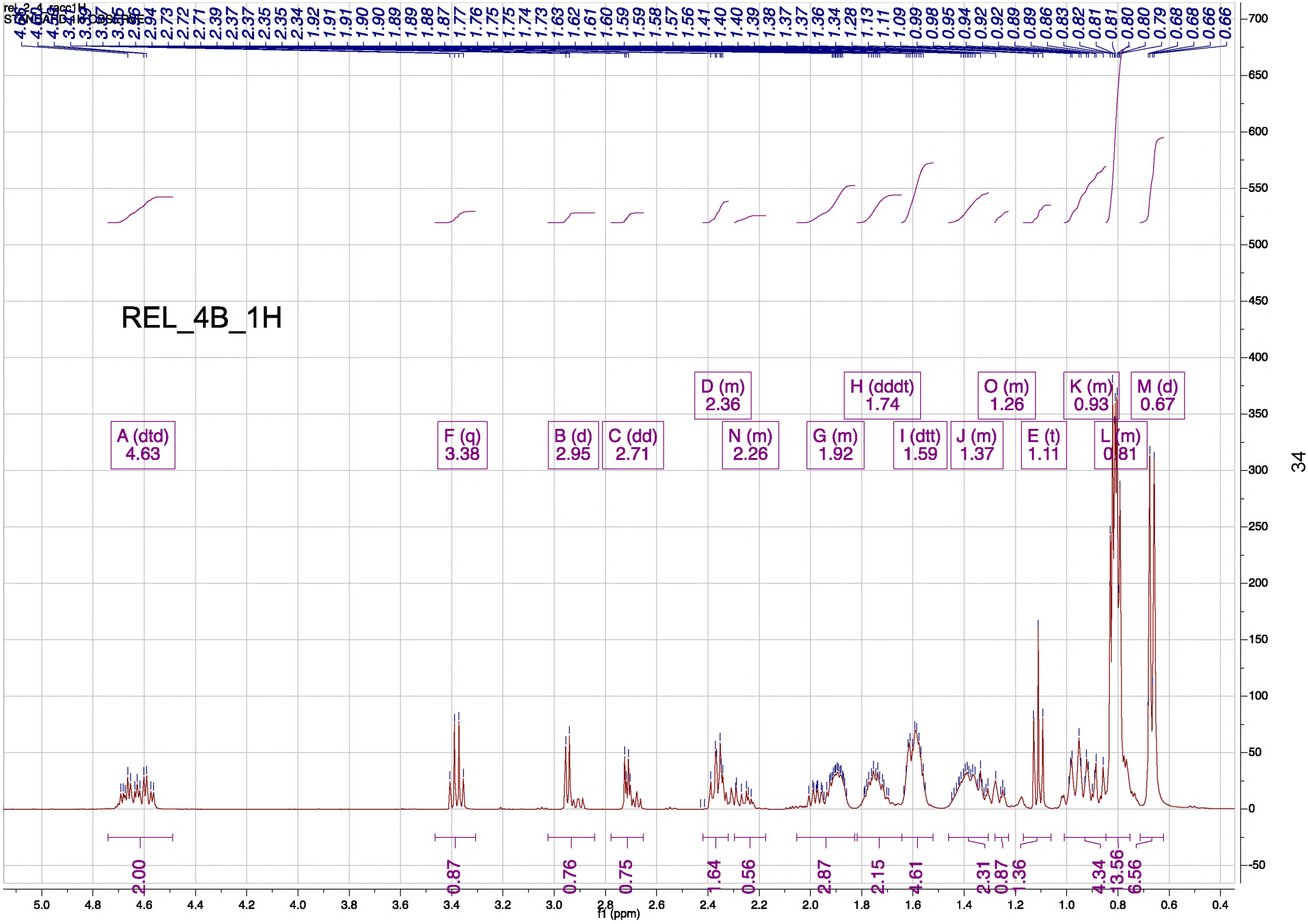
REL_4B_1H
A (dtd) 4.63
F (q) 3.38
B (d) 2.95
C (dd) 2.71
D (m) 2.36
N (m) 2.26
G (m) 1.92
H (dddt) 1.74
I (dtt) 1.59
J (m) 1.37
O (m) 1.26
E (t) 1.11
K (m) 0.93
L (m) 0.81
M (d) 0.67
2.00
0.87
0.76
0.75
1.64
0.56
2.87
2.15
4.61
2.31
0.87
1.36
4.34
13.56
6.56
f1 (ppm)
34

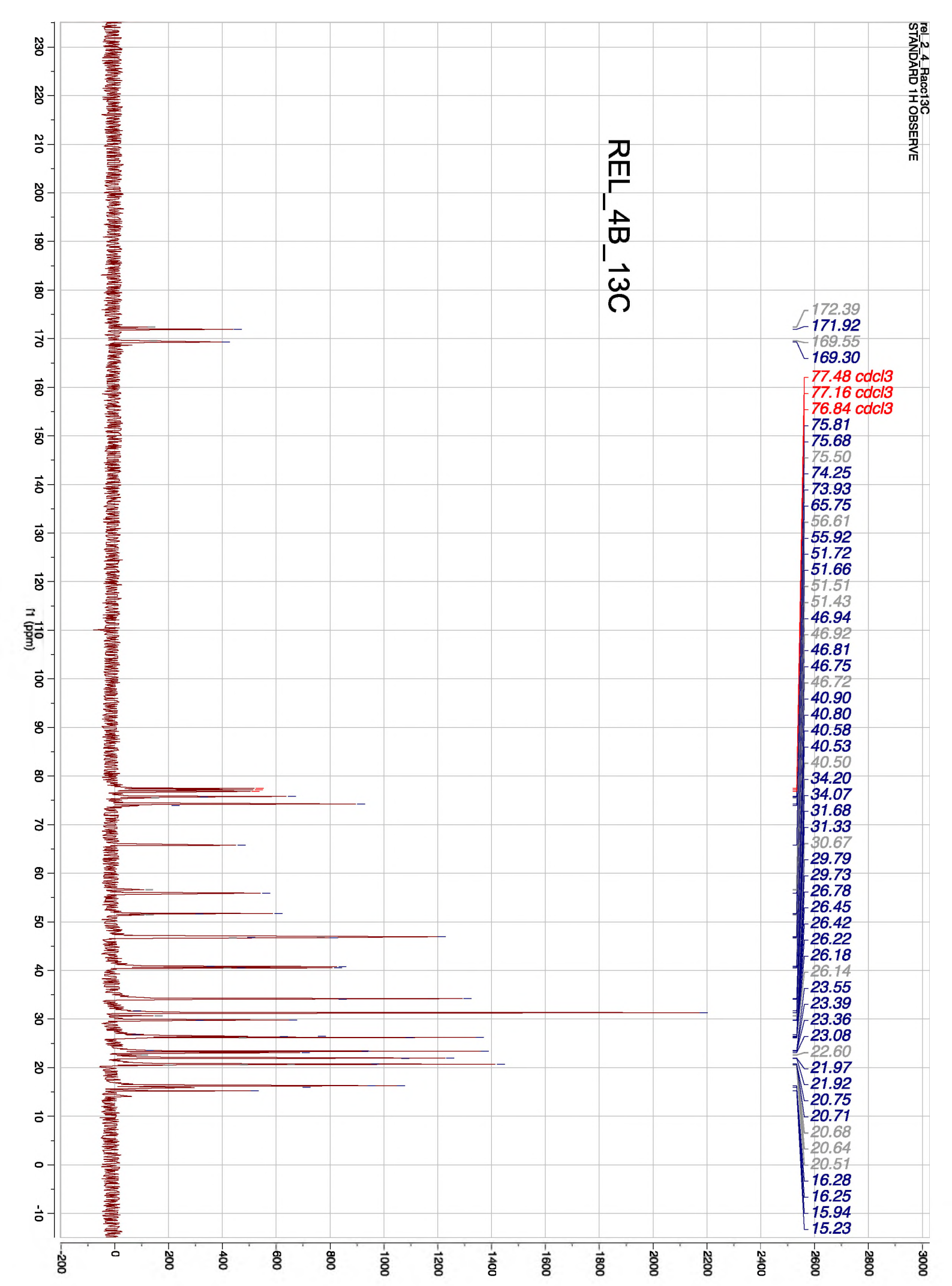
rel_2_4_Racc13C
STANDARD 1H OBSERVE
REL_4B_13C
f1 (ppm)
172.39
171.92
169.55
169.30
77.48 cdcl3
77.16 cdcl3
76.84 cdcl3
75.81
75.68
75.50
74.25
73.93
65.75
56.61
55.92
51.72
51.66
51.51
51.43
46.94
46.92
46.81
46.75
46.72
40.90
40.80
40.58
40.53
40.50
34.20
34.07
31.68
31.33
30.67
29.79
29.73
26.78
26.45
26.42
26.22
26.18
26.14
23.55
23.39
23.36
23.08
22.60
21.97
21.92
20.75
20.71
20.68
20.64
20.51
16.28
16.25
15.94
15.23

MS Spectrum

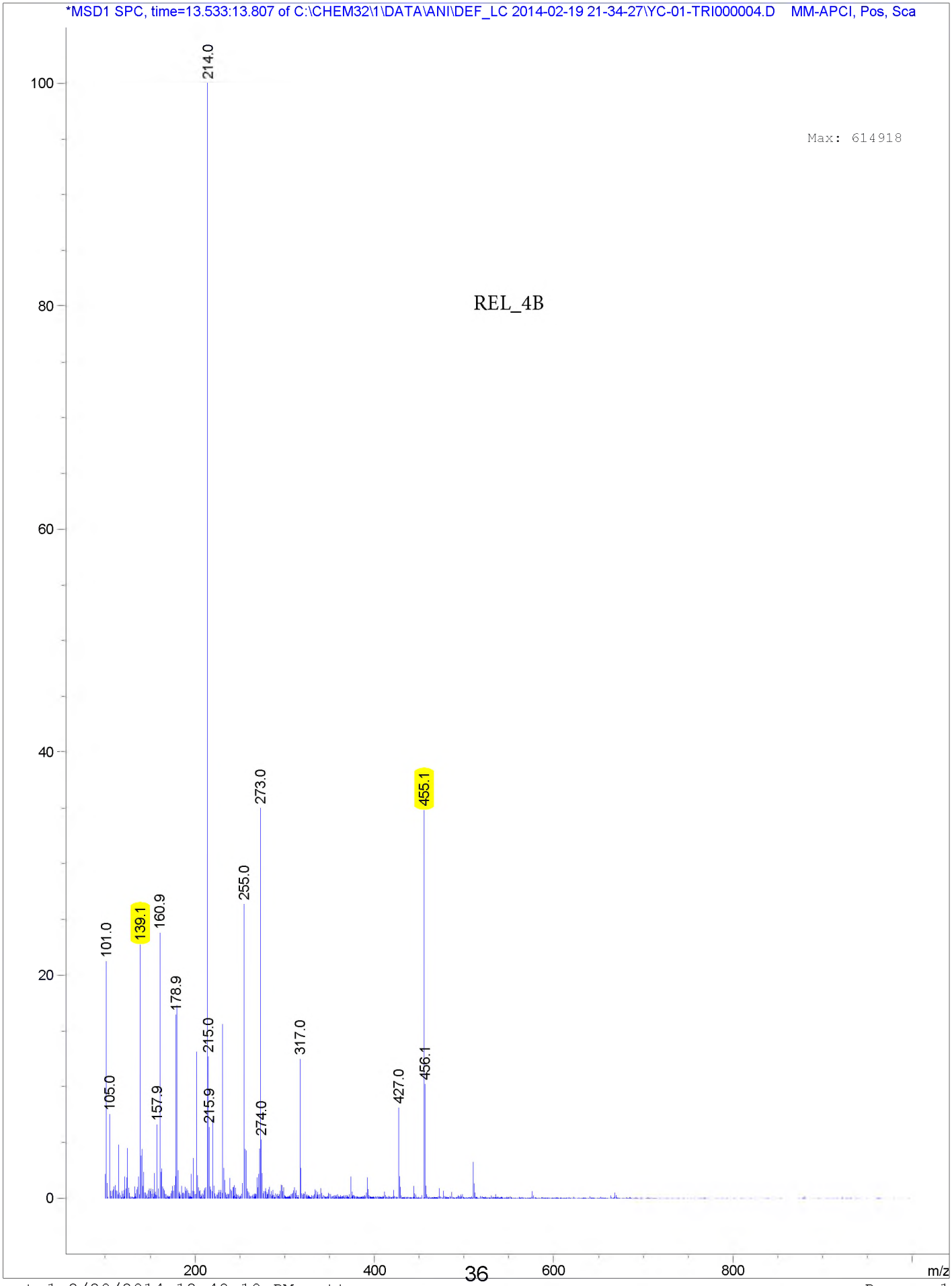
*MSD1 SPC, time=13.533:13.807 of C:\CHEM32\1\DATA\ANI\DEF_LC 2014-02-19 21-34-27\YC-01-TRI000004.D MM-APCI, Pos, Sca
Max: 614918
REL_4B
214.0
455.1
273.0
255.0
139.1
160.9
101.0
178.9
215.0
317.0
105.0
157.9
215.9
274.0
427.0
456.1
100
80
60
40
20
0
200
400
600
800
m/z

rel_2_12_aqeous
STANDARD PROTON PARAMETERS

^{1}H NMR (300 MHz, Deuterium Oxide) δ 3.89 (d, J = 11.6 Hz, 1H), 3.68 (d, J = 11.7 Hz, 1H), 2.69 – 2.31 (m, 2H), 2.19 – 1.88 (m, 2H).

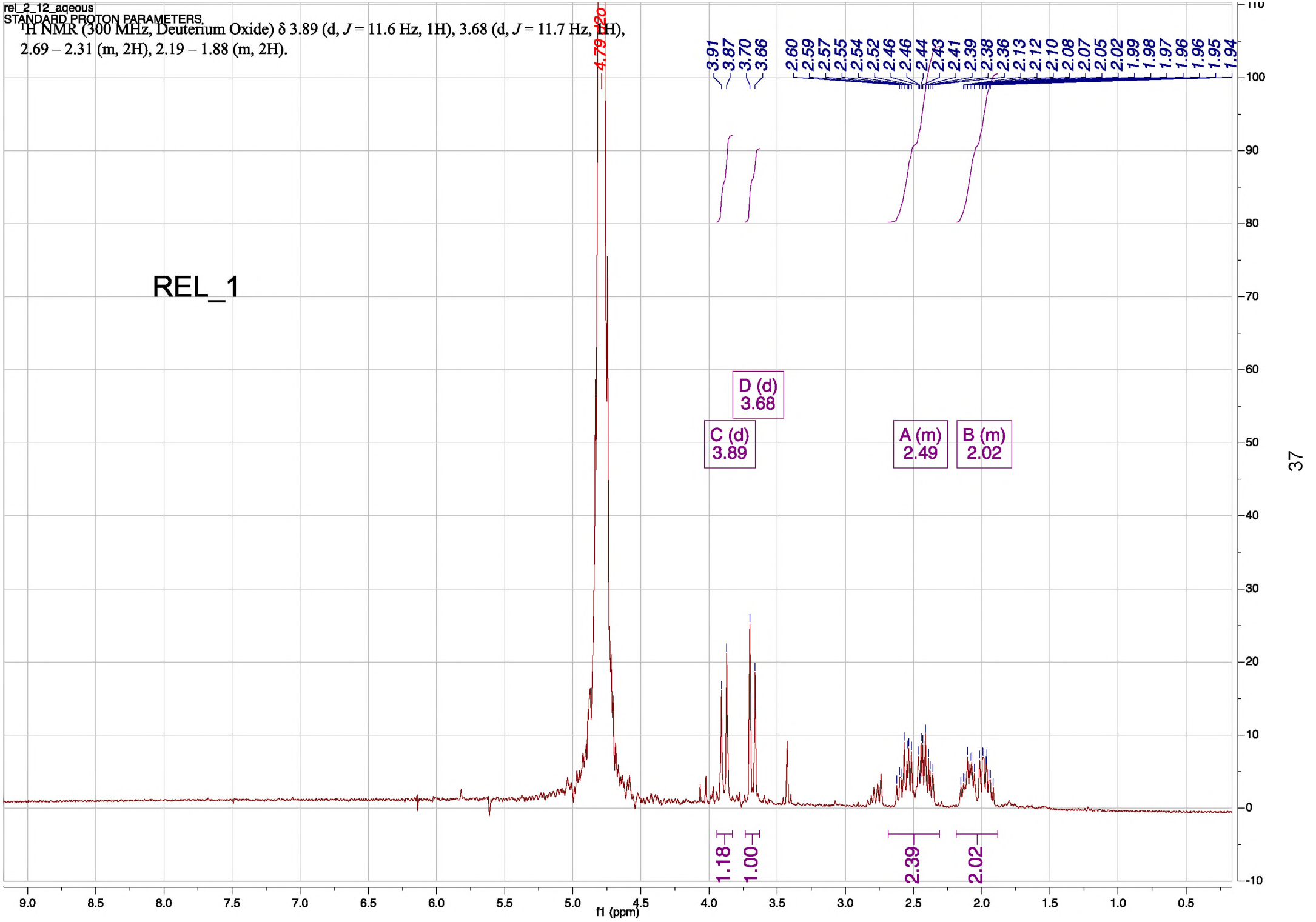

Crystal Collection Statistic by XTRIAGE

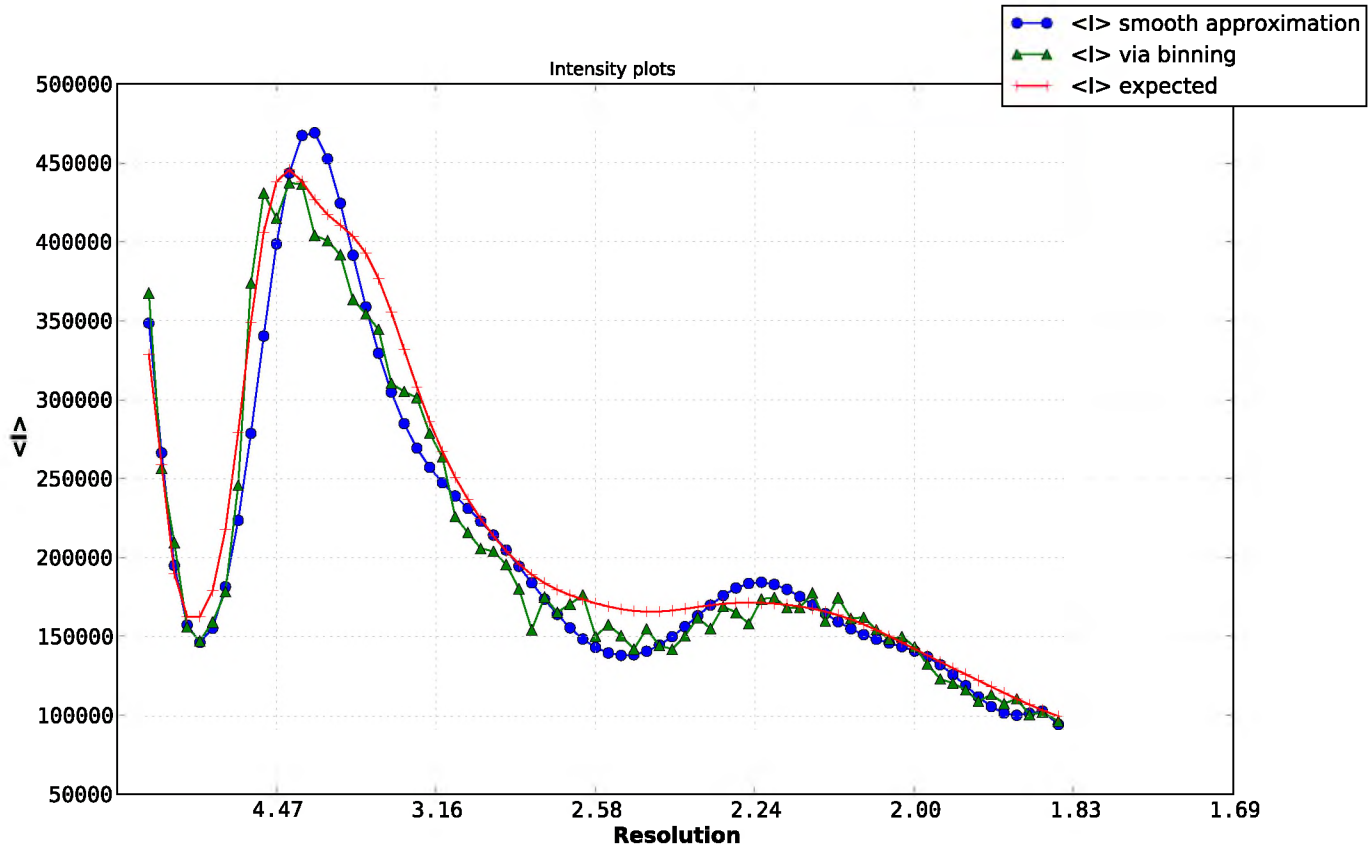

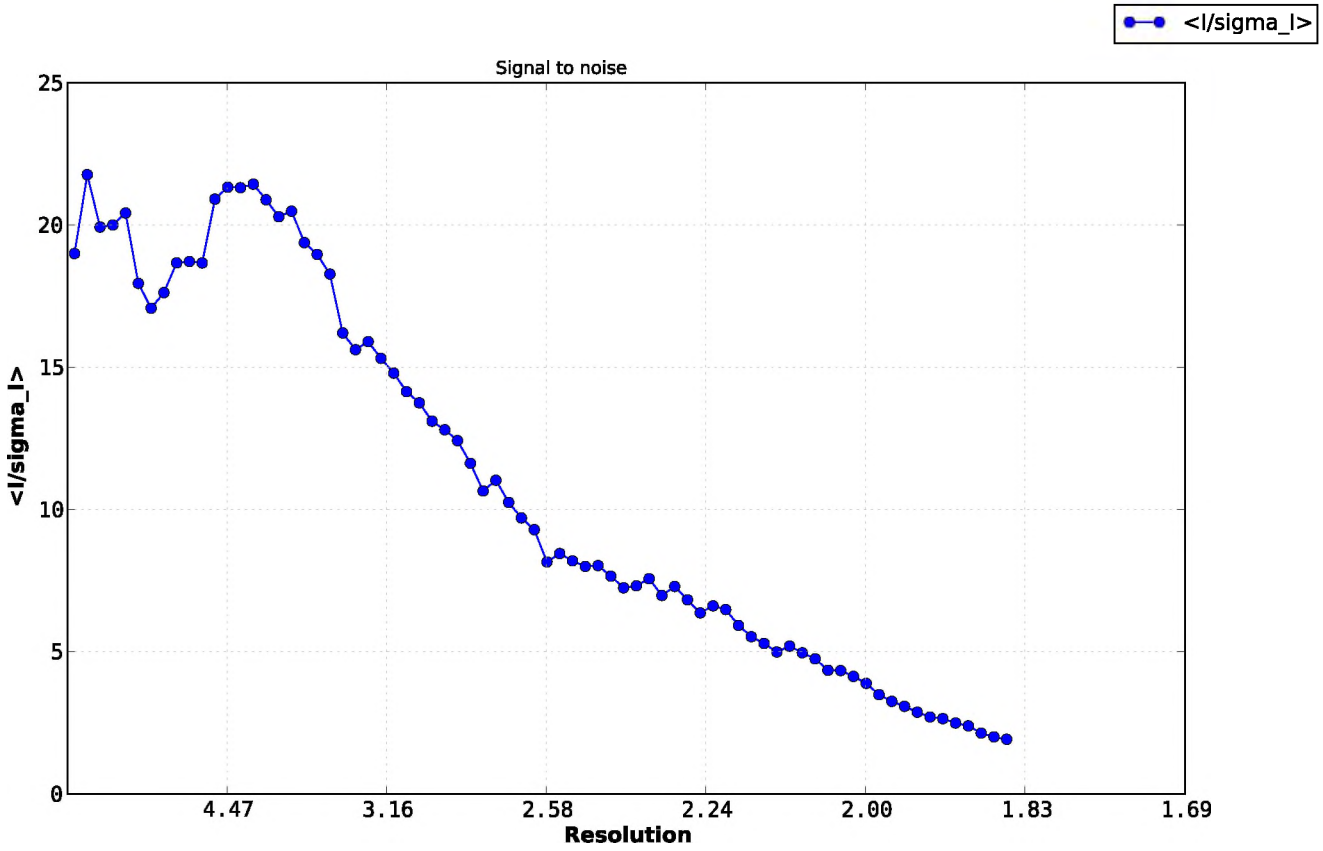

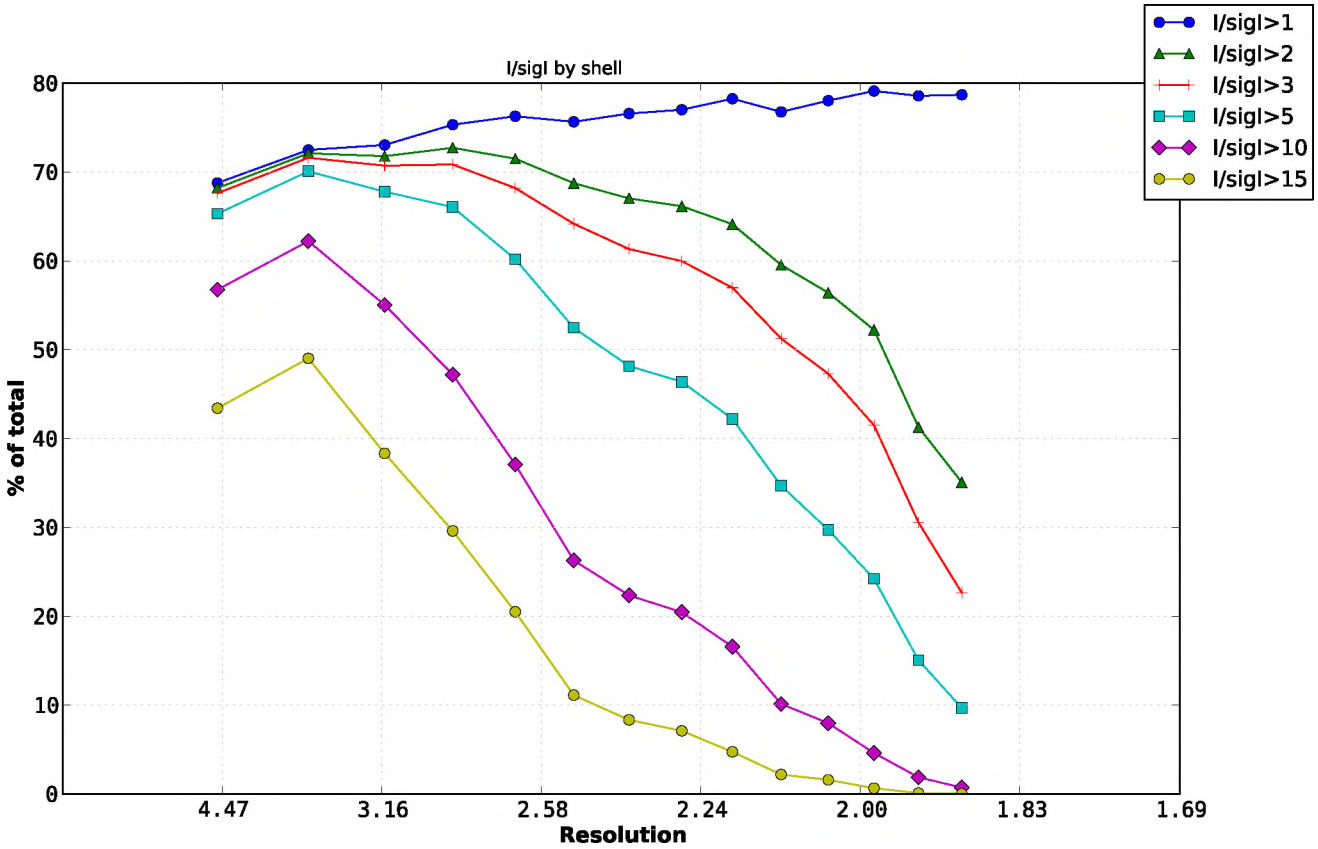
I/sigI by shell
I/sigI>1
I/sigI>2
I/sigI>3
I/sigI>5
I/sigI>10
I/sigI>15
% of total
Resolution
80
70
60
50
40
30
20
10
0
4.47
3.16
2.58
2.24
2.00
1.83
1.69

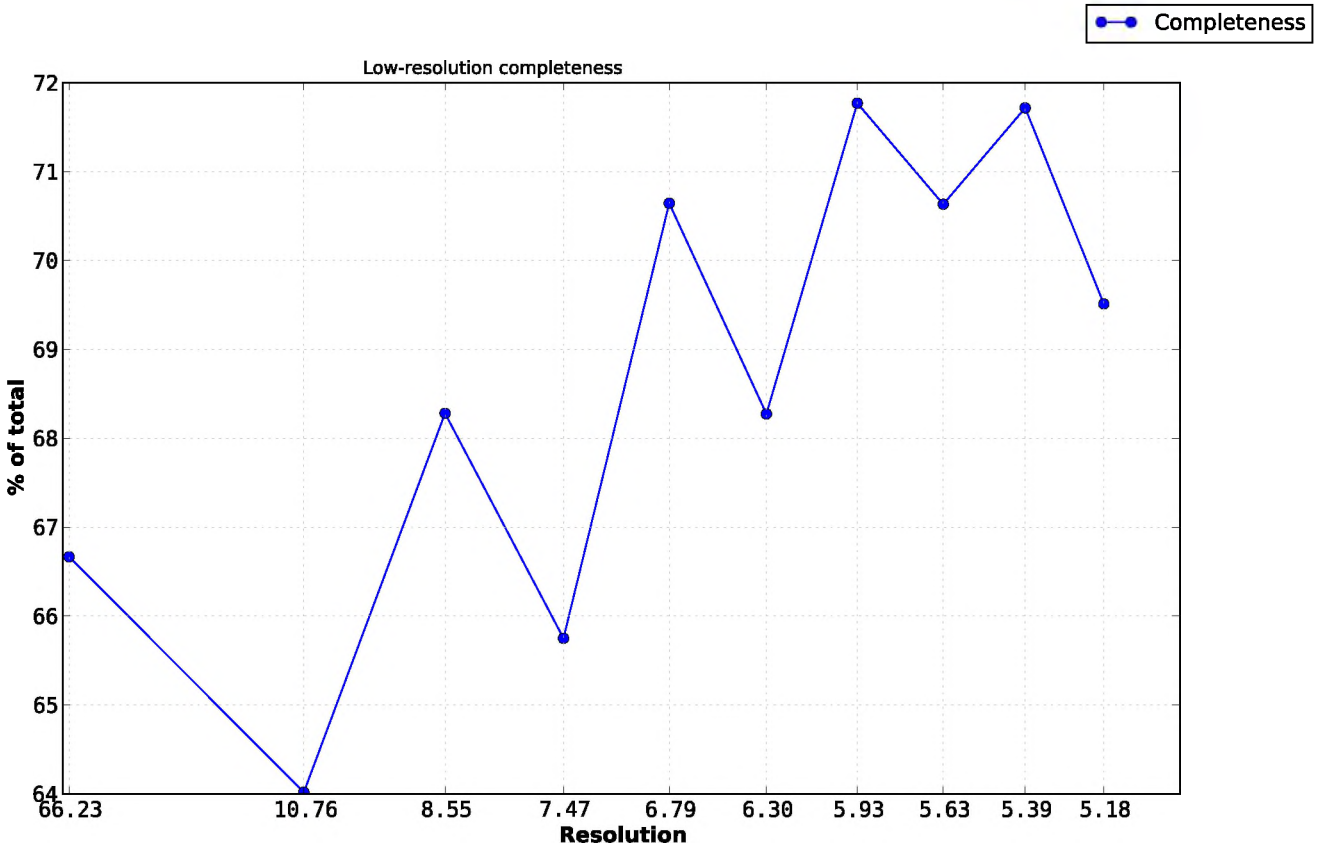
Completeness
Low-resolution completeness
% of total
Resolution
72
71
70
69
68
67
66
65
64
66.23
10.76
8.55
7.47
6.79
6.30
5.93
5.63
5.39
5.18

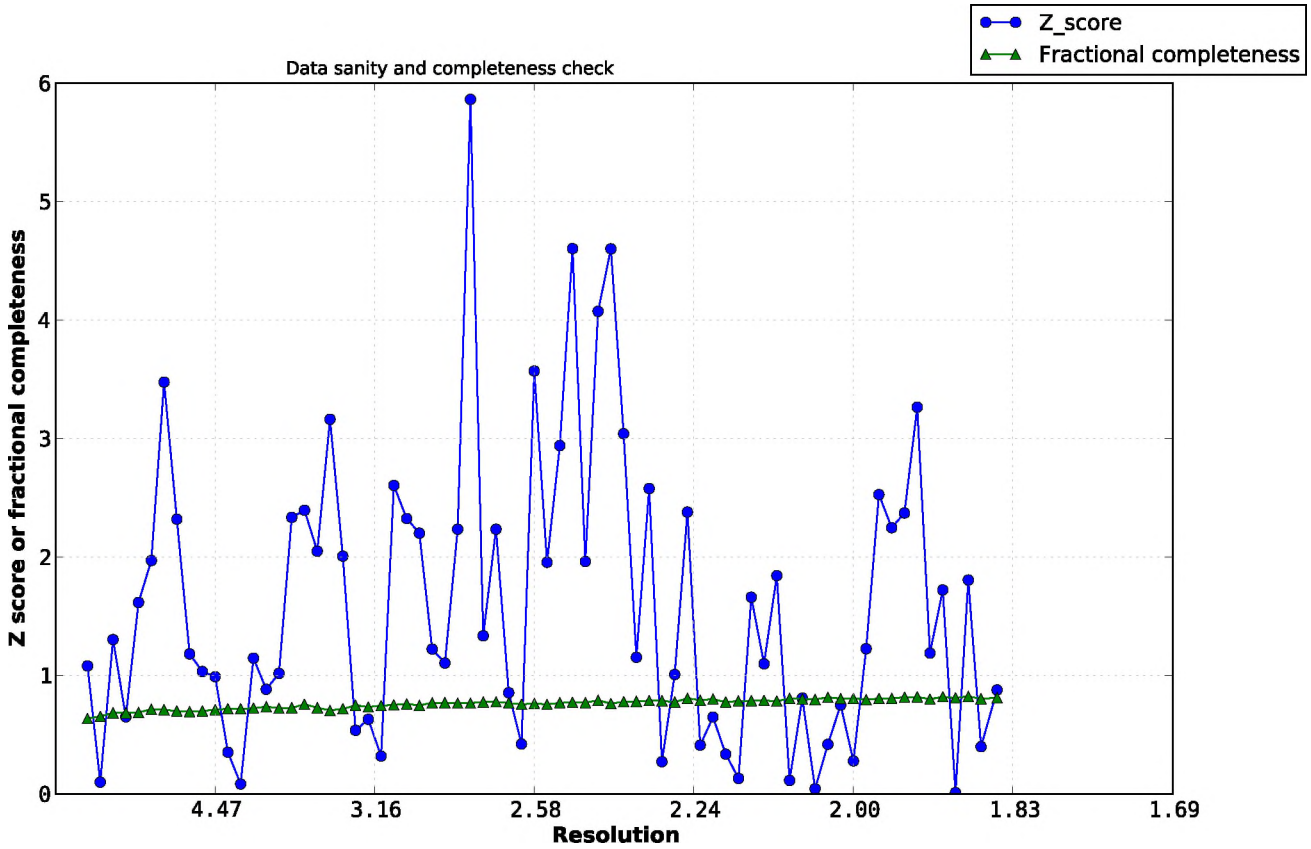
Z_score
Fractional completeness
Data sanity and completeness check
Z score or fractional completeness
Resolution
0
1
2
3
4
5
6
4.47
3.16
2.58
2.24
2.00
1.83
1.69

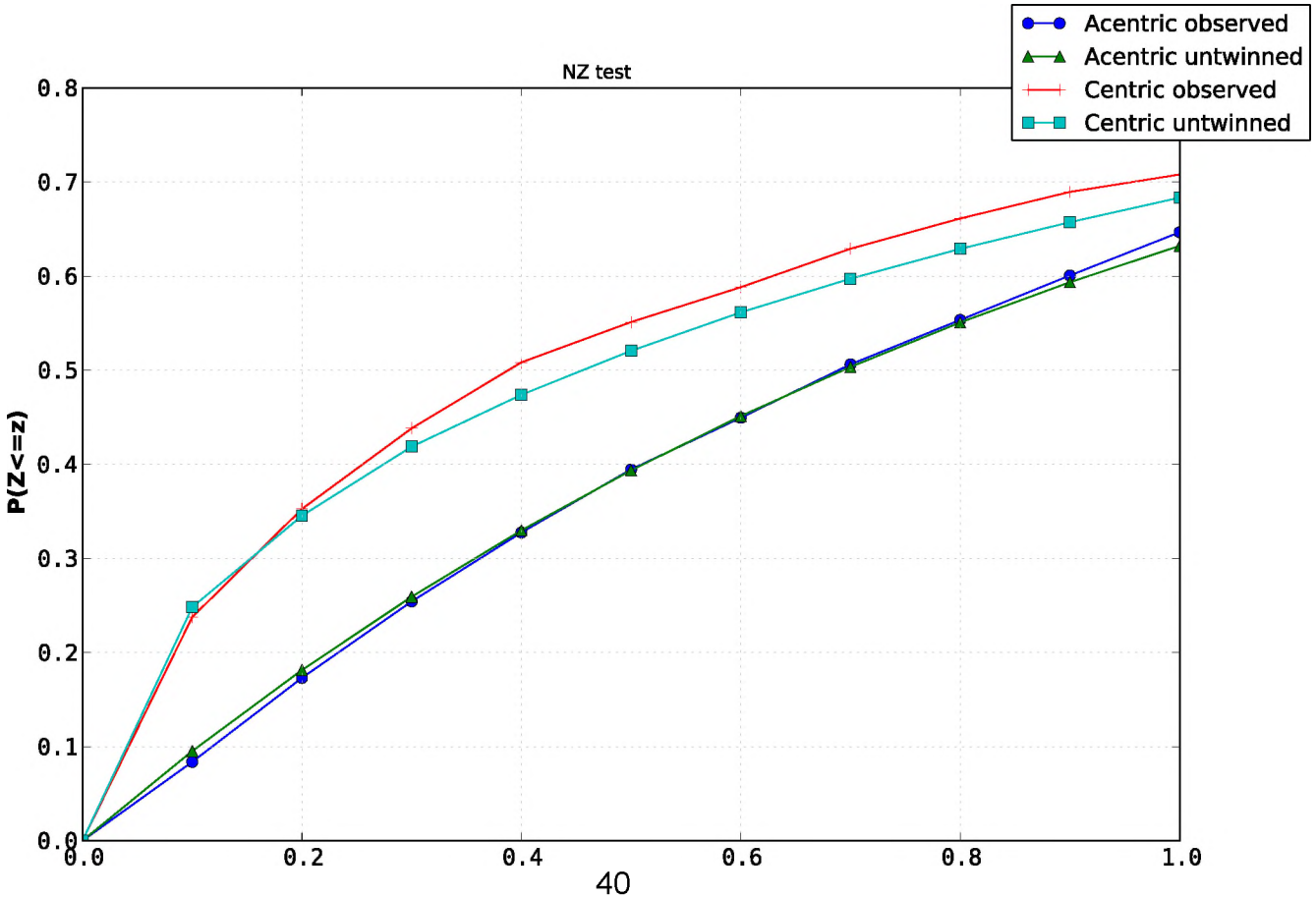
Acentric observed
Acentric untwinned
Centric observed
Centric untwinned
NZ test
P(Z<=z)
0.0
0.1
0.2
0.3
0.4
0.5
0.6
0.7
0.8
0.0
0.2
0.4
0.6
0.8
1.0

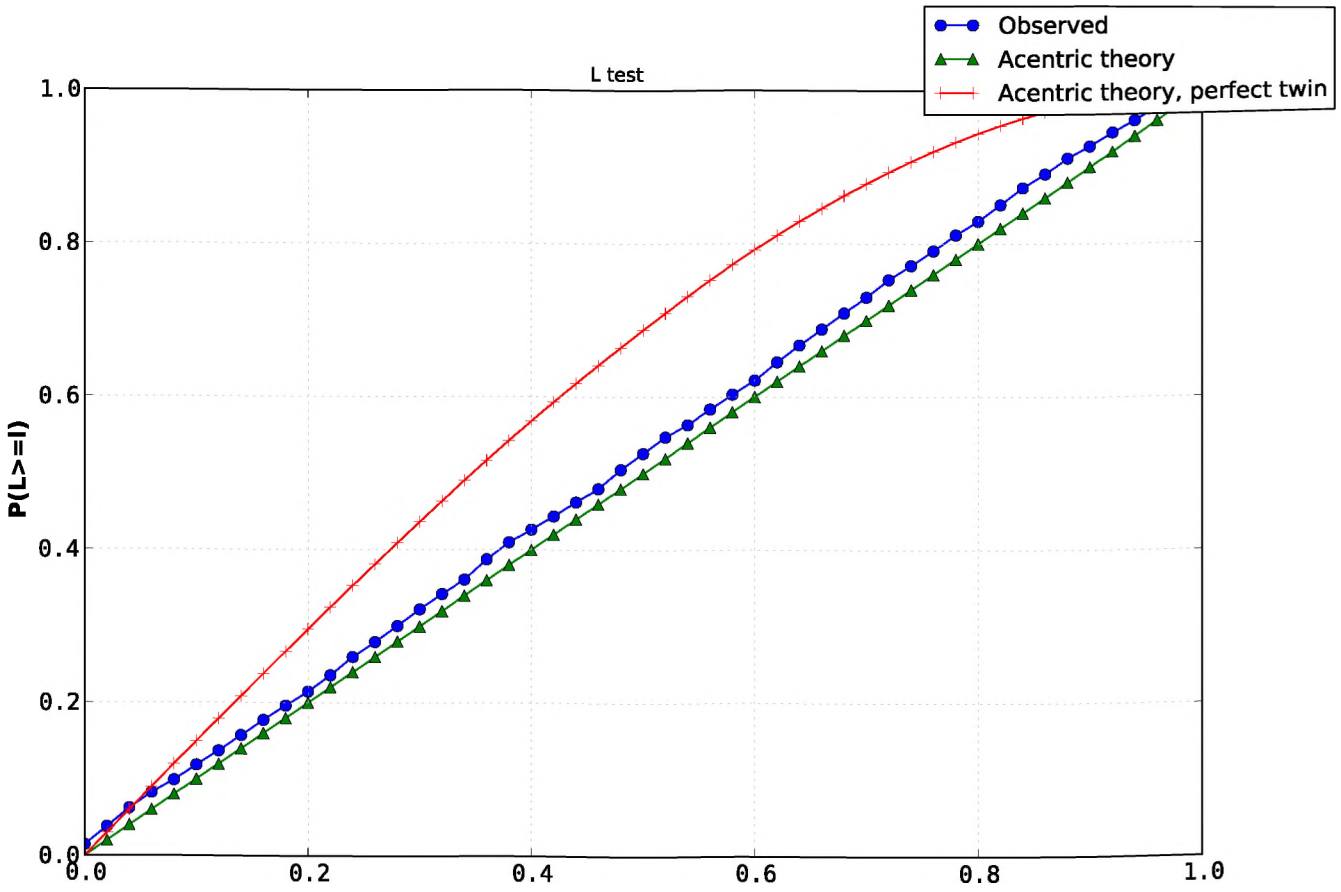

Data Quality:
Data competeness worse than 90% overall.

Twinning:
No Merohedral or pseudo-merohedral twin laws possible in this lattice.
The result of the L-test indicate that the intenisty statistics behave as expected. No twinning is suspected.

NZ test indicates translational pseudosymmetry unlikely.

CHAIN A

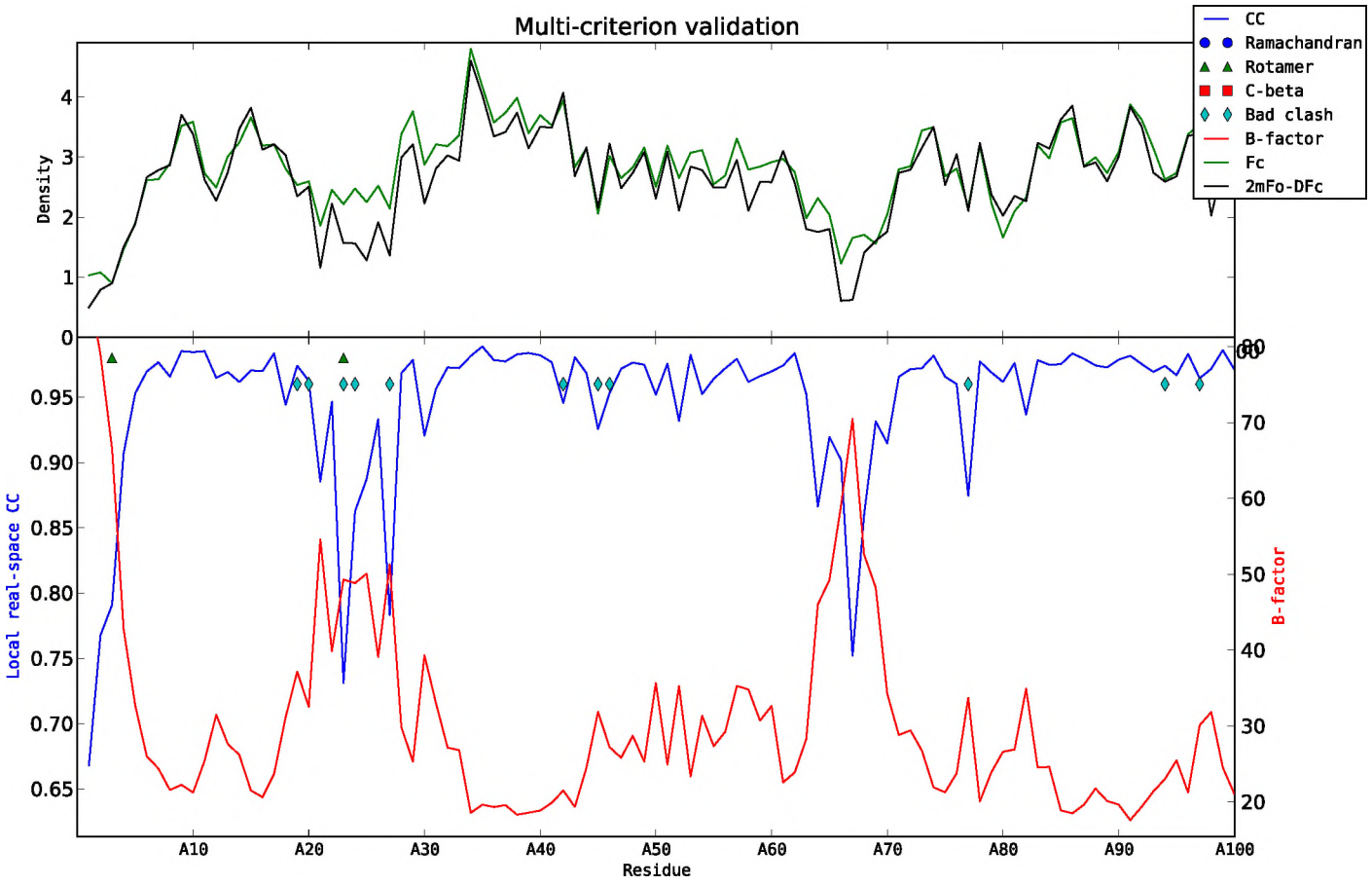
Multi-criterion validation
CC
Ramachandran
Rotamer
C-beta
Bad clash
B-factor
Fc
2mFo-DFc
Density
Local real-space CC
B-factor
Residue
A10
A20
A30
A40
A50
A60
A70
A80
A90
A100

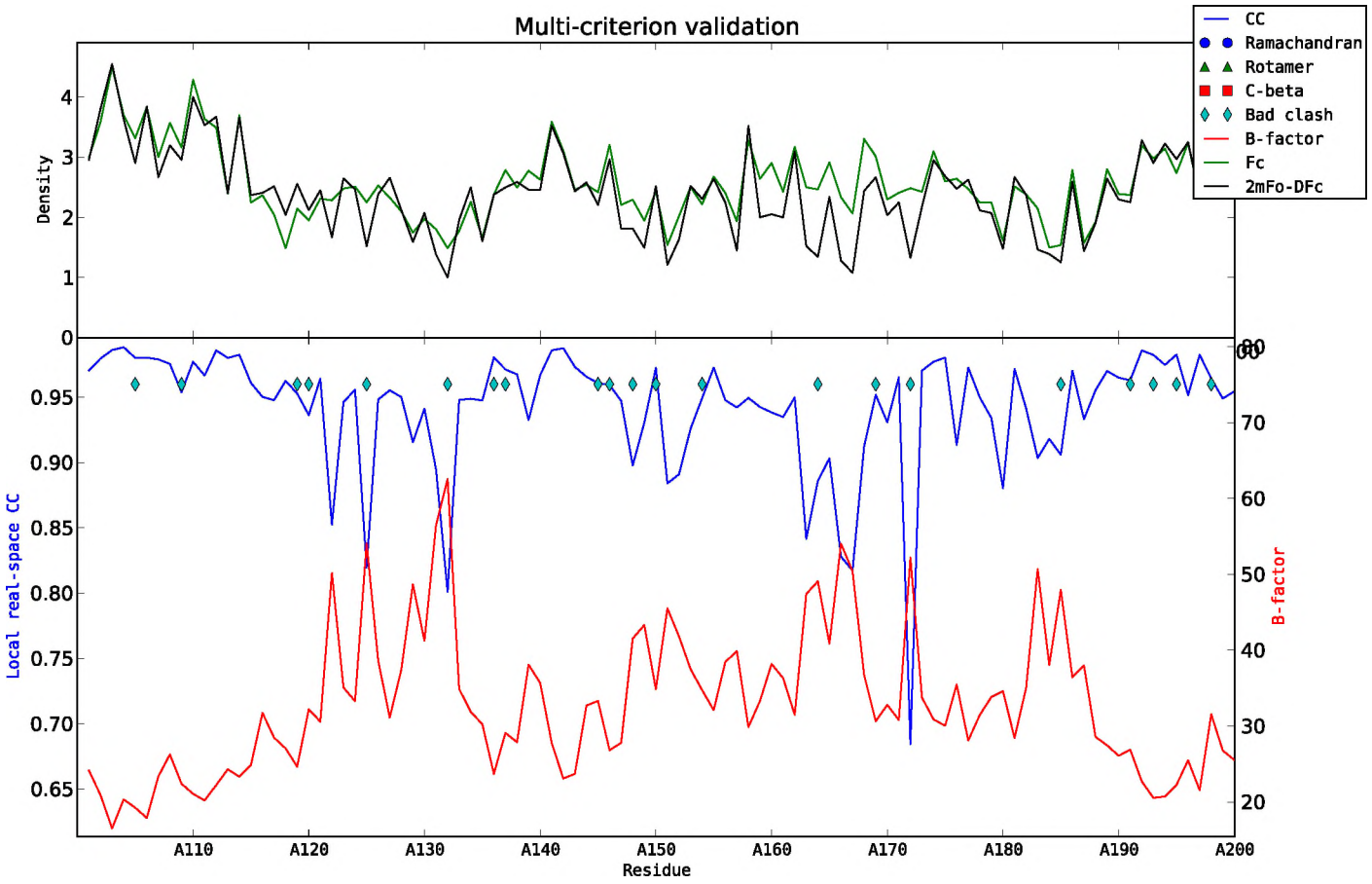
Multi-criterion validation
CC
Ramachandran
Rotamer
C-beta
Bad clash
B-factor
Fc
2mFo-DFc
Density
Local real-space CC
B-factor
Residue
A110
A120
A130
A140
A150
A160
A170
A180
A190
A200

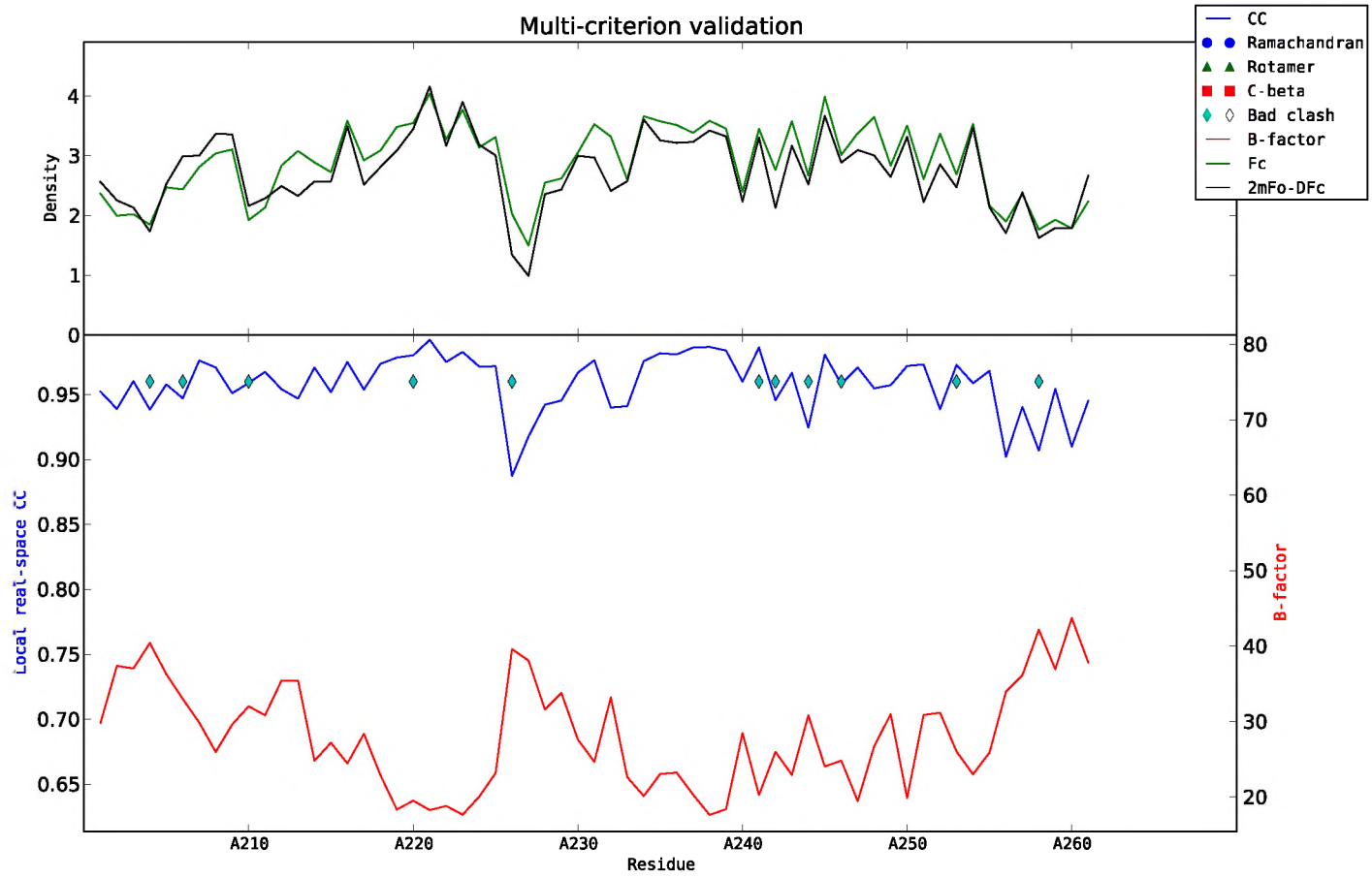
Multi-criterion validation
CC
Ramachandran
Rotamer
C-beta
Bad clash
B-factor
Fc
2mFo-DFc
Density
Local real-space CC
B-factor
A210
A220
A230
A240
A250
A260
Residue

CHAIN B

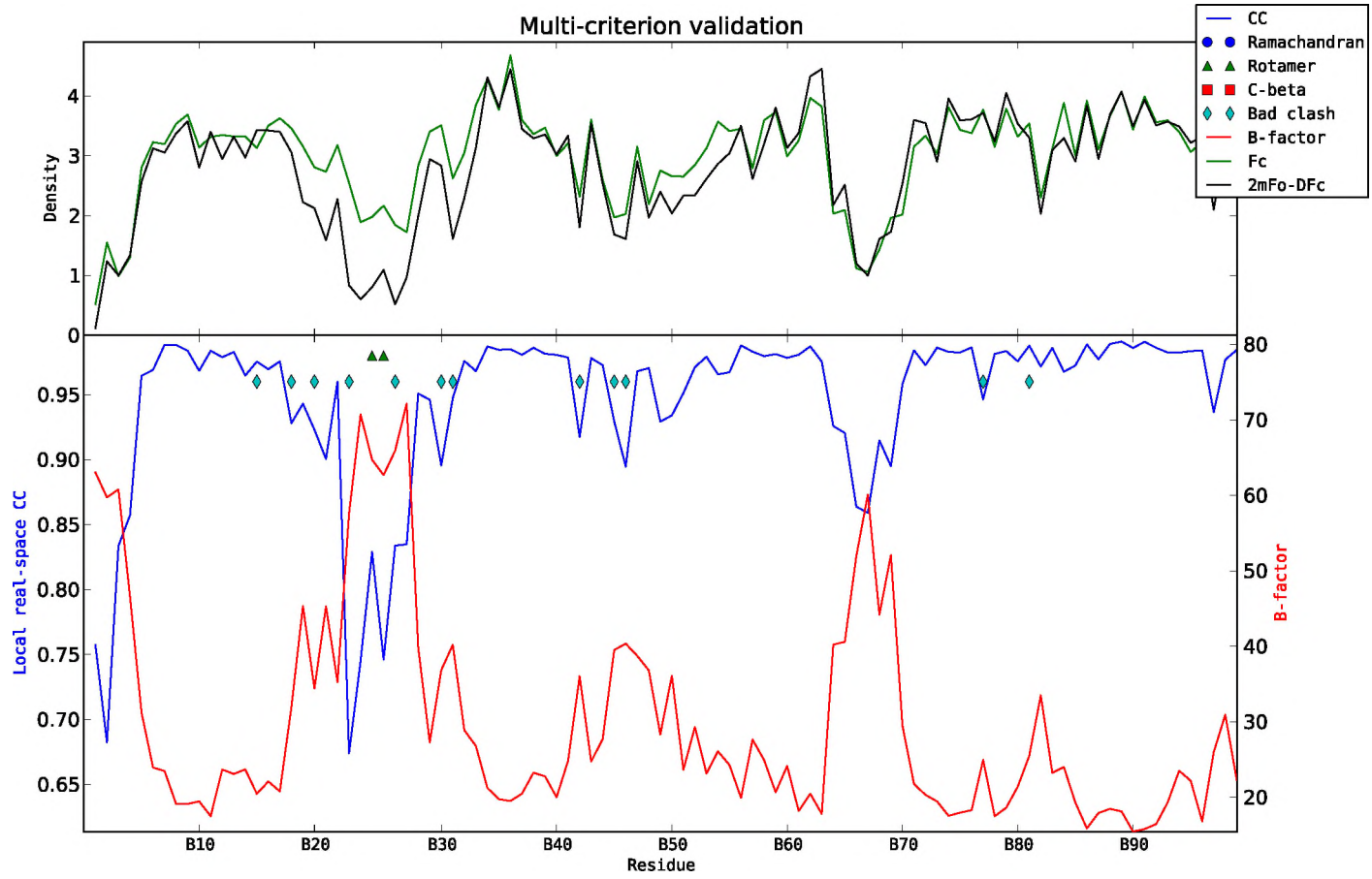
Multi-criterion validation
CC
Ramachandran
Rotamer
C-beta
Bad clash
B-factor
Fc
2mFo-DFc
Density
Local real-space CC
B-factor
B10
B20
B30
B40
B50
B60
B70
B80
B90
Residue

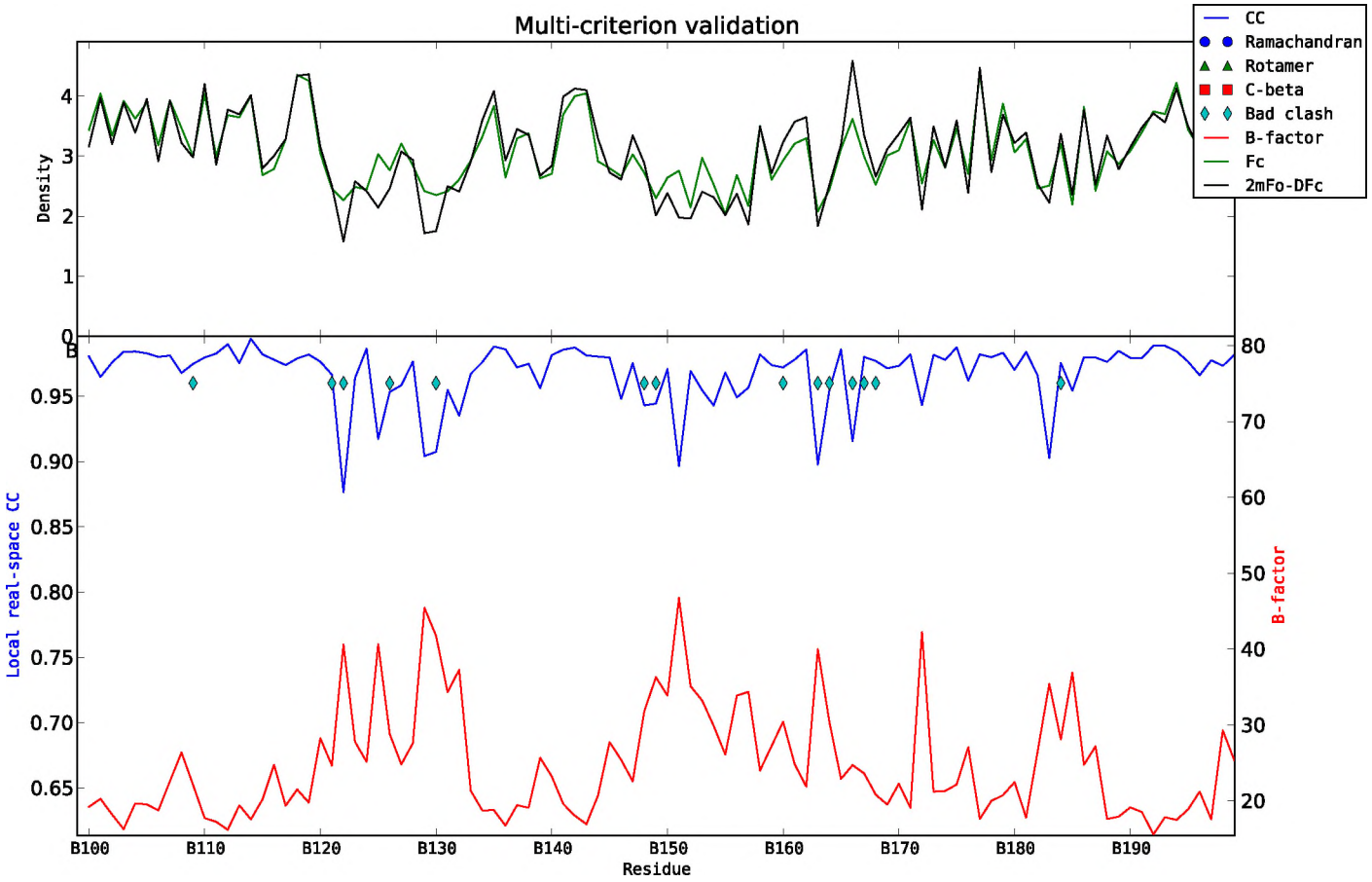
Multi-criterion validation
CC
Ramachandran
Rotamer
C-beta
Bad clash
B-factor
Fc
2mFo-DFc
Density
Local real-space CC
B-factor
B100
B110
B120
B130
B140
B150
B160
B170
B180
B190
Residue

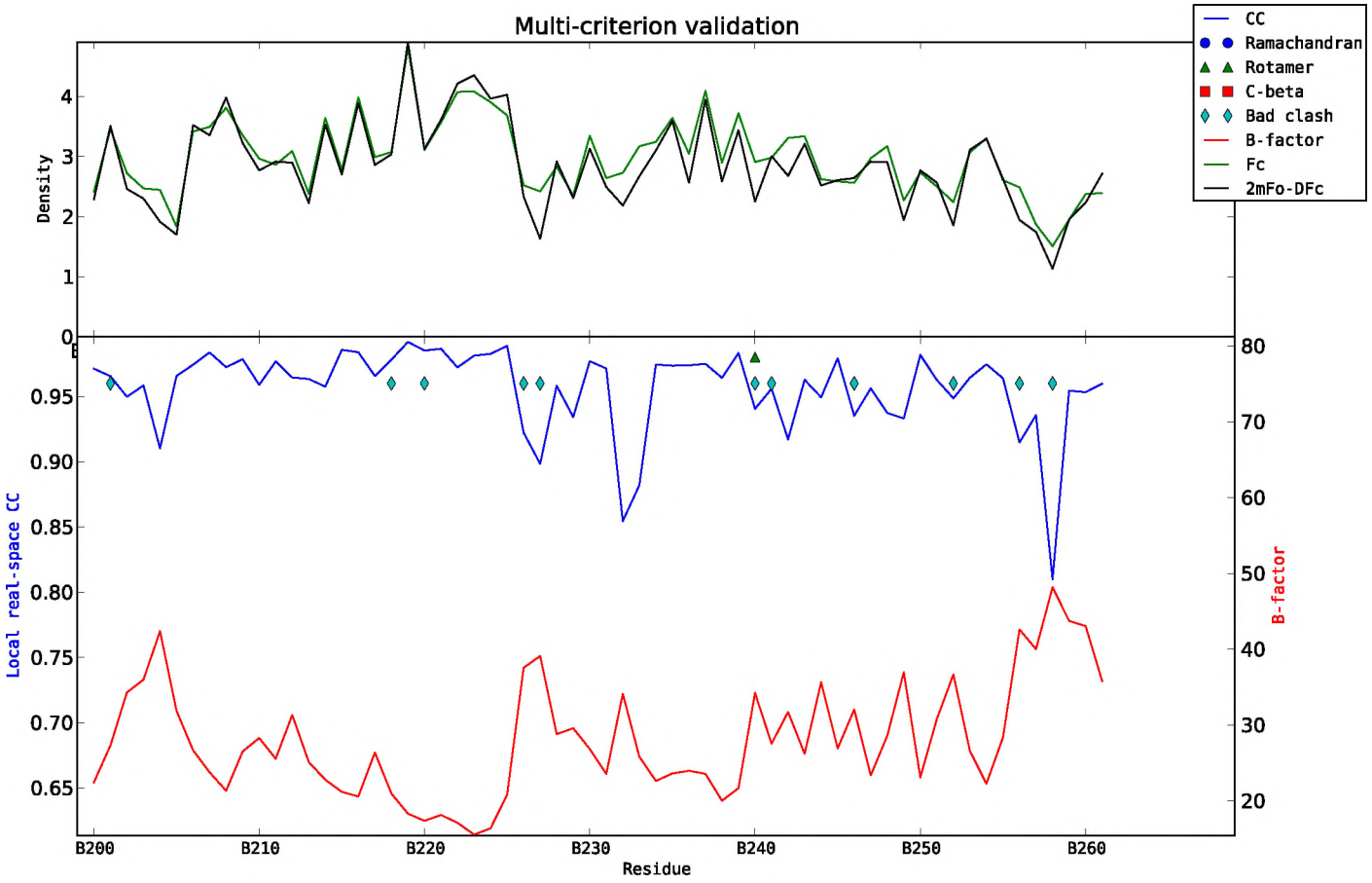
Multi-criterion validation
CC
Ramachandran
Rotamer
C-beta
Bad clash
B-factor
Fc
2mFo-DFc
Density
Local real-space CC
B-factor
B200
B210
B220
B230
B240
B250
B260
Residue

CHAIN C

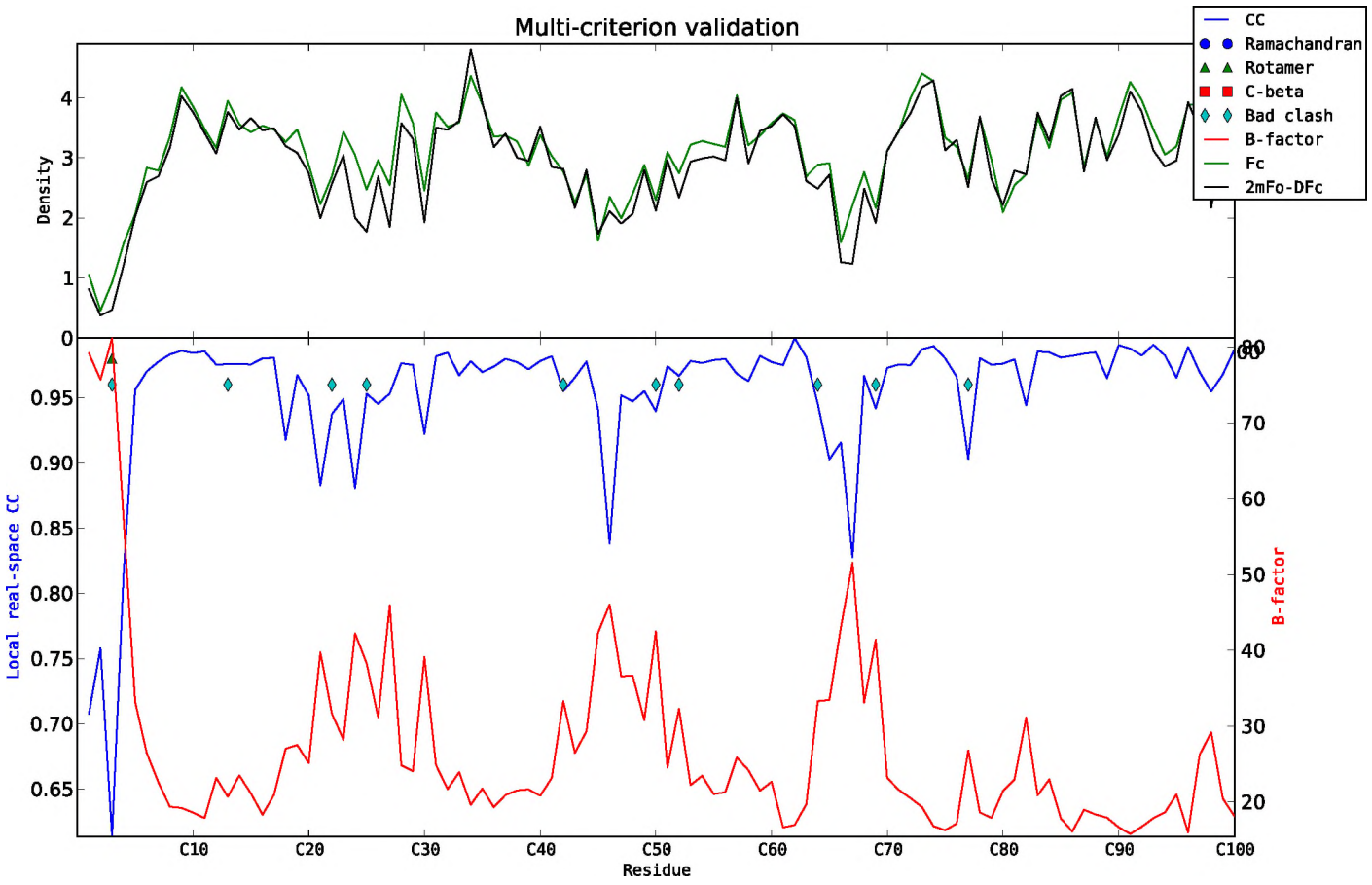
Multi-criterion validation
CC
Ramachandran
Rotamer
C-beta
Bad clash
B-factor
Fc
2mFo-DFc
Density
Local real-space CC
B-factor
Residue
C10
C20
C30
C40
C50
C60
C70
C80
C90
C100

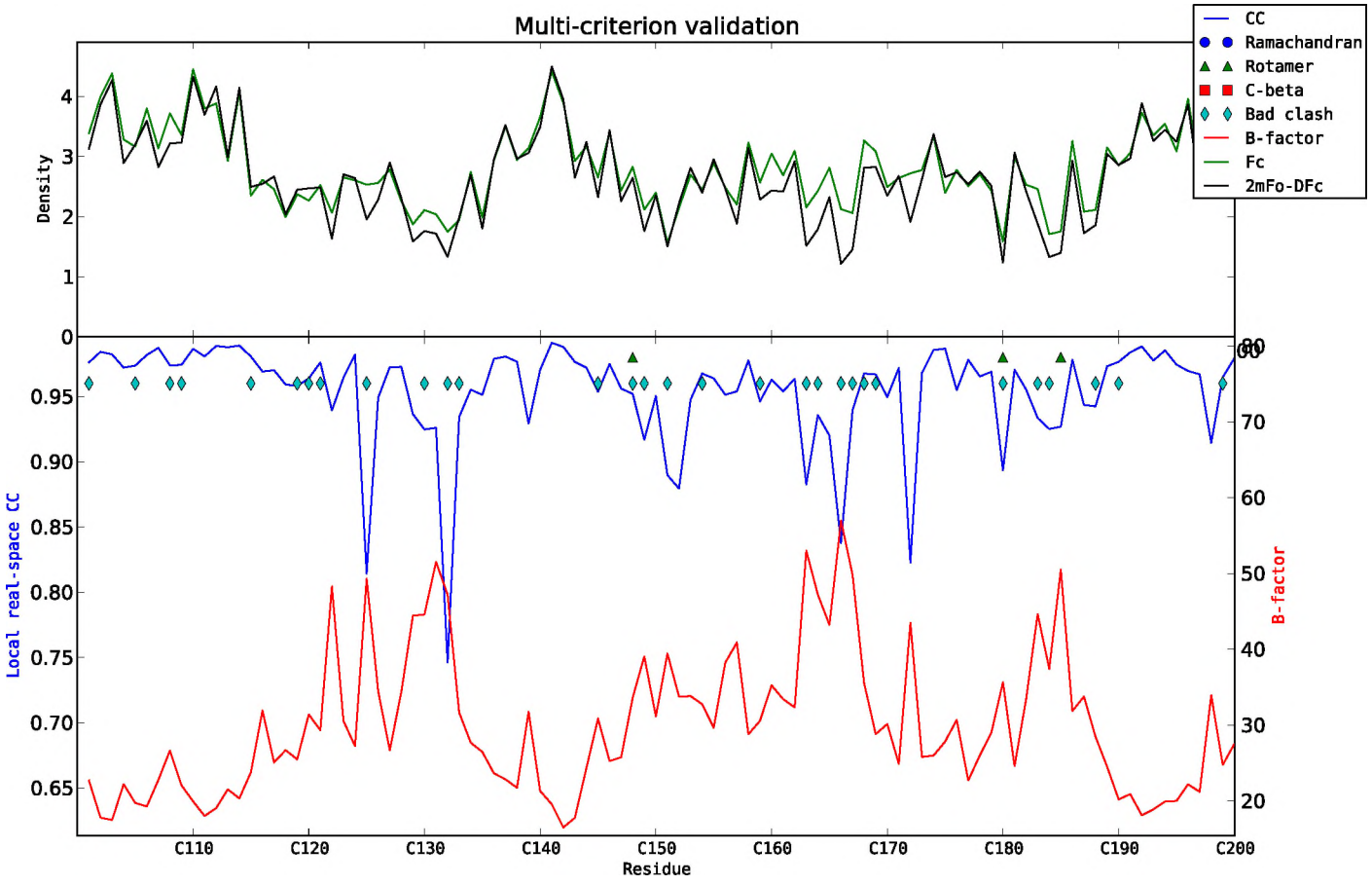
Multi-criterion validation
CC
Ramachandran
Rotamer
C-beta
Bad clash
B-factor
Fc
2mFo-DFc
Density
Local real-space CC
B-factor
Residue
C110
C120
C130
C140
C150
C160
C170
C180
C190
C200

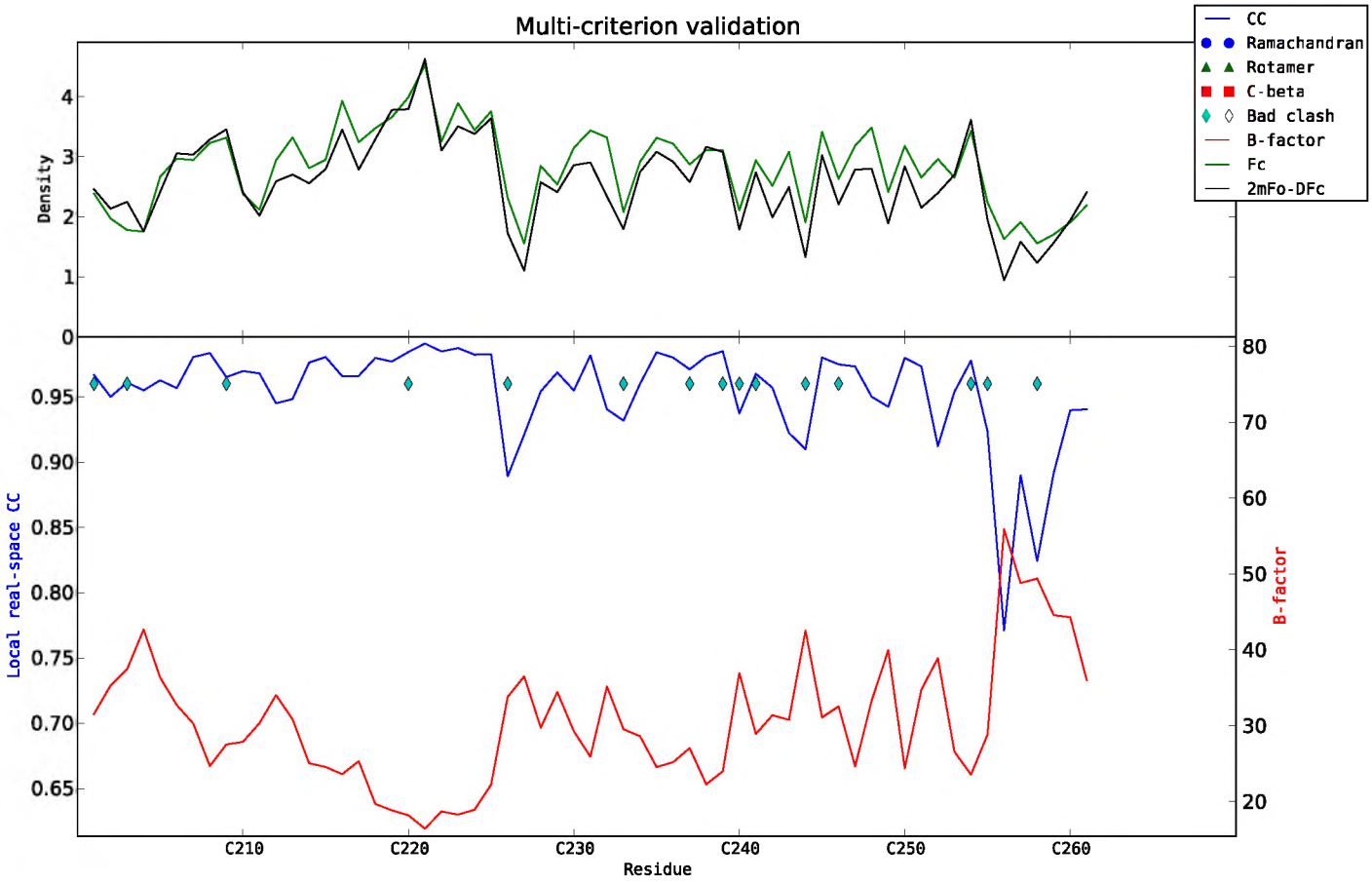
Multi-criterion validation
CC
Ramachandran
Rotamer
C-beta
Bad clash
B-factor
Fc
2mFo-DFc
Density
Local real-space CC
B-factor
Residue
C210
C220
C230
C240
C250
C260

MolProbity Ramachandran analysis

Final_StructureFH_reg.pdb, model 1

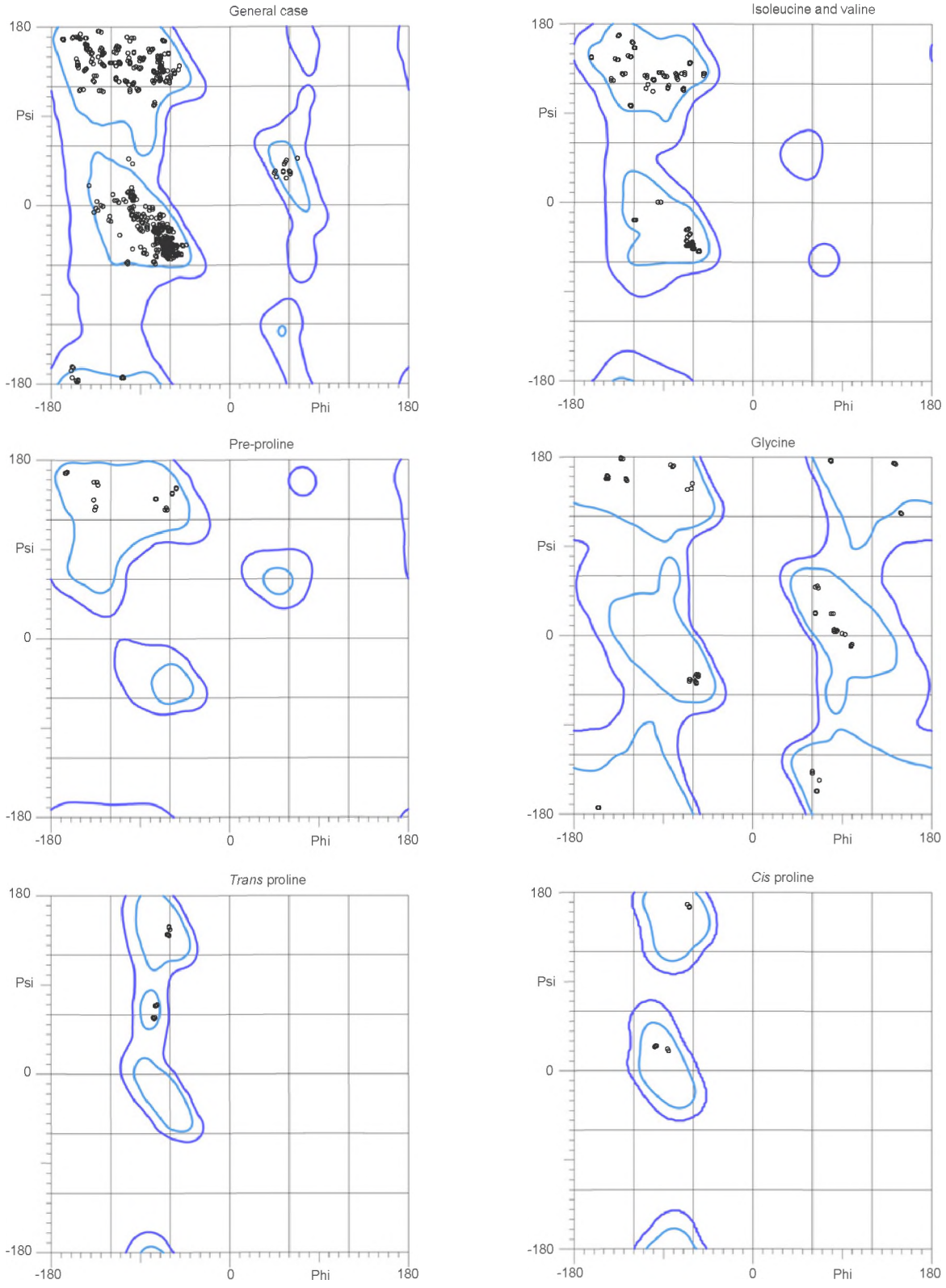

98.1% (765/780) of all residues were in favored (98%) regions.
100.0% (780/780) of all residues were in allowed (>99.8%) regions.

There were no outliers.

MolProbity Score

All-Atom Contacts	Clashscore, all atoms:		11.57	66th percentile
	Clashscore is the number of serious steric overlaps (> 0.4 Å) per 1000 atoms.			
Protein Geometry	Poor rotamers	7	1.07%	Goal: <1%
	Ramachandran outliers	0	0.00%	Goal: <0.05%
	Ramachandran favored	760	98.06%	Goal: >98%
	MolProbity score^		1.60	90th percentile
	Cβ deviations >0.25Å	0	0.00%	Goal: 0
	Bad backbone bonds:	3 / 6219	0.05%	Goal: 0%
	Bad backbone angles:	4 / 8359	0.05%	Goal: <0.1%

In the two column results, the left column gives the raw count, right column gives the percentage.

* 100th percentile is the best among structures of comparable resolution; 0th percentile is the worst. For clashscore the comparative set of structures was selected in 2004, for MolProbity score in 2006.

^ MolProbity score combines the clashscore, rotamer, and Ramachandran evaluations into a single score, normalized to be on the same scale as X-ray resolution.

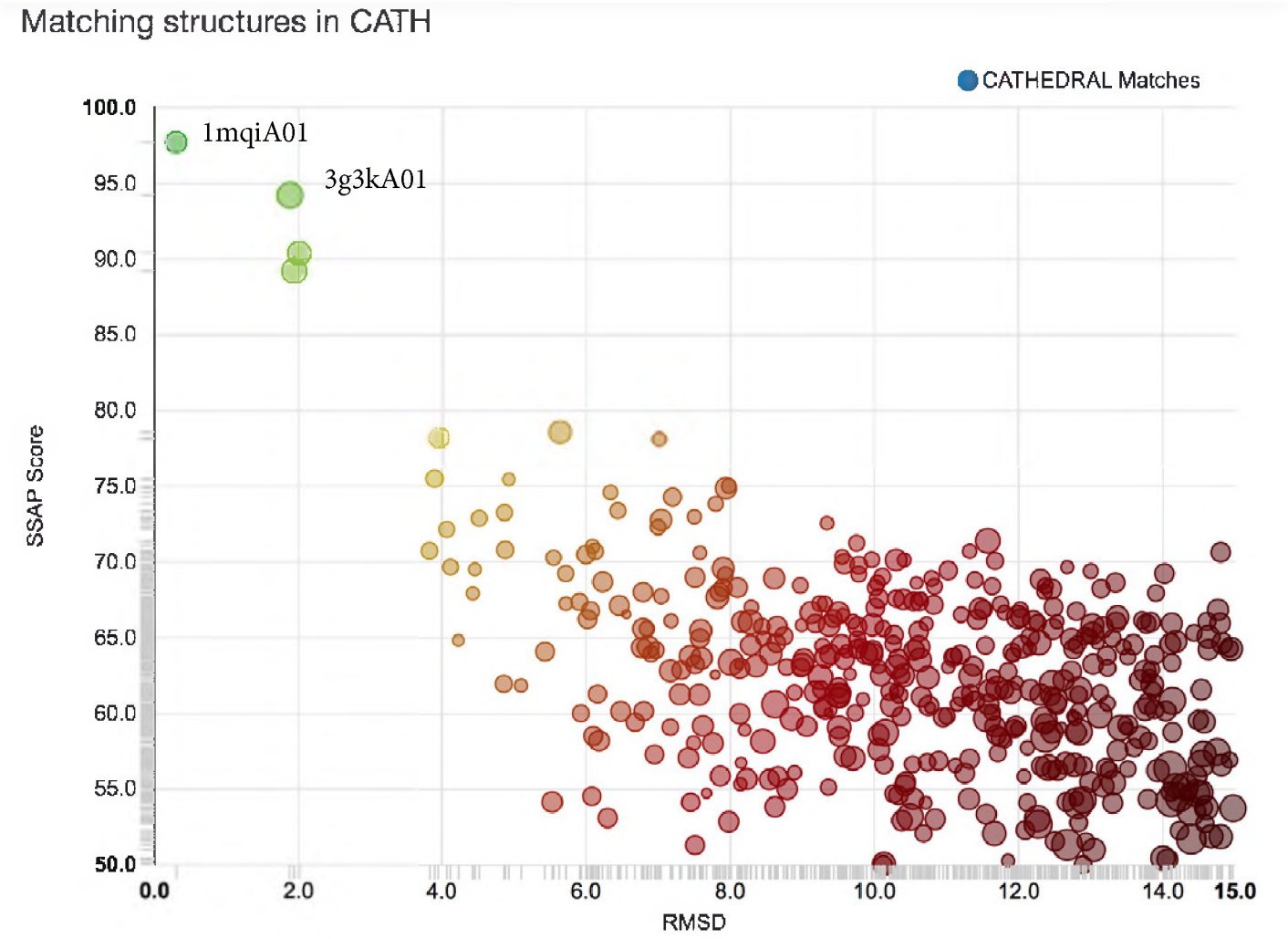

pointandscale.log

The logfile is composed of output from the following programs:

- Pointless
- Aimless
- Ctruncate Finished with: Normal termination

Please consider citing the following papers:

- Aimless
  - P.R.Evans and G.N.Murshudov, 'How good are my data and what is the resolution?' Acta Cryst. D69, 1204-1214 (2013). **PDF**
- Pointless
  - P.R.Evans, 'Scaling and assessment of data quality' Acta Cryst. D62, 72-82 (2006). **PDF** P.R.Evans, 'An introduction to data reduction: space-group determination, scaling and intensity statistics' Acta Cryst. D67, 282-292 (2011) **PDF**

Pointless *Version 1.8.17 Run at 21:09:01 on 18/ 4/2014*

Result:

Best Solution: point group P 2 2 2

Reindex operator:	[h,k,l]
Laue group probability:	0.988
Systematic absence probability:	0.986
Total probability:	0.974
Space group confidence:	0.000
Laue group confidence	0.985

Unit cell: 47.19 113.4 163.1 90 90 90

66.22 to 2.38 - Resolution range used for Laue group search

66.22 to 1.84 - Resolution range in file, used for systematic absence check

Number of batches in file: 400

The data do not appear to be twinned, from the L-test

The following tables were found in the logfile:

L-test for twinning, twin fraction 0.011

Axial reflections, axis a (lattice frame) rotation axis order 2

Axial reflections, axis c (lattice frame) screw axis 2(1)

L-test for twinning, twin fraction 0.011

[Show logfile summary] [Show full logfile] [Documentation]

Aimless *Version 0.2.17* *Run at 21:09:07 on 18/ 4/2014*

Result:

Summary data for Project: New Crystal: New Dataset: New

	Overall	InnerShell	OuterShell
Low resolution limit	66.22	66.22	1.88
High resolution limit	1.84	9.02	1.84
Rmerge (within I+/I-)	0.077	0.037	0.602
Rmerge (all I+ and I-)	0.084	0.041	0.638
Rmeas (within I+/I-)	0.099	0.046	0.794
Rmeas (all I+ & I-)	0.098	0.047	0.762
Rpim (within I+/I-)	0.061	0.027	0.510
Rpim (all I+ & I-)	0.048	0.023	0.405
Rmerge in top intensity bin	0.039	-	-
Total number of observations	202780	1833	11066
Total number unique	59545	512	3815
Mean((I)/sd(I))	8.7	20.2	2.0
Mn(I) half-set correlation CC(1/2)	0.997	0.998	0.599
Completeness	78.1	67.7	81.7
Multiplicity	3.4	3.6	2.9
Anomalous completeness	60.2	61.7	59.6
Anomalous multiplicity	1.6	1.9	1.3
DelAnom correlation between half-sets	-0.080	0.056	-0.044
Mid-Slope of Anom Normal Probability	0.936	-	-

Estimates of resolution limits: overall
from half-dataset correlation CC(1/2) > 0.50: limit = 1.84A == maximum resolution
from Mn(I/sd) > 2.00: limit = 1.86A

Estimates of resolution limits in reciprocal lattice directions:
Along h axis
from half-dataset correlation CC(1/2) > 0.50: limit = 1.84A == maximum resolution
from Mn(I/sd) > 2.00: limit = 1.84A == maximum resolution
Along l axis
from half-dataset correlation CC(1/2) > 0.50: limit = 1.84A == maximum resolution
from Mn(I/sd) > 2.00: limit = 1.84A == maximum resolution

Anisotropic deltaB (i.e. range of principal components), A^2: 4.83

Average unit cell: 47.19 113.4 163.1 90 90 90
Space group: P 2 2 2
Average mosaicity: 0.34

Minimum and maximum SD correction factors: Fulls 0.00 0.00 Partials 0.26 36.94
Anomalous flag switched ON in input but the anomalous signal is weak

DISSECTION AND RECORDING SCHEMES

Posterior to anterior incision along the midline was followed by lateral cut along sternite 3. The skin was pulled back to reveal nerve 3. Recordings were amplified by 10K before recordings.

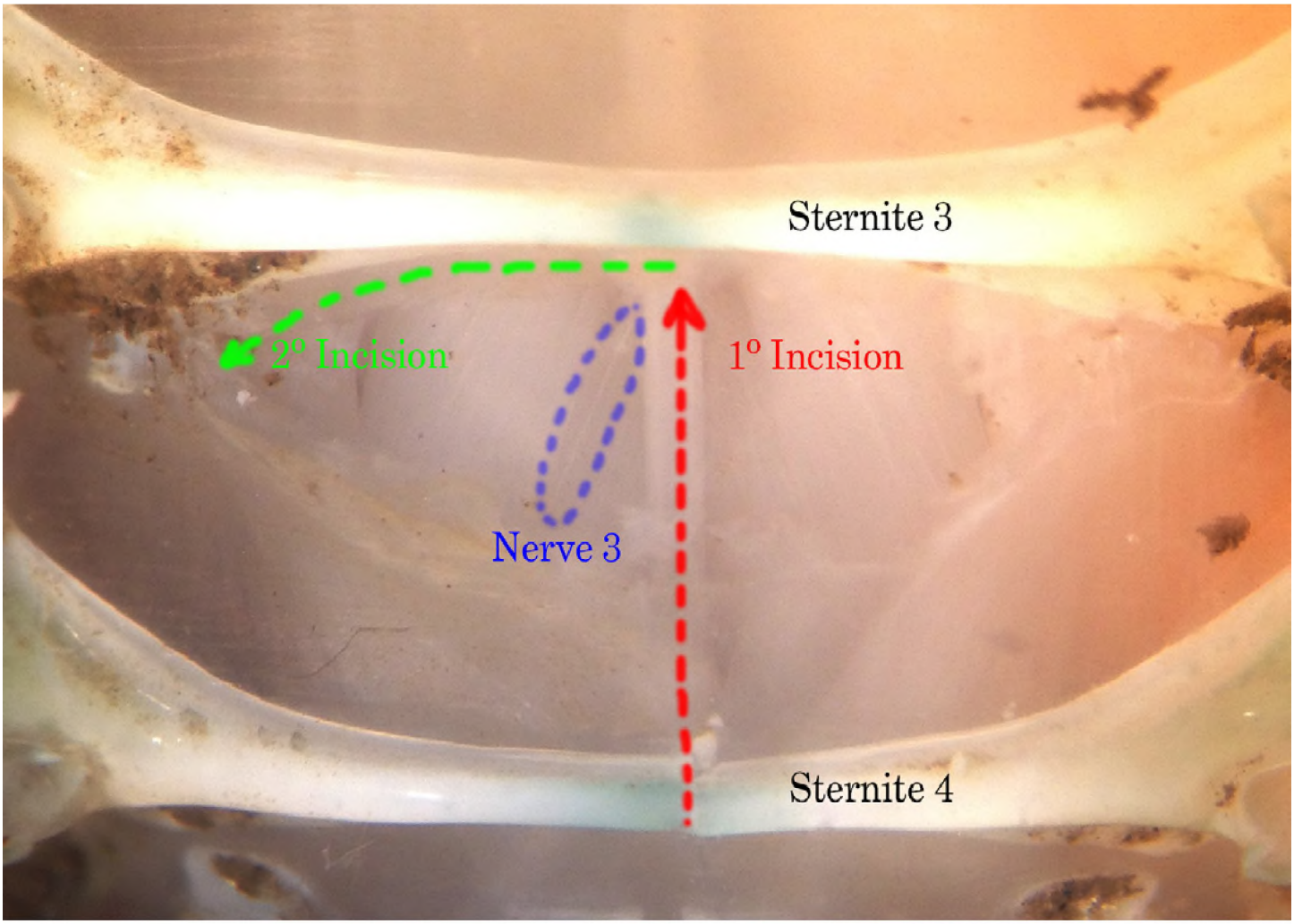

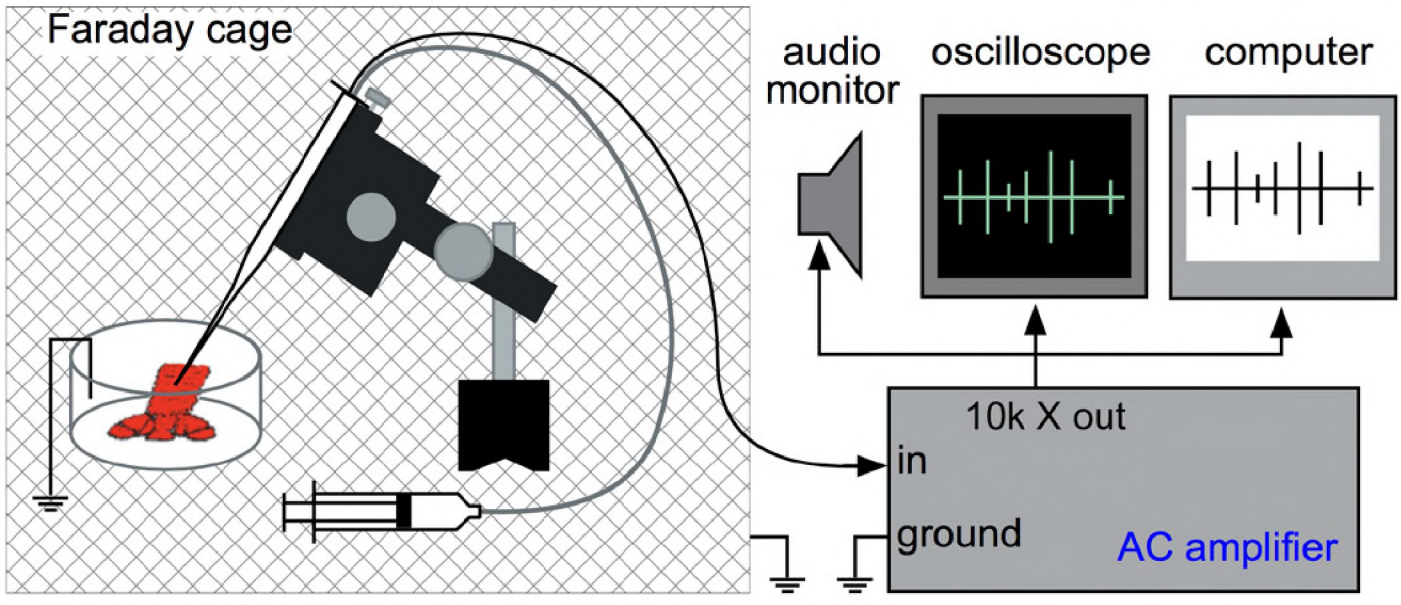

MSG BASAL

MSG 10mM

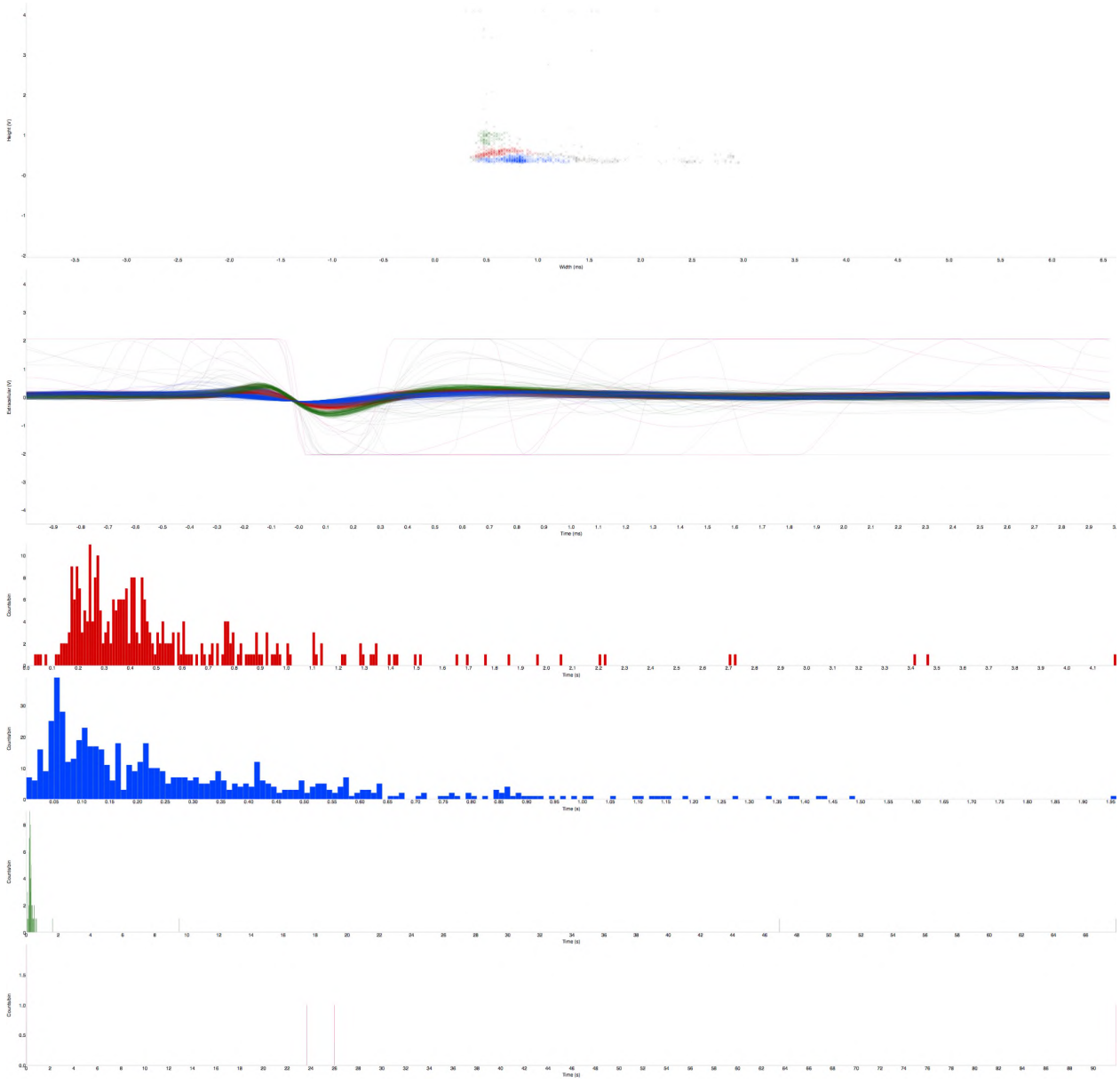

MSG SALINE WASH1

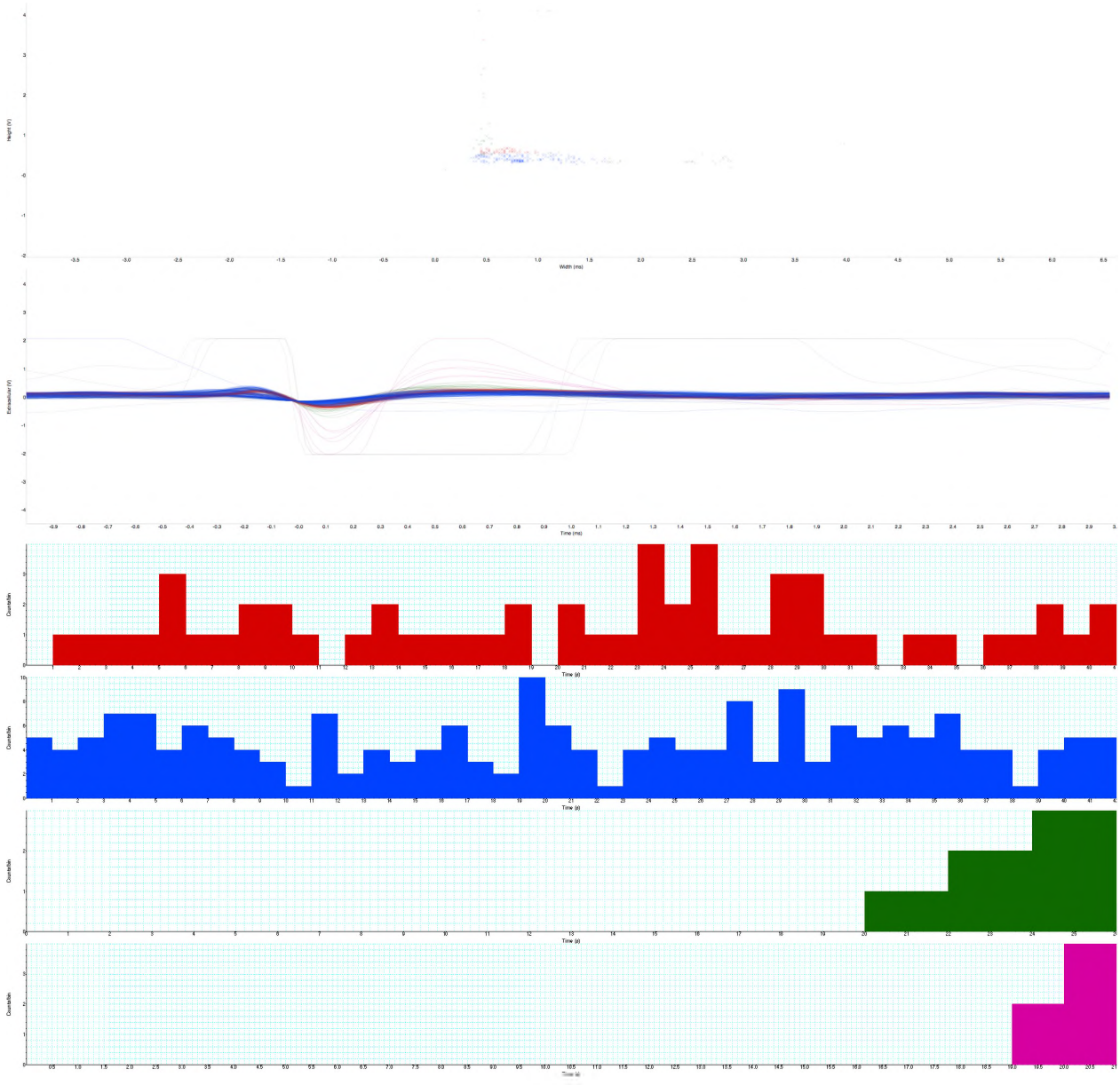

MSG 20mM

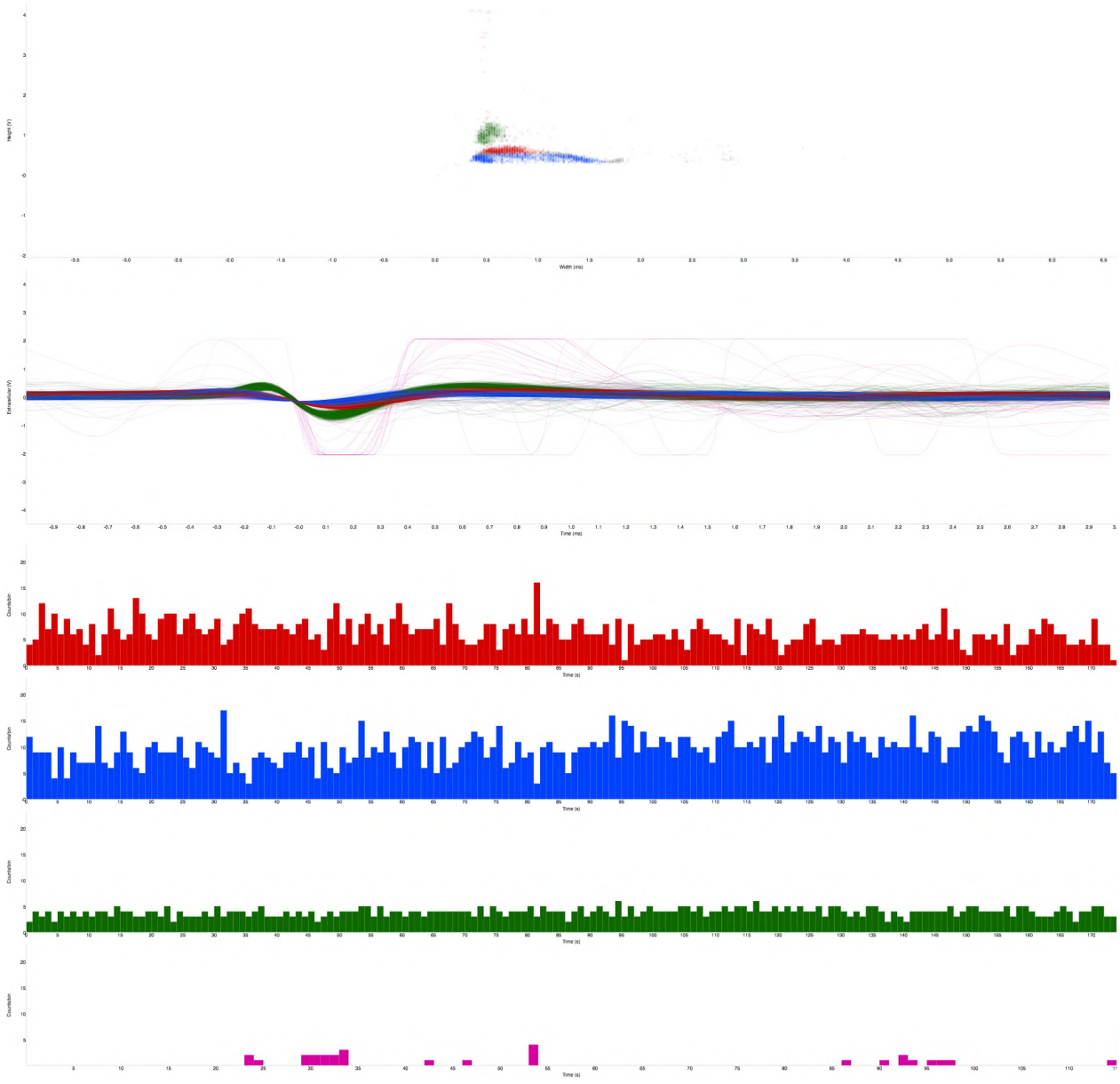

MSG SALINE2

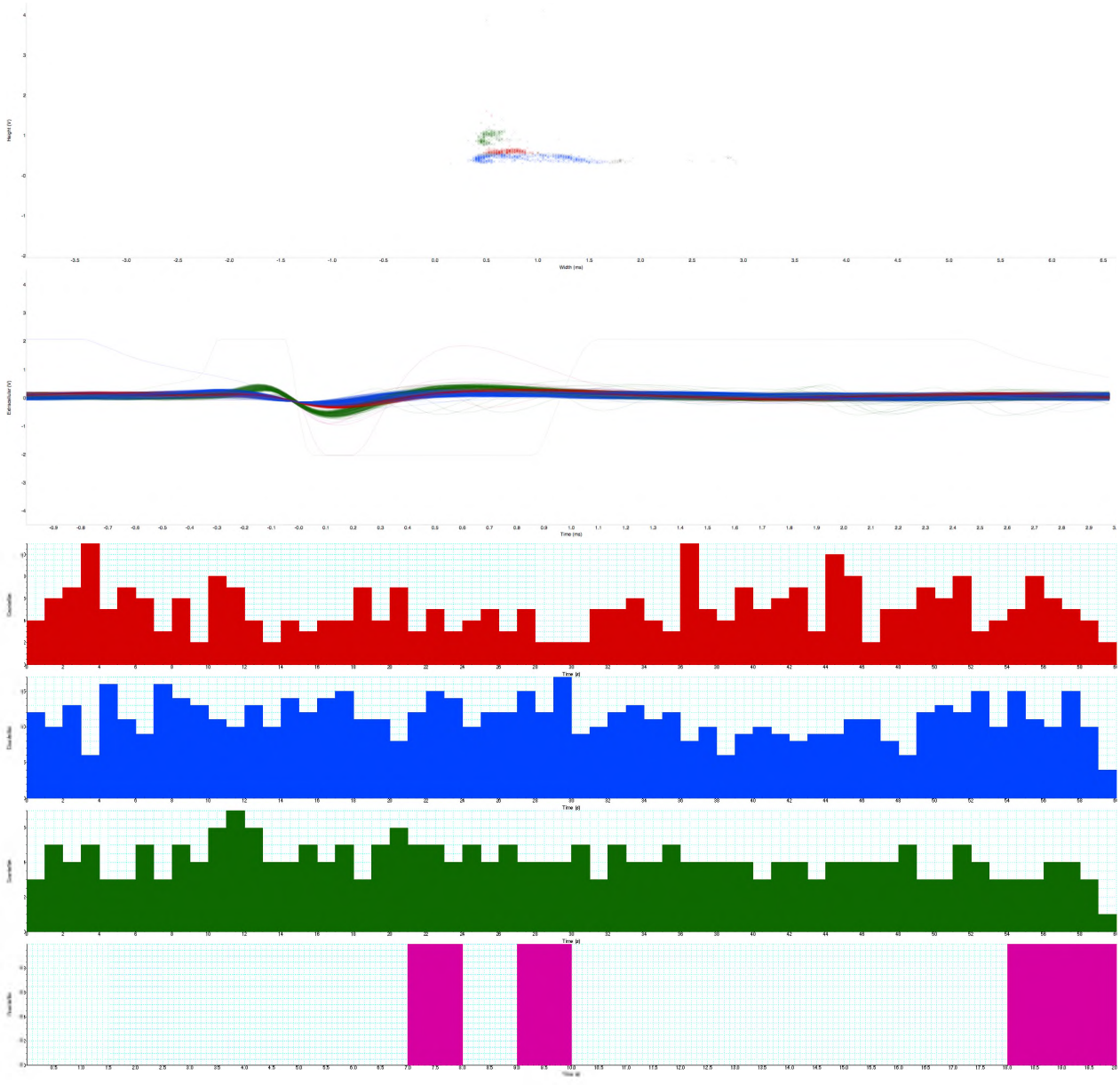

MSG 42mM

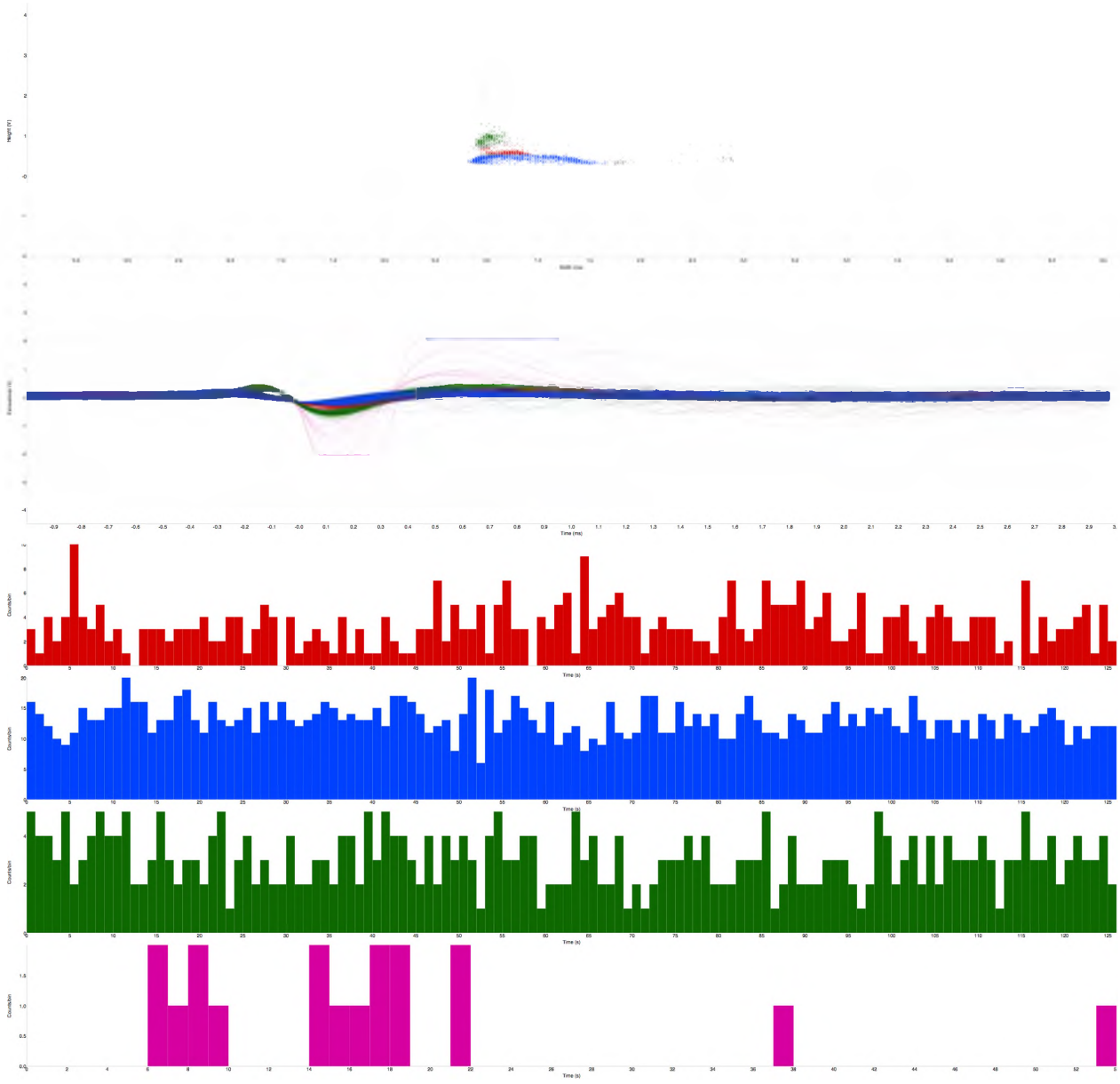

MGS Saline 3

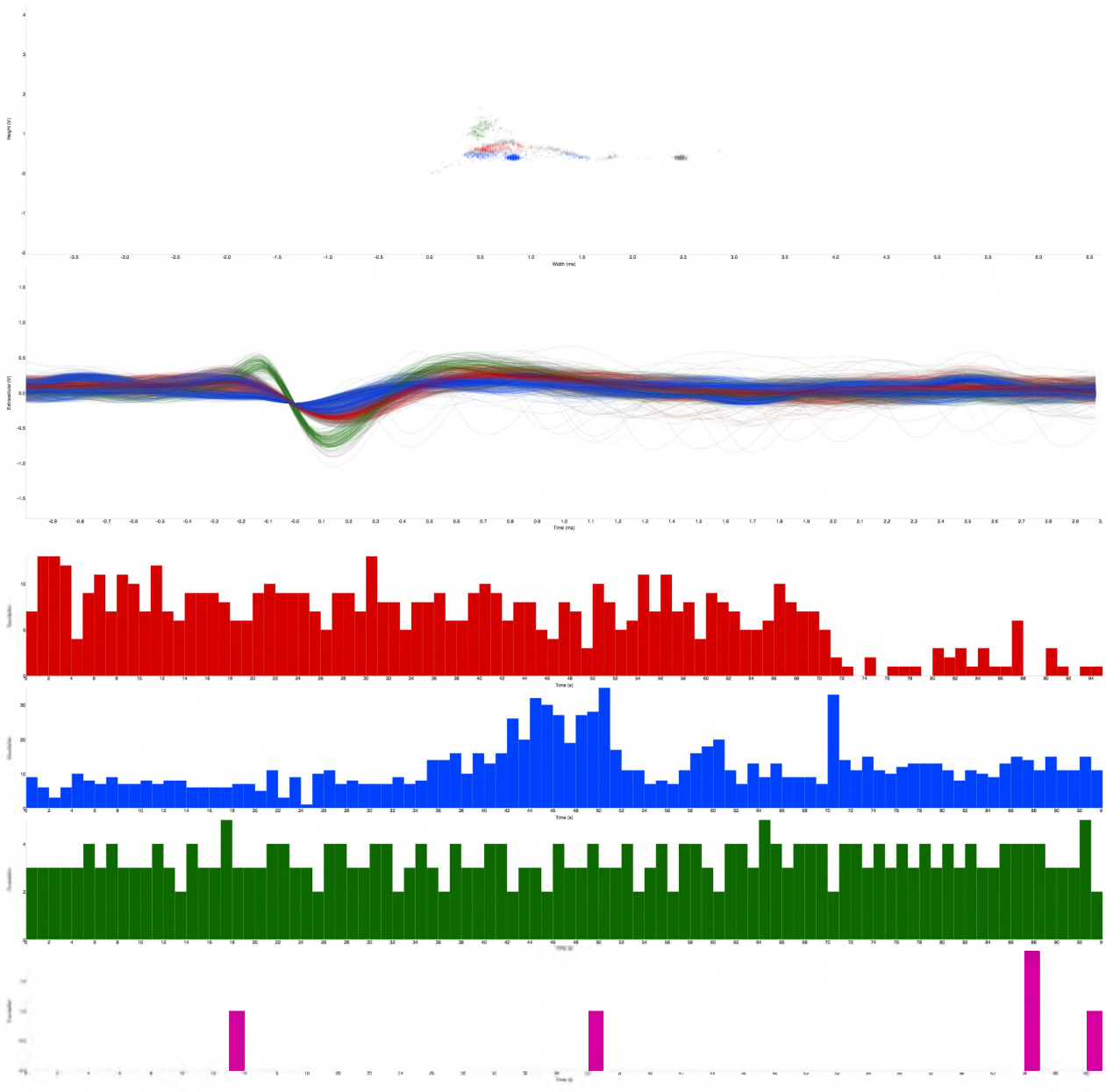

MSG 84mM

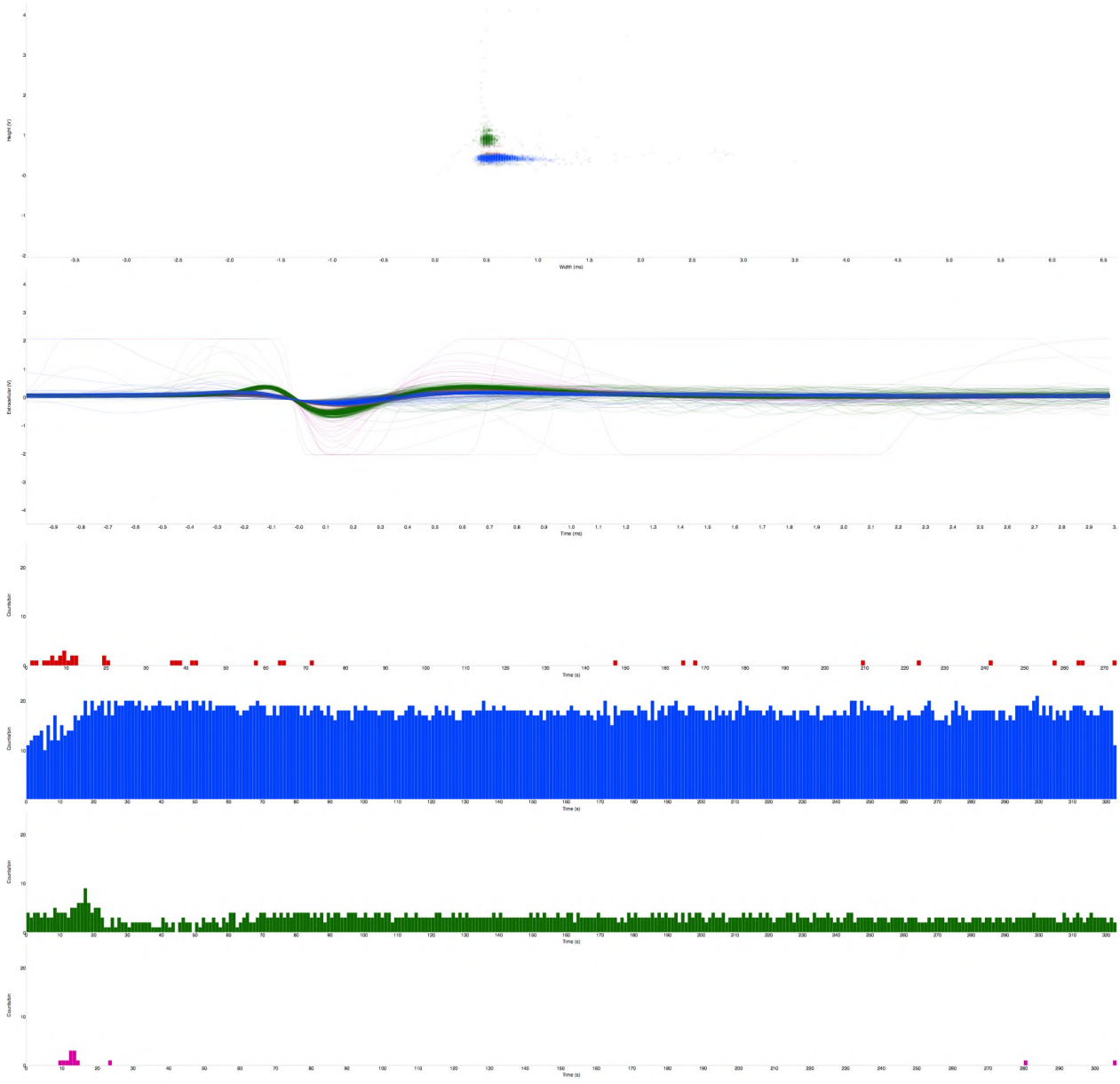

MSG Saline4

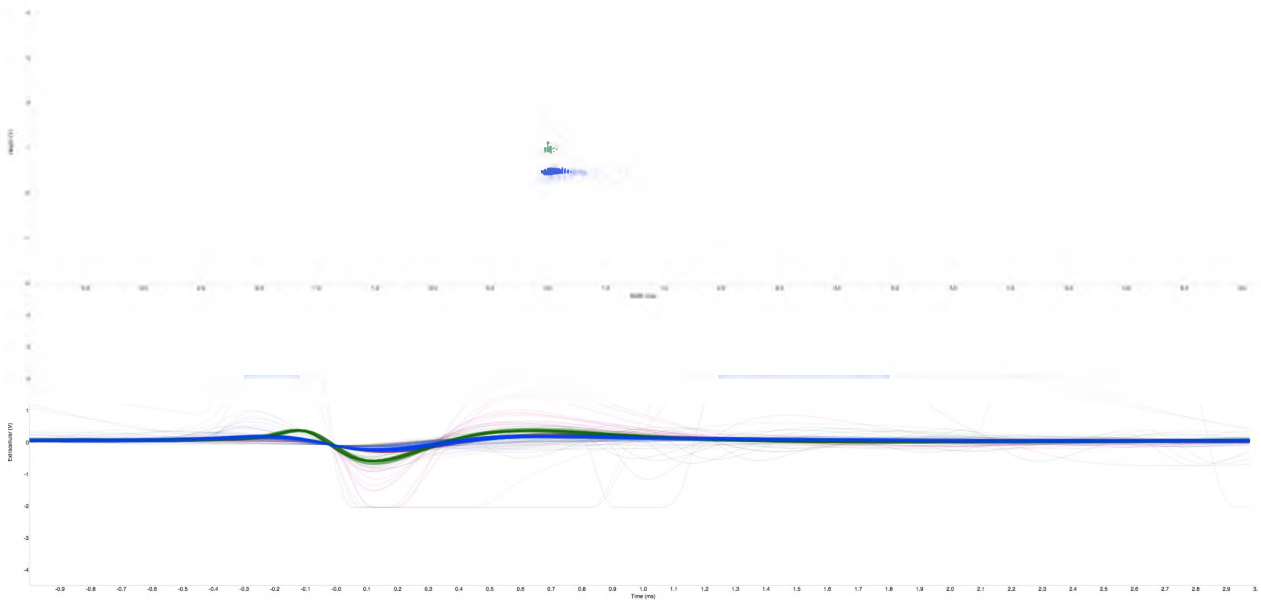

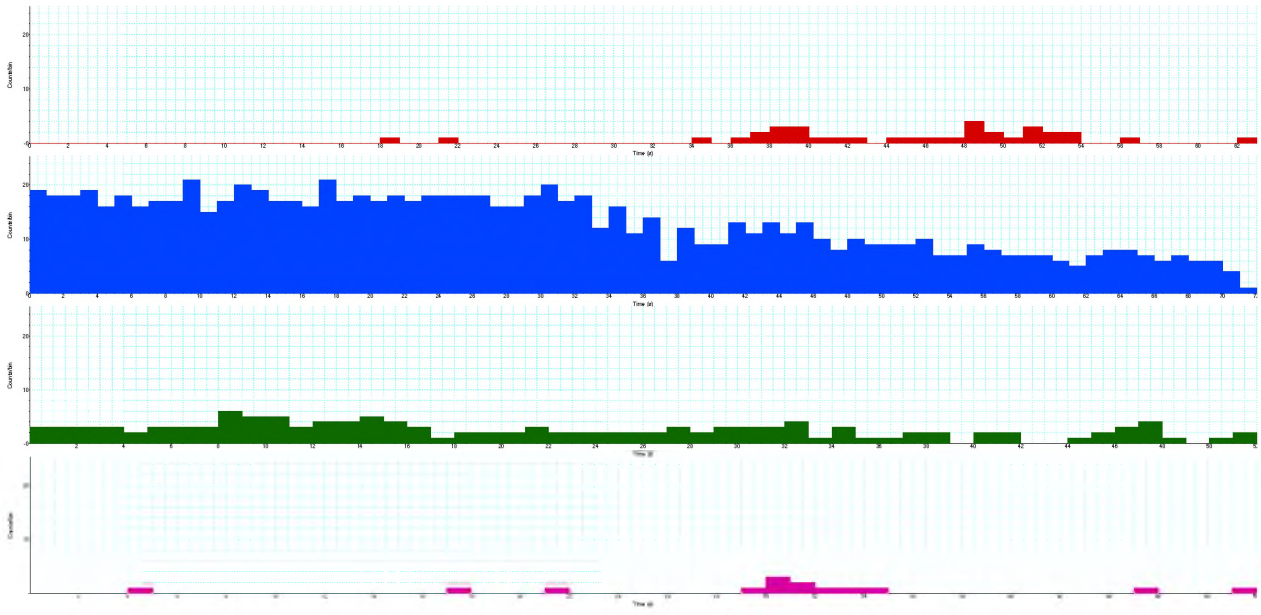

MSG 100mM

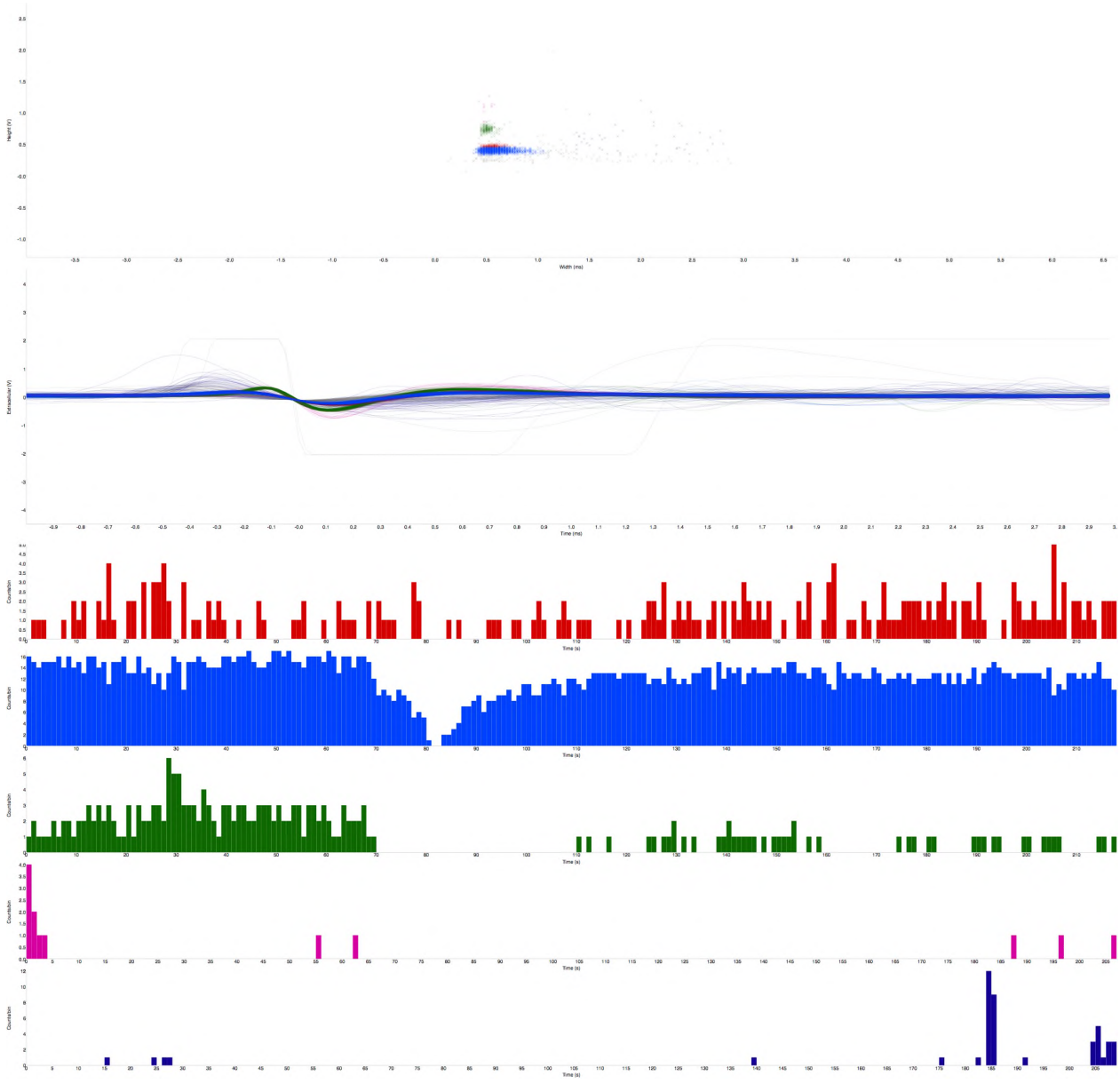

MSG 130mM

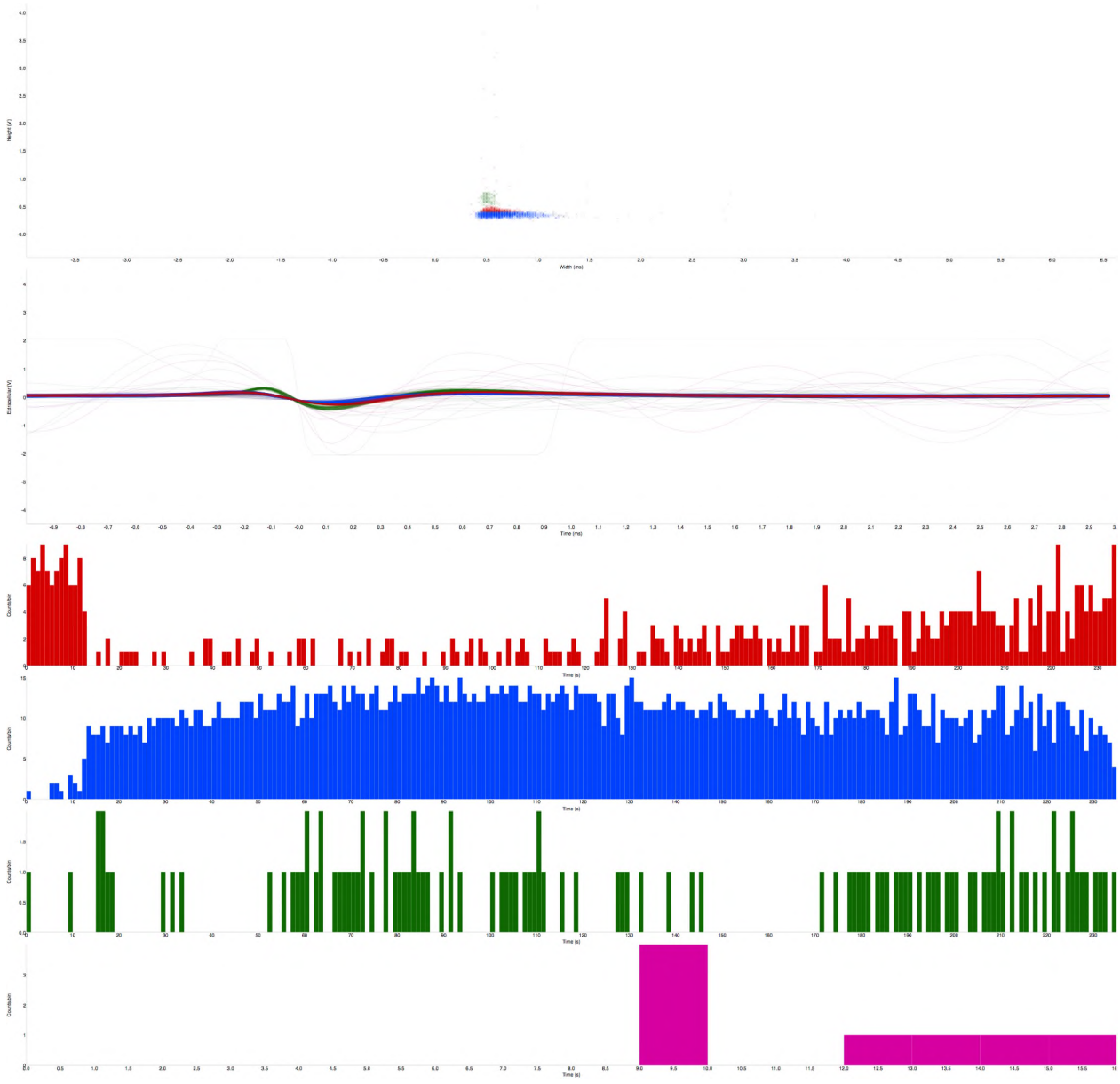

MSG Saline 7

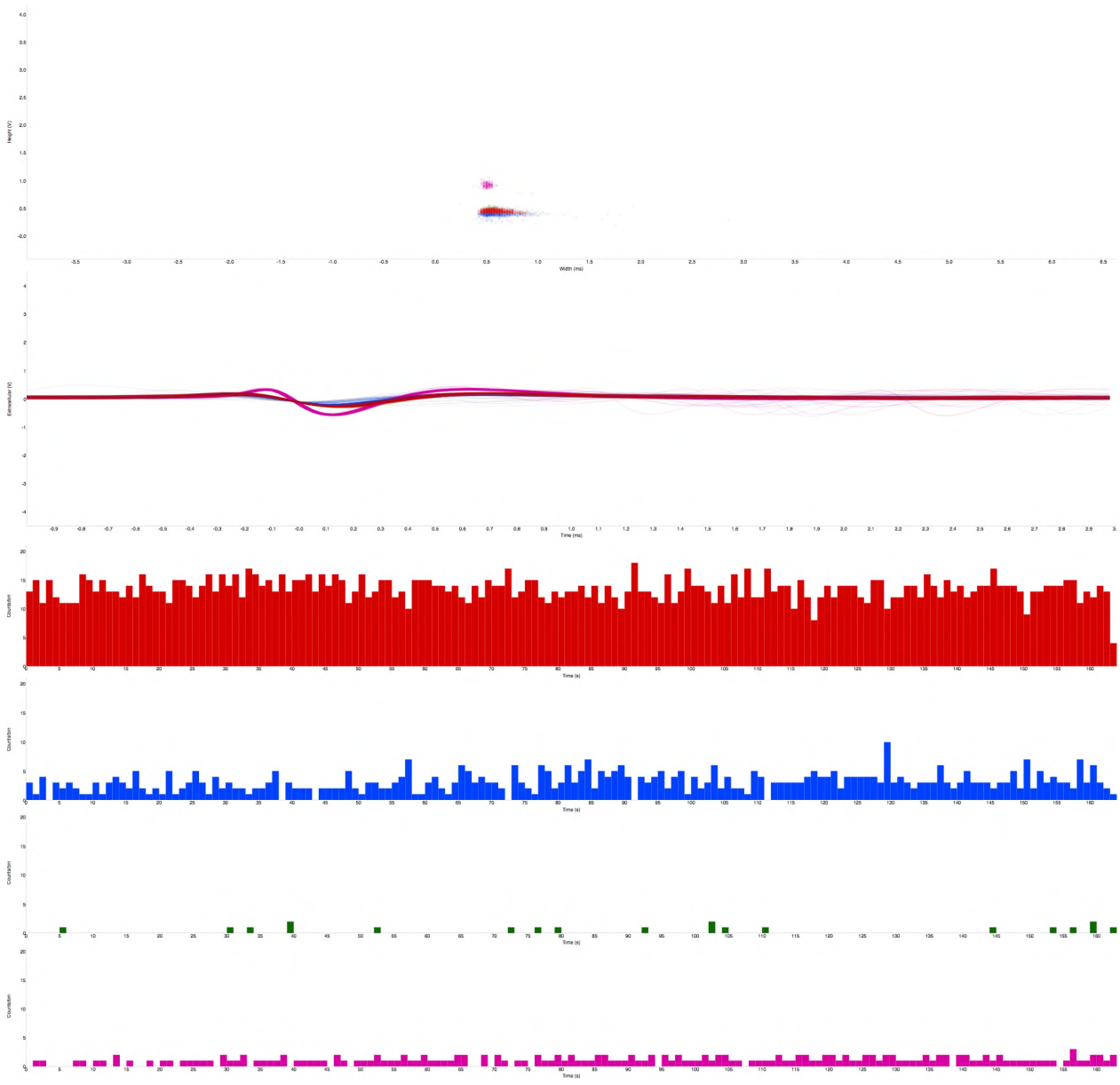

MSG 171mM

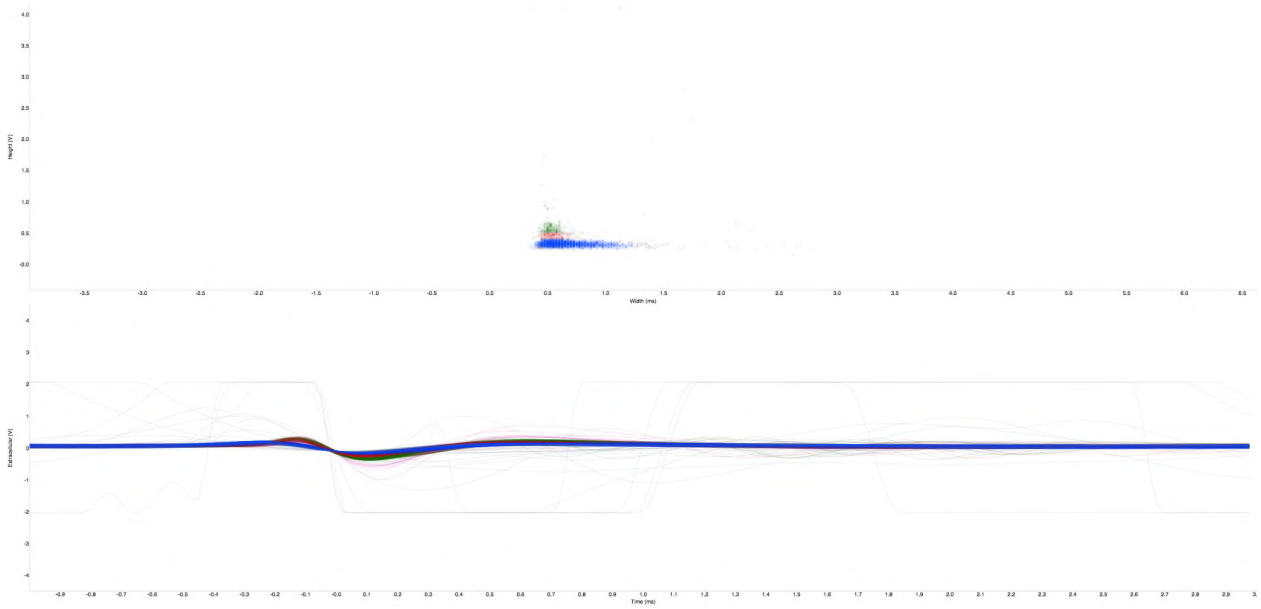

REL_1A Baseline

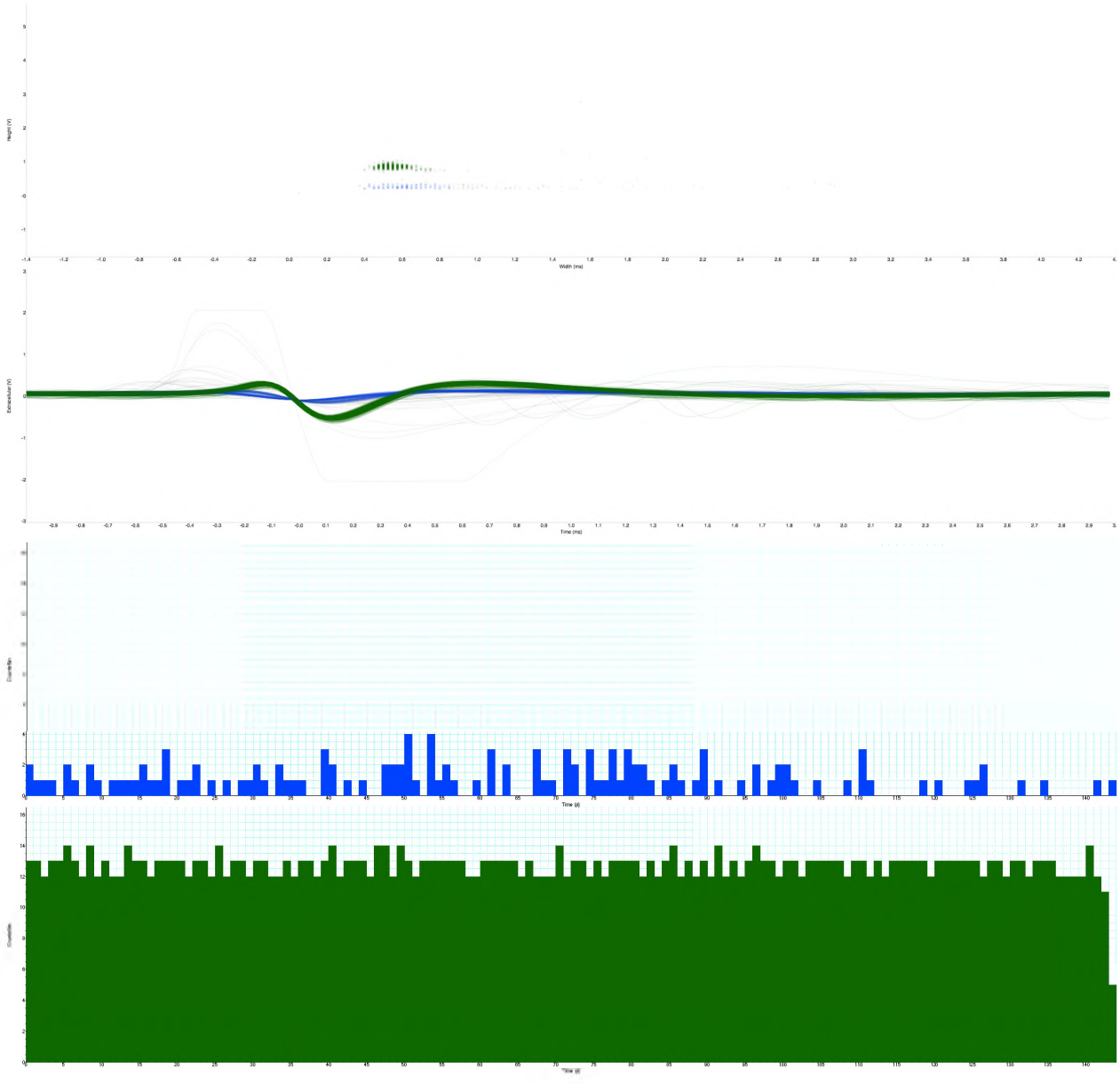

REL_1A 5mM

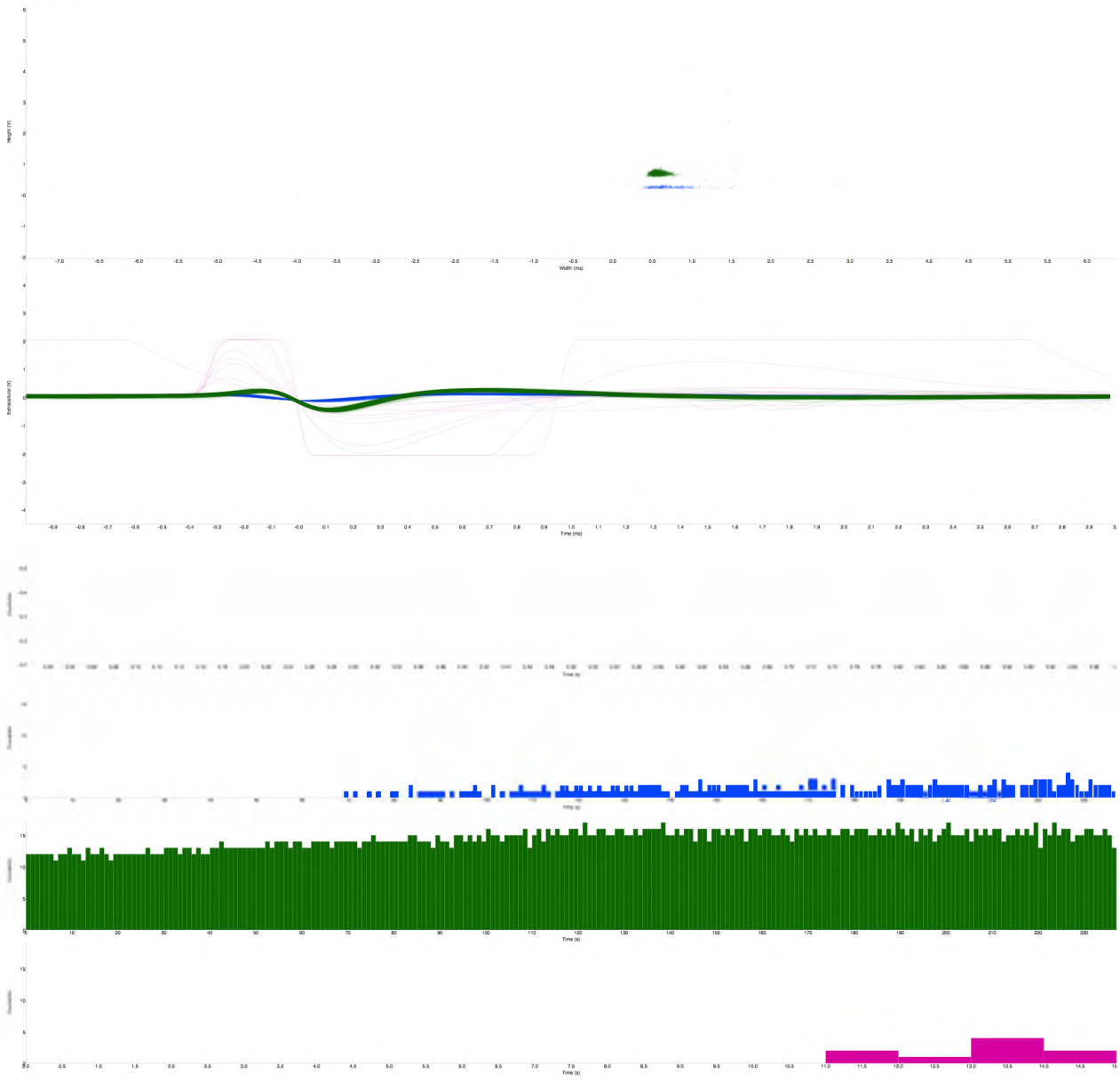

REL_1A Saline Wash 1

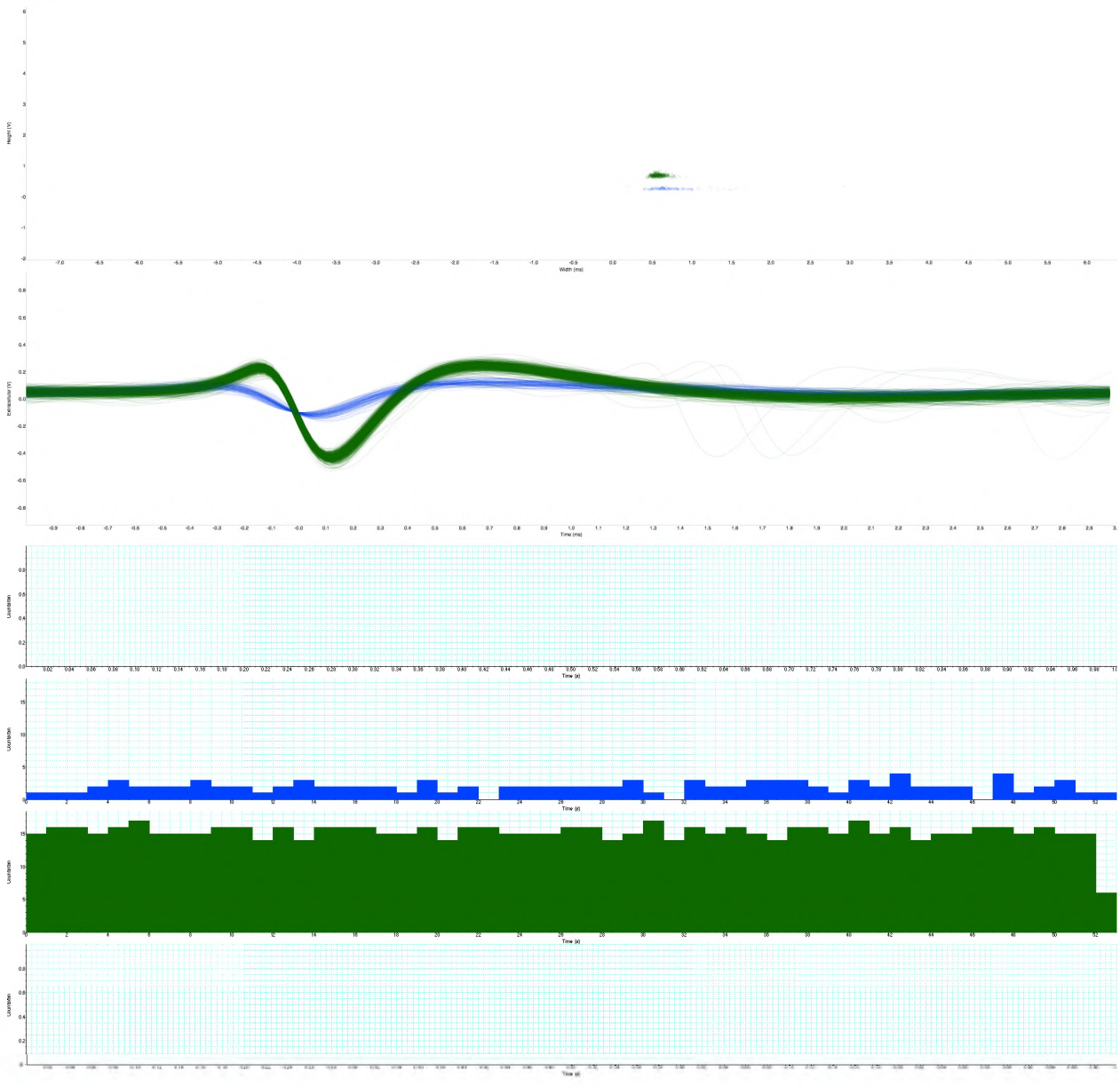

REL_1A 10mM

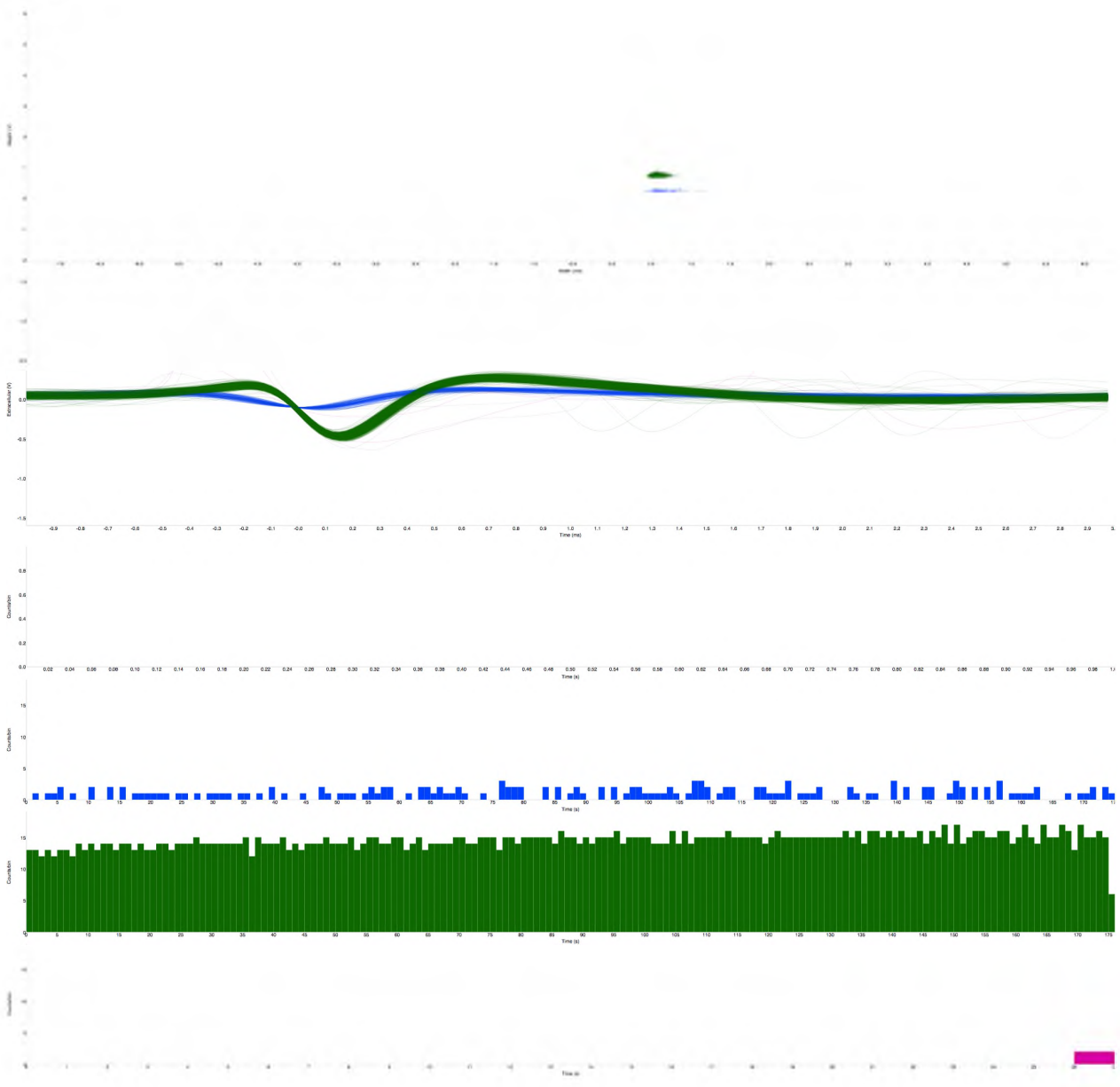

REL_1A 20mM

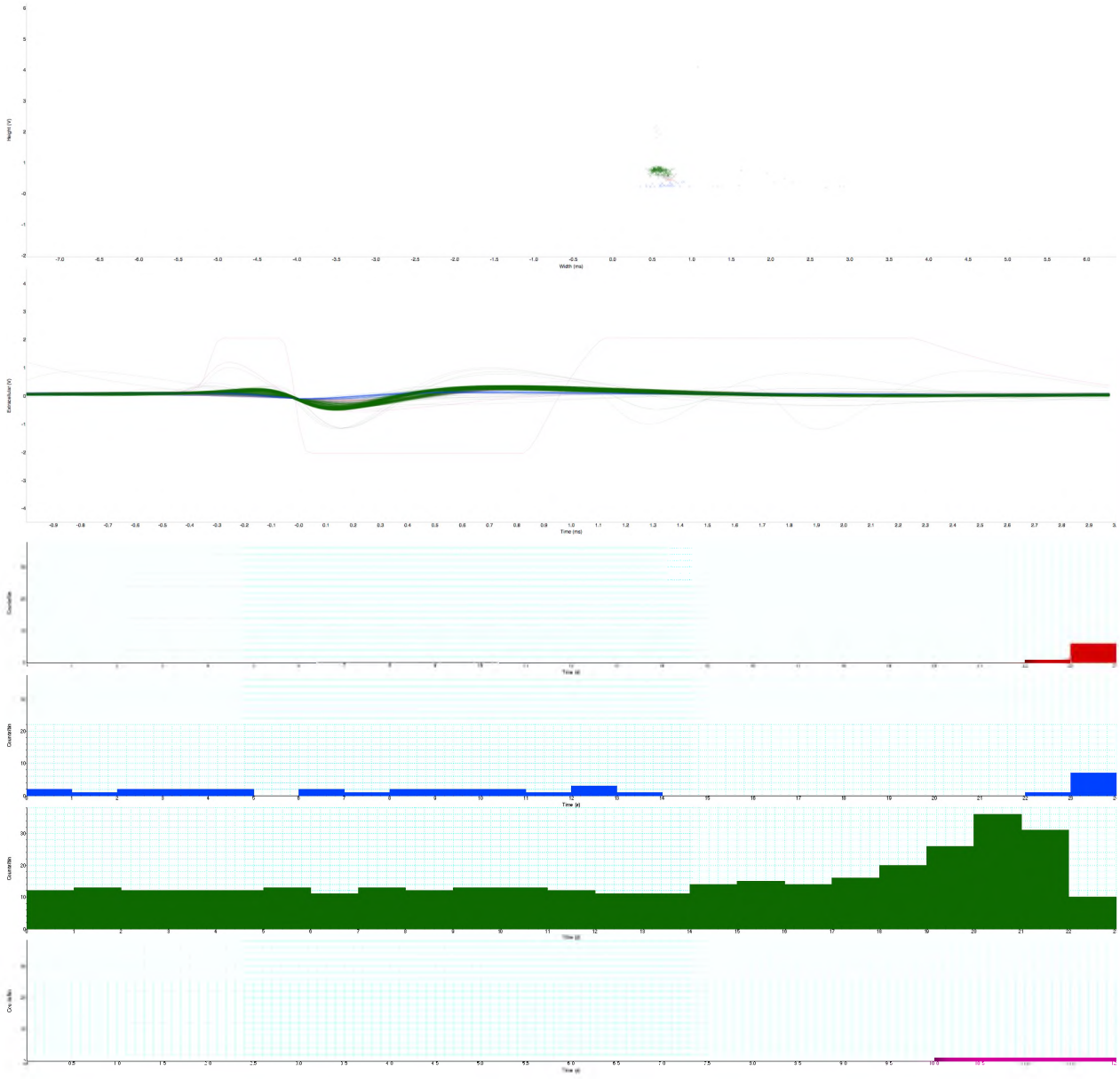

REL_1A 20mM Spike TRACE

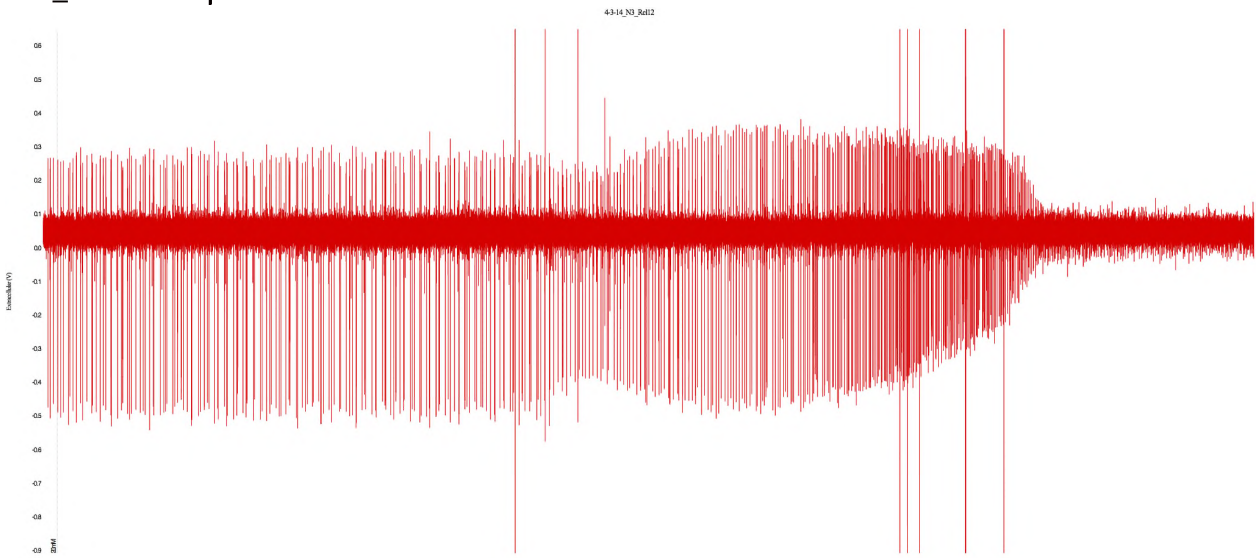

REL_1B Basal Spike Disc View

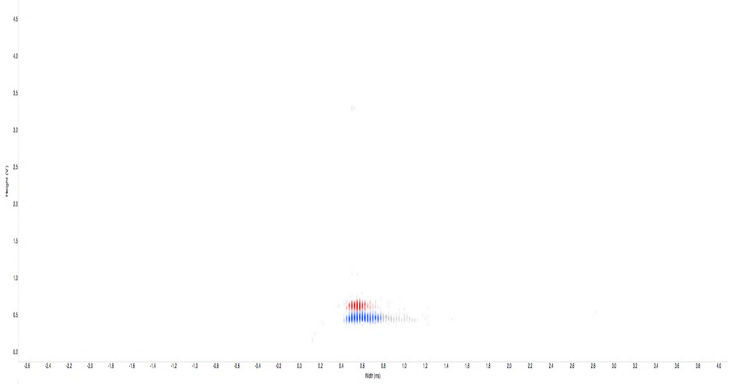

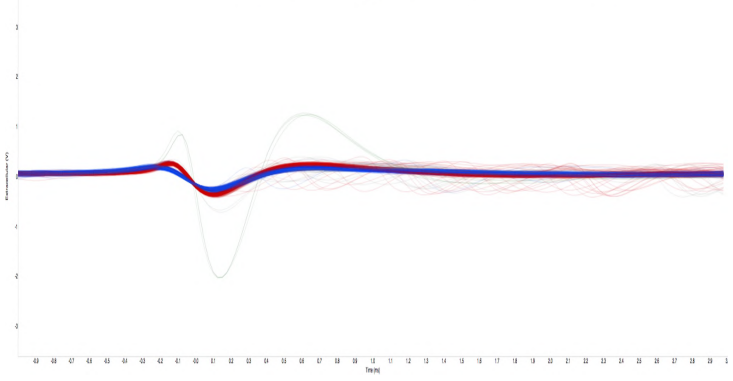

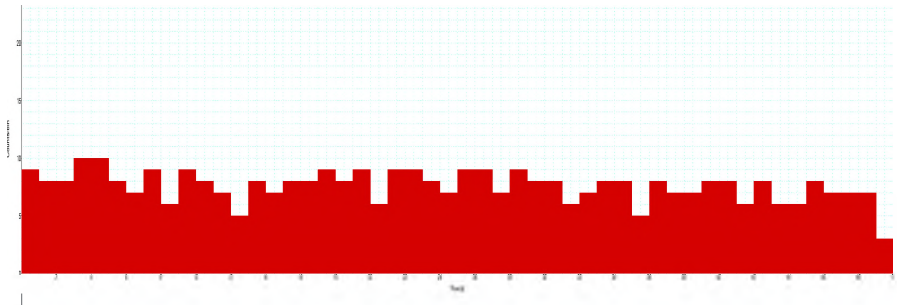

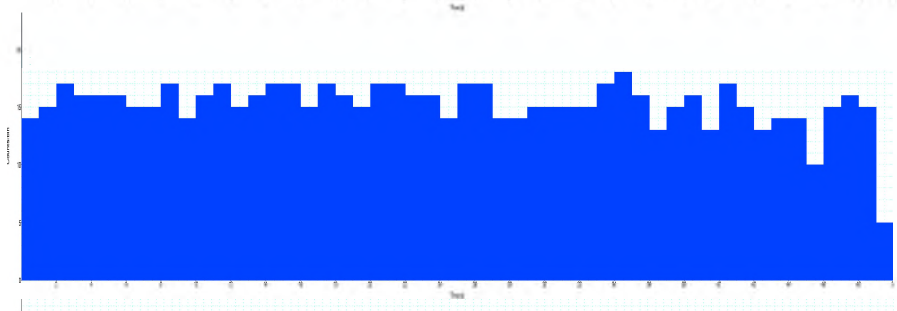

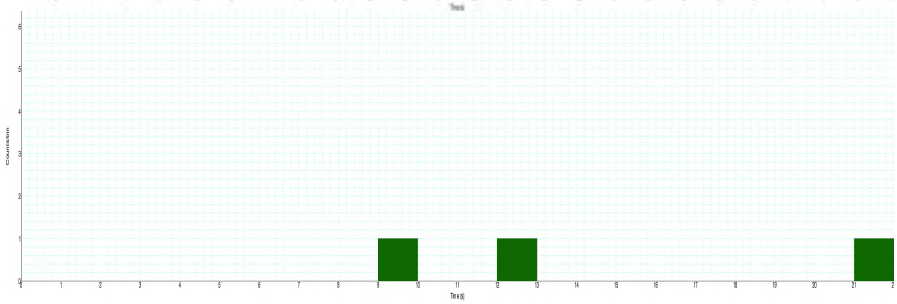

REL_1B 4mM

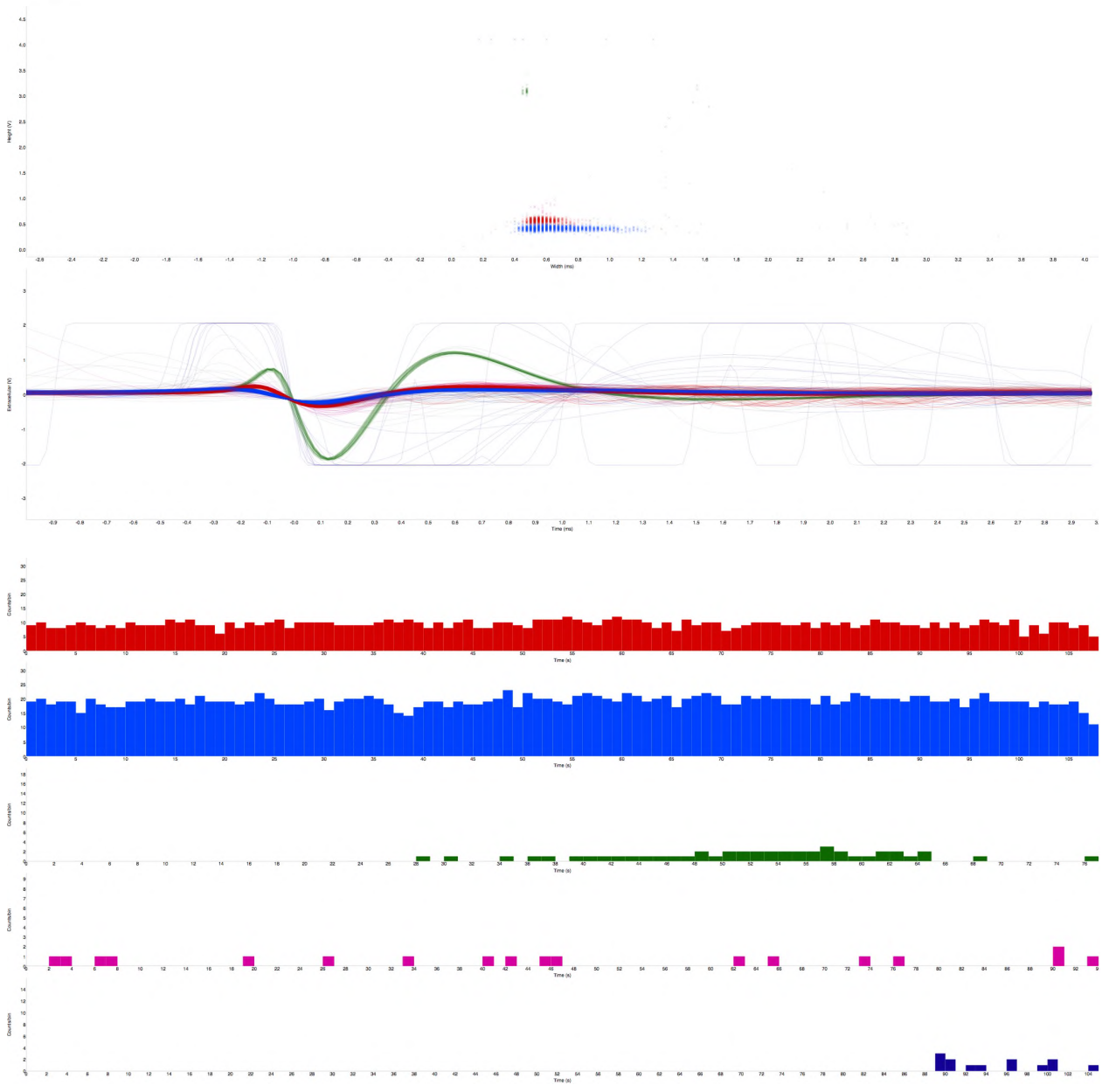

REL_1B Saline WASH1

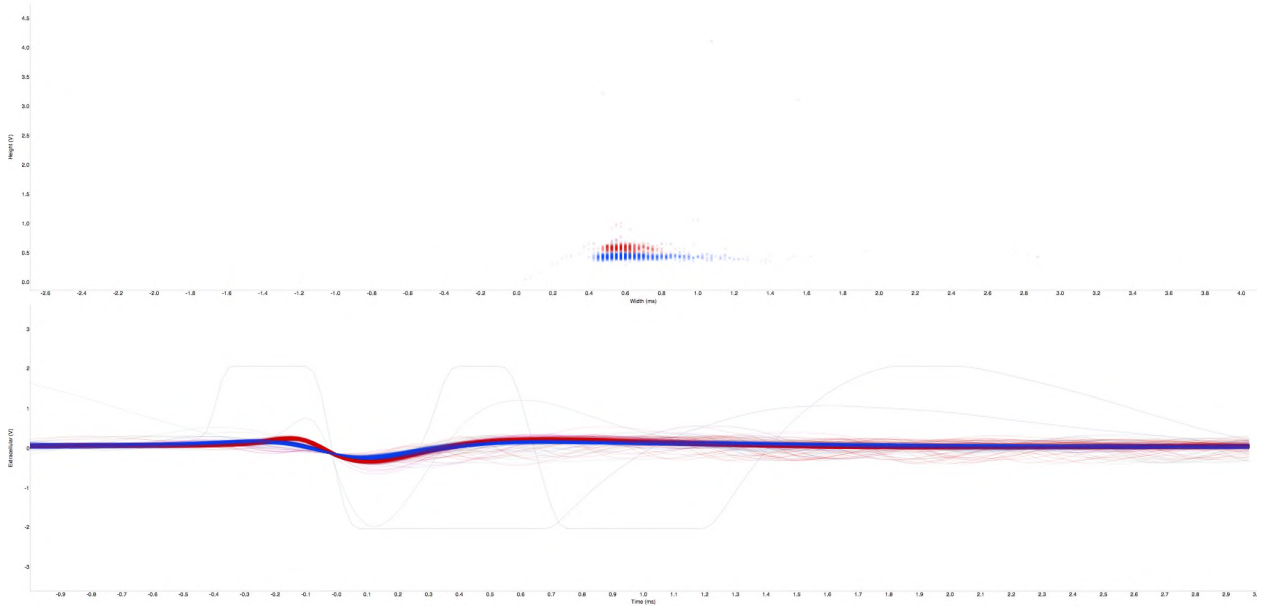

REL_1B 7mM

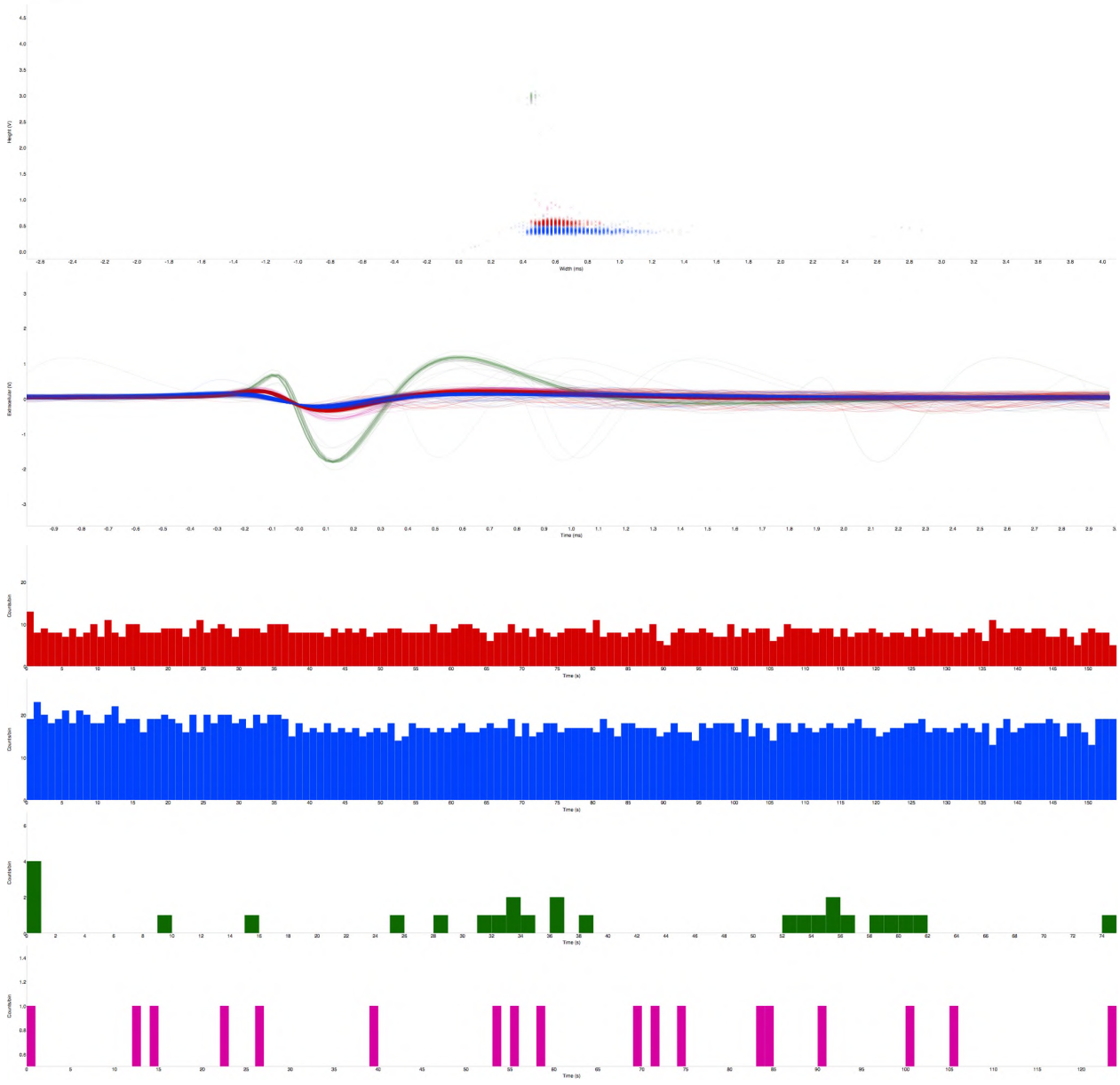

REL_1B 15mM

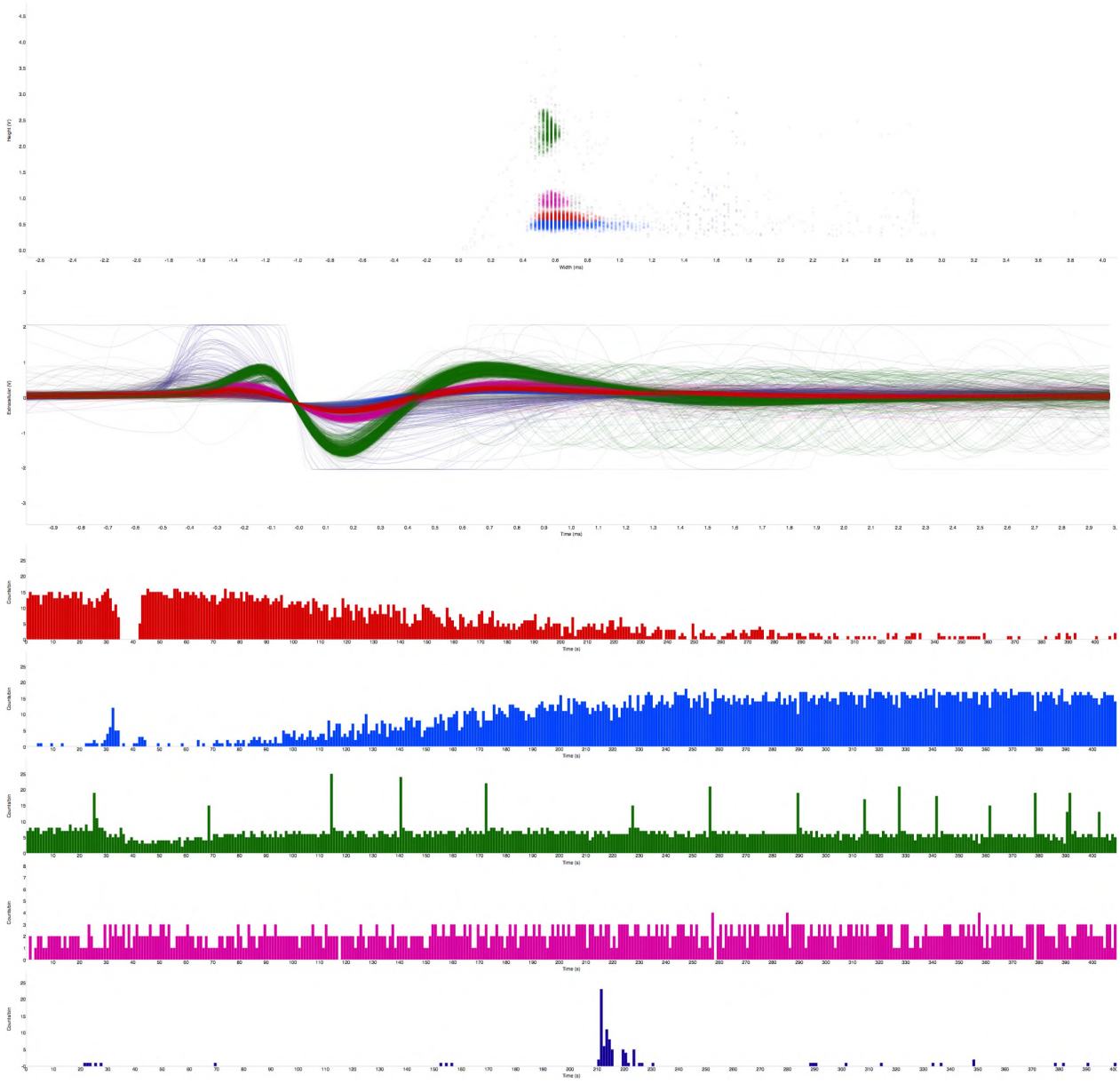

REL_1B Post15mMWASH

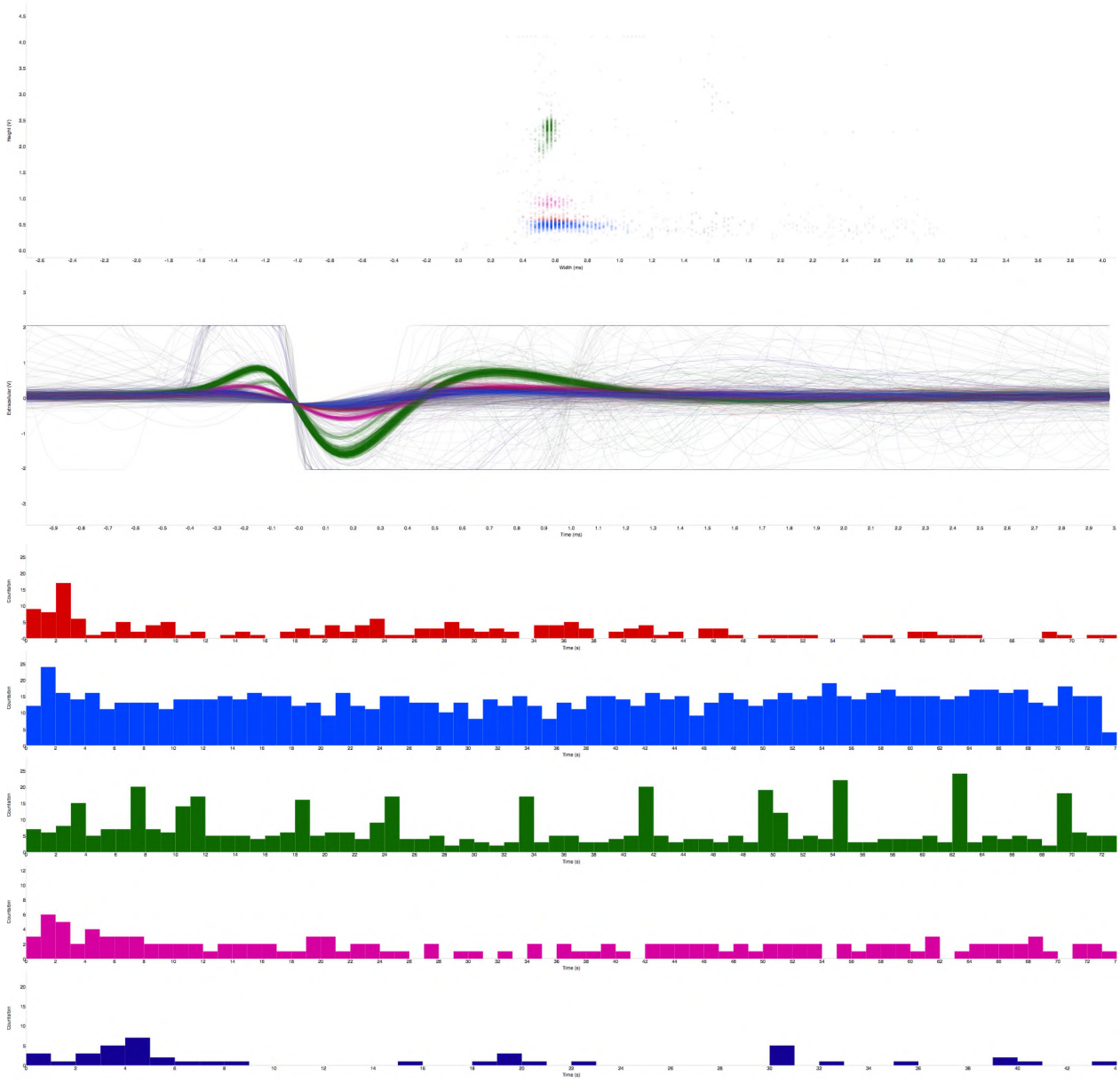

REL_1B 20mM

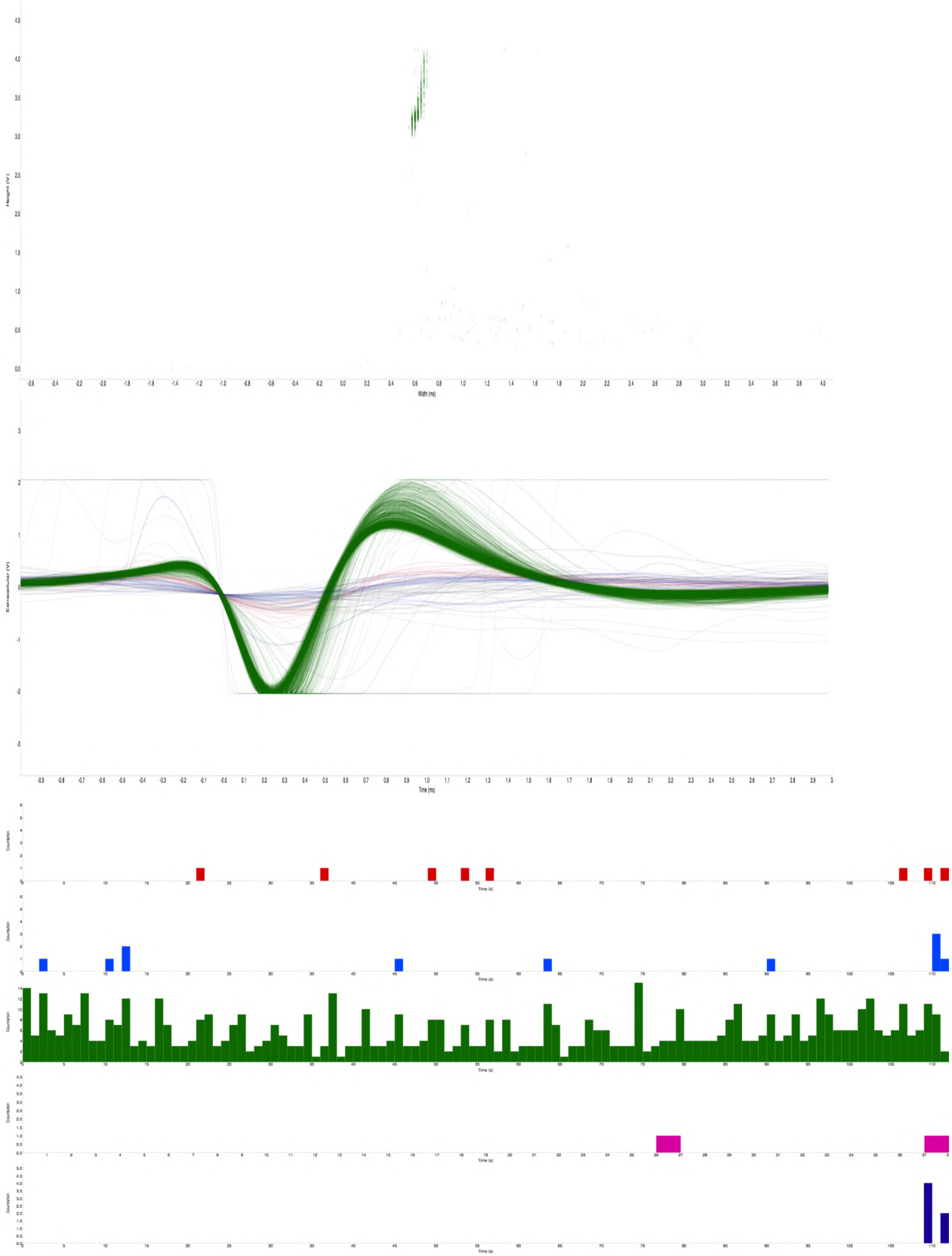

REL_1B HF Bursts

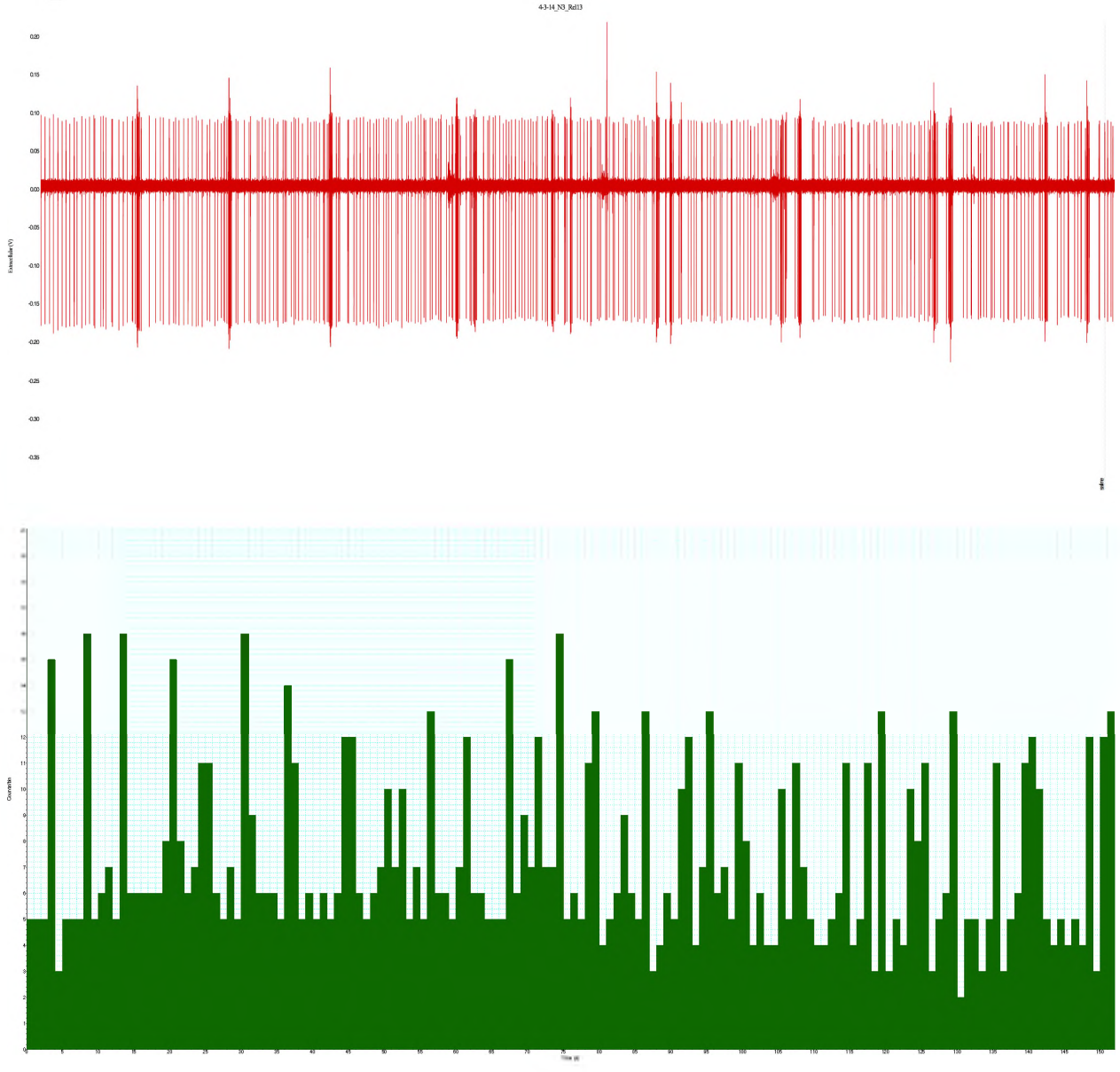

REL_1B 40mM Death